Karlsruhe Tritium Experiment: Detector System Commissioning and In-Situ PIN-Diode Array Dead-Layer Measurement

Brandon Lee Wall

A dissertation
submitted in partial fulfillment of the
requirements for the degree of

Doctor of Philosophy

University of Washington

2013

Reading Committee:

John F. Wilkerson, Chair

Hamish Robertson

Alejandro Garcia

Program Authorized to Offer Degree:
Physics

University of Washington

Abstract

Karlsruhe Tritium Experiment: Detector System Commissioning
and
In-Situ PIN-Diode Array Dead-Layer Measurement

Brandon Lee Wall

Chair of the Supervisory Committee:
Professor John F. Wilkerson
Physics

The Karlsruhe Tritium Neutrino (KATRIN) experimental goal is to measure the neutrino mass to 0.2 eV sensitivity at the 90 percent confidence level. This is an order of magnitude more sensitive than the two most recent direct neutrino mass measurements. The primary sensitivity of the KATRIN experiment is determined by the source strength and the main spectrometer resolution, but a confluence of focal plane detector parameters contribute to the uncertainty in the measured neutrino mass including the detector backgrounds and the detector electron response function.

The detector system group developed a figure of demerit, F, to quantify the effect of the detector system on neutrino mass uncertainty. F, essentially a signal to noise ratio, weights the focal plane detector response function against the total background based upon their influence of the m_ν^2 uncertainty. During commissioning of the detector system at the University of Washington, we determined a figure of demerit value of $1.12 \pm .01$, which nearly meets the tritium data taking goal for KATRIN.

A critical parameter that effects the detector response is the focal plane detector's dead layer. The KATRIN detector system's design constraints needed a novel approach to measure the dead-layer thickness not outlined in standard texts. We used a method of making measurements with an electron source over a range of incident energies, and then fit these monoenergetic electron source spectra to simulated spectra to determine the dead-layer

thickness of the KATRIN focal plane detector. The standard model of a monolithic dead layer yielded poor overall fits, while a model that allowed the energy deposited into the dead layer to diffuse back into the active region, gave an improved fit, with a preferred value of 46%. Using this model, the final detector dead layer thickness of the focal plane detector is $1554 \pm 5^{+18.8}_{-12.4}$ Å.

DEDICATION

To my parents, John and Linda, for their loving support.

TABLE OF CONTENTS

Page

LIST OF FIGURES

LIST OF TABLES

Chapter 1

INTRODUCTION

The neutrino has been the target of research by many scientists since its hypothesis in 1930. Wolfgang Pauli hypothesized the particle as a solution to several observed discrepancies in nuclear beta-decay experiments. This began a struggle of discovery to determine its properties that has spanned over 80 years.

1.1 Beta Decay

At the time of Pauli's hypothesis the nuclear model developed by Rutherford defined the nucleus as a tightly confined sea of electrons and protons. Two experimental results contradicted this model. The continuous beta-decay spectrum, first observed by Otto Hahn and Lise Meitner in 1911, contradicted energy conservation. According to the Rutherford model of the nucleus, beta-decay should obey a two body decay mode, where the nucleus ejects a single electron leaving a positively charged nucleus. The resulting electron energy spectrum should be a mono energetic peak as illustrated in blue rather than the observed continuous spectrum in red as illustrated in Figure 1.1. The second observation, from Raman scattering experiments performed by Rasetti, demonstrated the spin of the ^{14}N nucleus as spin 1 instead of the expected spin 1/2 [1].

Chadwick's detection of the neutron changed the Rutherford nuclear model to what we know it as today, where the nucleus is a set of bound protons and neutrons. In 1934 Fermi penned his theory for beta decay including Pauli's solution for the continuous decay spectrum, the neutrino and a nucleus consisting of protons and neutrons. Fermi's theory was based on his previous theory for radiation emitted from atomic transitions [2]. Instead of an electron transitioning from one atomic state to another, Fermi viewed the nucleus in a similar fashion, where the neutron and proton were separate quantum states in the nucleus. The neutron to proton transition in a nucleus X results in an ejected electron and

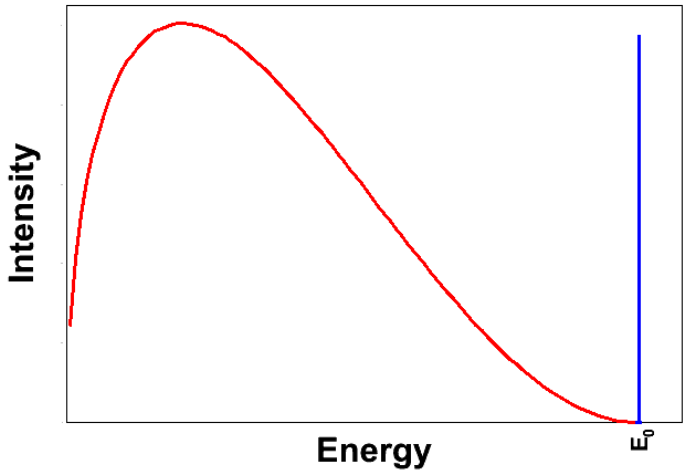

Figure 1.1: A mono-energetic two-body decay peak in blue at energy E_0 and continuous beta-decay spectrum in red with end-point energy E_0.

antineutrino.

$$ {}^{A}_{Z}X \rightarrow {}^{A}_{Z+1}X + e^{-} + \overline{\nu_e} \tag{1.1} $$

Fermi's beta-decay model leads to the probability of emitting an electron with total energy E:

$$ dN(E) = K|M|^2 F(Z,R,E) p_e E (E_0 - E)\sqrt{(E_0 - E)^2 - m_{\nu_e}^2 c^4}\, dE, \tag{1.2} $$

where,

$$ K = G_F^2 \frac{m^5 c^4}{2\pi^3 \hbar^7} \cos(\theta_c), $$

G_F is the Fermi coupling constant, θ_c is the Cabibbo angle; M is the nuclear matrix element for the decay; p_e is the electron momentum; E_0 is the end point energy of the decay where the electron antineutrino mass, m_{ν_e}, is zero; F(Z,R,E) is the Fermi function correcting for Coulomb interactions between the nuclear charge and the emitted electron. This theory accounts for the continuos beta decay spectrum and the spin discrepancy observed by Rasetti.

1.2 Neutrino Mass Measurement

The mass of the neutrino has been constrained by various experiments, but is still left undetermined within a range from 48 meV to 2.0 eV. Oscillation experiments are sensitive to the mass squared differences but provide the lower bound of the neutrino mass. Currently there are three methodologies to measure the absolute mass scale of the neutrino; examination of high precision cosmological and astrophysics measurements, rates of neutrinoless double beta decay, and weak-decay kinematic studies. The first two methodologies have inherent model dependencies while the kinematic searches do not.

1.2.1 Oscillation Experiments

Oscillation experiments are an abundant source of information regarding neutrino properties. The experiments determined that the neutrino flavor eigenstates are not equivalent to their mass eigenstates. After the creation of a neutrino in a flavor state from a weak interaction it propagates through space as a mixture of mass states. Each mass state propagates at different velocity causing the neutrino to become a new mixture of flavor states and the probability of measuring the original flavor state to change.

Two quantities are measured in oscillation experiments, the mixing angle θ_{ij} and the difference of the squared masses Δm^2_{ij}. The mixing angles fill out the lepton mixing matrix $U^L_{\alpha i}$ that relates the flavor states to the mass states given by,

$$\begin{aligned} U^L_{\alpha i} &= \begin{bmatrix} U_{e1} & U_{e2} & U_{e3} \\ U_{\mu 1} & U_{\mu 2} & U_{\mu 2} \\ U_{\tau 1} & U_{\tau 2} & U_{\tau 3} \end{bmatrix} \\ &= \begin{bmatrix} c_{12}c_{13} & s_{12}c_{13} & s_{13}e^{-i\delta} \\ -s_{12}c_{23} - c_{12}s_{23}s_{13}e^{i\delta} & c_{12}c_{23} - s_{12}s_{23}s_{13}e^{i\delta} & s_{23}c_{13} \\ s_{12}s_{23} - c_{12}c_{23}s_{13}e^{i\delta} & -c_{12}s_{23} - s_{12}c_{23}s_{13}e^{i\delta} & c_{23}c_{13} \end{bmatrix} \end{aligned} \tag{1.3}$$

where $s_{ij} = sin(\theta_{ij})$, $c_{ij} = cos(\theta_{ij})$, and δ is the charge parity violating phase. Being only sensitive to the mass squared differences, oscillation experiments can't provide the absolute

mass scale of the neutrino but can provide a lower limit. If one assumes a zero mass for the lightest neutrino then the lower limit for the heaviest neutrino mass is $m_\nu \gtrsim .048$ eV. Table 1.1 details the current values for the oscillation parameters.

Table 1.1: Particle Data Group listings for neutrino oscillation parameters[3].

Oscillation Parameters
$sin^2(2\theta_{12}) = 0.857 \pm 0.024$
$sin^2(2\theta_{23}) > 0.95$
$sin^2(2\theta_{13}) = 0.098 \pm 0.013$
$\lvert\Delta m_{32}\rvert^2 = (2.32 + 0.12 - 0.08) * 10^{-3}$ eV^2
$\Delta m^2_{21} = (7.50 \pm 0.20) * 10^{-5}$ eV^2

There are two possible orderings for the neutrino masses: the normal hierarchy where $m_1 < m_2 < m_3$ and the inverted hierarchy $m_3 < m_1 < m_2$. Solar oscillation experiments determine the mass ordering of ν_2 and ν_1 [4].

1.2.2 Astrophysics and Cosmology Measurements

During the big bang, neutrinos are generated as a form of hot dark matter (currently the only known source of hot dark matter). They are readily produced in weak interactions until a decoupling temperature of $T \sim 1MeV$ at which point their relativistic velocity causes them to free stream through matter fluctuations in the early expanding universe. Matter fluctuations are then suppressed below the free streaming length or Jeans scale. The matter density power spectrum below this length is retarded by the fraction,

$$\frac{\Delta P}{P} \sim -8\frac{\Omega_\nu}{\Omega_m} \tag{1.4}$$

where Ω_ν is the neutrino matter density of the total dark matter content Ω_m.

The neutrino matter density is the product of the total neutrino mass Σm_ν and the relic neutrino number density normalized to the critical density ρ_c . Assuming that the relic neutrinos are non-relativistic, the relic neutrino number density n_ν is fixed to 3/11 of the cosmic microwave background photon density, n_γ, and related to the CMB temperature,

T_{CMB}.

$$n_\nu = \frac{3}{11} n_\gamma = \frac{6\zeta(3)}{11\pi^2} T_{CMB}^3 \tag{1.5}$$

Hence,

$$\Omega_\nu = \frac{n_\nu \Sigma m_\nu}{\rho_c} = \frac{\Sigma m_\nu}{h^2 34eV}. \tag{1.6}$$

The relationship between the matter power spectrum and the neutrino mass means data sensitive to large scale structure such as the cosmic microwave background, weak lensing of distant galaxies, galactic redshifts, and baryon acoustic oscillations are sensitive to the neutrino mass. The data from these measurements assumes an input model to extract various cosmological parameters including Ω_ν. Most commonly used is a flat concordance model ΛCDM, where $\omega = -1$ and $\Omega_k = 0$. Ω_ν is degenerate with cosmological parameters such as Ω_m and the Hubble parameter h.

Table 1.2: Cosmological measurements of Σm_ν from the data sets: Wilkinson Microwave Anisotropy Probe (WMAP), baryon acoustic oscillations (BAO), type-Ia supernovae (SN), weak lensing (WL), Hubble Space Telescope (HST), and Sloan Digital Sky Survey MegaZ.

Reference	Data Used	Σm_ν eV
Komatsu et al. [5]	WMAP7	< 1.3
Komatsu et al. [5]	WMAP7+BAO+HST	< 0.58
Ichiki et al. [6]	WMAP5+SNe+BAO+WL	< 0.54
Thomas et al. [7]	WMAP5+SNe+BAO+MegaZ+HST	< 0.28

The degeneracies, data sets used, and errors from cosmological parameters measured by other experiments lead to a spectrum of neutrino mass limits. Table 1.2 lists a range of mass limits from $\Sigma m_\nu < .27$ to 1.3 [5]. The degeneracies and range of mass results lead to an argument for terrestrial based measurement of the neutrino mass. A model independent measurement would help fix a value for Ω_ν and provide better results for the remaining cosmological parameters.

1.2.3 Neutrinoless Double Beta Decay

Neutrinoless double beta decay is a posited extremely rare decay process that requires the neutrino to be its own anti-particle or a Majorana particle rather than Dirac. In the process, two neutrons in the nucleus decay to two protons and 2 electrons without the emission of two neutrinos.

$$ {}^{A}_{Z}X \rightarrow {}^{A}_{Z+2}X + e^{-} \tag{1.7} $$

The limits of the half-life of this process are on order of $T_{1/2} > 10^{22}$ to 10^{25} years depending upon the isotope being measured [8].

Searching for neutrinoless double beta decay is extremely difficult, since the life-times are so long. The technology to measure these lifetimes varies greatly from isotopically enriched semi-conductor based detectors, doped liquid scintillators, to liquid cryogens. The common thread in these experiments is the necessity for low background environments and good signal discrimination.

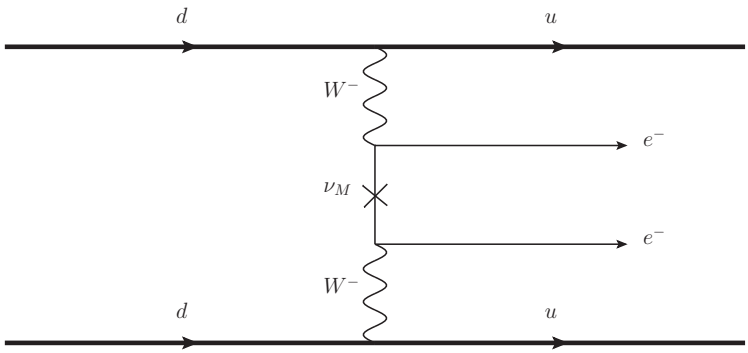

Figure 1.2: Standard neutrinoless double beta-decay Feynman diagram with light neutrino exchange.

The extraction of the neutrino mass from the half life of neutrinoless double beta decay requires the assumption of a mechanism for the decay. The most common model for the decay is the exchange of a light neutrino as seen in figure 1.2. The relationship between the half-life and the neutrino mass is then

$$ [T^{0\nu}_{1/2}]^{-1} = G^{0\nu}|M^{0\nu}|^2|\langle m_{\beta\beta}\rangle|^2 \tag{1.8} $$

where $G^{0\nu}$ is a calculable phase factor, $M^{0\nu}$ is the nuclear matrix element, and $\langle m_{\beta\beta}\rangle$ is the effective neutrino mass[9].

Unlike cosmology, neutrinoless double beta decay is not sensitive to a simple sum of the neutrino mass eigenstates, but to the coherent sum

$$\langle m_{\beta\beta}\rangle = \sum_{k=1}^{3} |U_{ek}^{L}|^2 m_k e^{i\phi_k}. \tag{1.9}$$

The unknown Majorana phases, ϕ_k, complicate matters in extracting an absolute mass scale, since there can be cancellations depending on the unknown phases. Alone neutrinoless double beta decay can provide complimentary, but model dependent, information on the absolute mass scale [10]

Table 1.3: Neutrinoless double beta-decay half-life limits at the 90% C.L. for various candidate isotopes and effective neutrino mass limits. The effective mass limits are the full range of values for all nuclear matrix elements listed in the experiment's respective references.

Isotope	$[T_{1/2}^{0\nu}]$ y	$\langle m_{\beta\beta}\rangle$ eV	Experiment
^{148}Ca	$> 5.8 * 10^{22}$	$< 3.5 - 22$	ELEGANT[11]
^{76}Ge	$> 1.9 * 10^{25}$	$< 0.23 - 0.64$	Heidelberg-Moscow[12][13]
^{100}Mo	$> 1.1 * 10^{24}$	$< 0.45 - 0.93$	NEMO3[13]
^{82}Se	$> 3.6 * 10^{23}$	$< 0.89 - 2.43$	NEMO3[13]
^{130}Te	$> 2.8 * 10^{24}$	$< 0.30 - .71$	CUOROCINO[14]
^{136}Xe	$> 4.9 * 10^{24}$	$< 1.1 - .2.9$	DAMA[15]

Nuclear matrix elements are calculated from a variety of models. The most common models used are the Quasiparticle Random Phase Approach (QRPA) and the shell model. A matrix element value for a particular isotope varies depending on the model used and has an error on order of 20 percent. This leads to large uncertainty for the value of the effective neutrino mass. Table 1.3 shows the current limits for $[T_{1/2}^{0\nu}]$ for several isotopes and the ranges for $\langle m_{\beta\beta}\rangle$ limits.

1.2.4 Kinematic Measurement of Neutrino Mass

Kinematic measurements of the neutrino mass span the last sixty years. With the discovery of neutrino oscillations, it is known that neutrino flavors do not have well-defined masses. The current effective mass limits for each neutrino flavor are given in Table 1.4. Tau neutrino limits are derived from semi-leptonic decays of a Tau into pions. Measurements of pion decays into muon and muon neutrinos provide the muon neutrino mass limit. The electron neutrino mass, $\langle m_\beta \rangle$, limits primarily come from spectral measurements of beta decay. Beta decay has the greatest sensitivity to the neutrino masses because of the strong mixing in the neutrino sector as measured by oscillation experiments and hence provide the smallest mass limit.

Table 1.4: Current effective neutrino mass limits for each flavor type.

Neutrino Flavor	Mass Limit	C. L.	Ref.
ν_τ	< 18.2 MeV	95%	[16]
ν_μ	< 0.17 MeV	90%	[17]
ν_e	< 2.0 eV	95%	[18]

Fermi's original paper on beta decay discussed spectral measurements of the neutrino mass as illustrated in figure 1.3 showing effects on the beta-decay spectrum from non-zero neutrino mass. In equation 1.2 the neutrino mass has its greatest effect near the end-point of E_o. As the beta-decay energy decreases the spectrum is quickly dominated by the $(E - E_o)^2$ term but near the endpoint the integral spectrum goes as $(\frac{m_\nu}{E_o})^3$. This implies that beta-decay sources with lower end-point energies have greater sensitivity to the neutrino mass.

Tritium with an endpoint of 18.6 keV has the second lowest beta-decay endpoint and is the preferred candidate isotope for a number of reasons as discussed in section 2.2. Figure 1.4 is the spectral distortion measured by Curran, Angus, and Cockroft in 1949; the earliest attempt to measure the neutrino electron mass. They found an upper limit of $m_\beta < 1keV$ [19]

The two most recent tritium based experiments, the Mainz group and the Troitsk group,

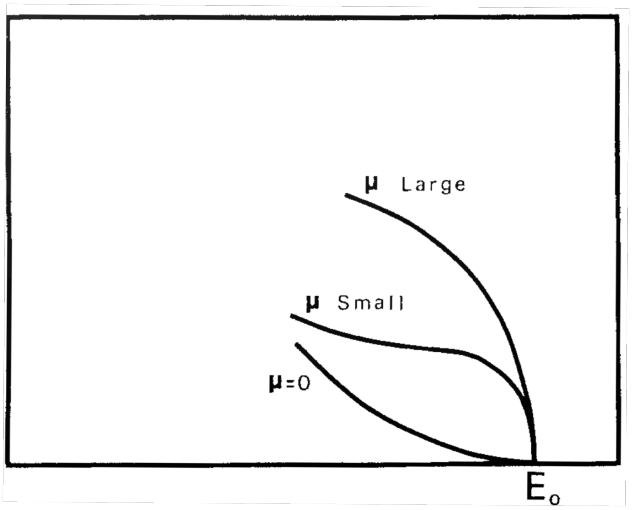

Figure 1.3: Effect of the neutrino mass μ on the beta-decay spectrum as illustrated by Fermi[2].

used different tritium source configurations. The Mainz experiment in using a monolayer of frozen tritium on a substrate set a limit of $m_\beta \leq 2.3eV$ [20]. Troitsk used a windowless gaseous tritium source. Originally their resulting tritium spectrum could only be fit by introducing a systematic step function. After a major effort to improve data integrity, the need for the step function vanished, and they determined limit to $m_\beta < 2.0eV$[18].

Table 1.5: Kinematic electron neutrino mass limits.

Experiment	Source	$\langle m_\beta \rangle$ eV	C.L.
Mainz [20]	Frozen Tritium	≤ 2.3	95%
Troitzk [18]	Windowless Gaseous Tritum	< 2.0	95%
MANU [21]	Rhenium 187	< 26	95%
MiBeta [22]	Rhenium 187	≤ 21.7	90%

As an alternative to the tritium based measurements, Rhenium-187 based bolometers have been used to measure the neutrino mass. Rhenium-187 has the lowest beta-decay end-point of 2.6 keV. The MANU[21] and MiBETA[22] experiments have measured mass limits

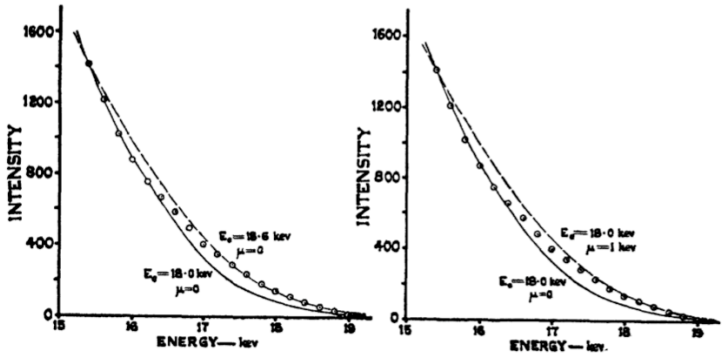

Figure 1.4: Curran, Angus, and Cockroft comparison of the tritium end-point spectrum[19].

of 26 eV (95% C.L.) and 21.7 eV (90% C.L.) respectively. MARE is the next generation of these experiments and proposes to reach 2 eV sensitivity[23].

Chapter 2

KATRIN

2.1 KATRIN

The Karlsruhe Tritium Neutrino (KATRIN) experiment utilizes a high precision electron energy spectrometer to measure the distortion of the tritium beta decay spectrum as a means to determine the neutrino mass. The goal of the KATRIN experiment is to measure the neutrino mass to 0.2 eV sensitivity at the 90 percent confidence level. This is an order of magnitude more sensitive than the two most recent neutrino direct mass measurements.

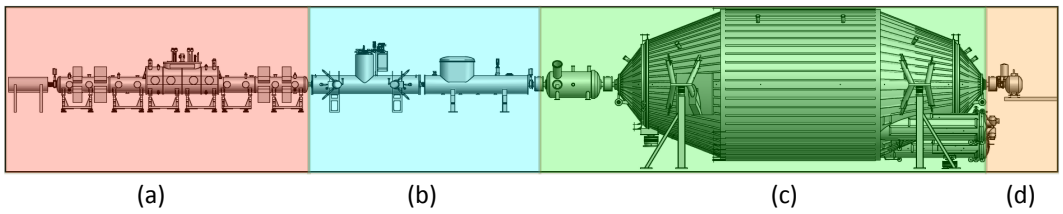

Figure 2.1: KATRIN experimental apparatus:(a) tritium source section, (b) transport section, (c) pre and main spectrometers, and (d) detector system.

The KATRIN experimental apparatus (Figure 2.1) consists of four major sections: a beta decay source, the transport section, an electron spectrometer, and finally the detector system [24]. The source is an extended source of gaseous molecular tritium. Beta decay electrons are guided by magnetic fields to a pre and main spectrometer. Acting as high-pass energy filter the two spectrometers reject electrons below an energy set point. The selected beta decay electrons are detected by a silicon PIN diode array in the detector system.

2.2 Tritium Source

Gaseous molecular tritium has been chosen as the ideal beta decay source for several reasons. First it has a low Q-value of 18.6 keV which maximizes the sensitivity to the spectral distortion of the neutrino mass. The decay from ^{3}H to ^{3}He is a super-allowed nuclear transition, which gives a high specific activity. Both isotopes have a simple electron structure so that β interactions with the shell electrons are calculable. Finally tritium has a relatively short half life of 12.3 years and a small self-interaction cross section.

The source is 95% pure gaseous molecular tritium. The column length and density of the source section is restricted by the interaction path length of the β-decay electrons in the source. The diameter is limited by the size of the main spectrometer's analyzing plane. KATRIN's planned source column density is 5x10^{17} molecules/cm^2 and has a length of 10 meters, producing 10^{11} β-decay electrons per second. The source is circulated, filtered, and replenished to maintain purity. Its temperature is strictly controlled to $\pm$0.03 K.

Understanding the source conditions is critical to KATRIN's final result. Strict controls and monitoring of the column density are necessary to combine data at different spectrometer settings because variations in the column density change the source strength. Further, the column density is needed in order to apply energy-loss corrections because the emitted betas can scatter while propagating through the source. Source strength is monitored via a Faraday cup, while the column density is probed using a rear mono-energetic electron source.

Emitted betas in the source are guided to either the rear wall or the spectrometers via a 3.6 T magnetic field. Upon exiting the source section the electrons are magnetically guided by a transport section to the spectrometers. The transport section uses differential pumping and an argon frost to remove molecular tritium gas and T^{3}He daughters that diffuse past the source section. Tritium contamination into the spectrometers creates a source of unfiltered beta emission that would contaminate the measured spectrum.

2.3 Pre and Main Spectrometers

The β-decay electrons leaving the transport section encounter a tandem of spectrometers. Each spectrometer utilizes a **M**agnetic **A**diabatic **C**olumnating **E**lectrostatic (MAC-E) filter [25][24]. During neutrino operation, the pre-spectrometer filters out electrons below 18.3 keV. This removes electrons of little neutrino physics value and reduces the flux of electrons entering the main-spectrometer to $10^3 e^-/s$. The lower flux in the main spectrometer reduces ionization of the residual gas, a background for the experiment. The main spectrometer scans the region 0 to 30 eV below the endpoint.

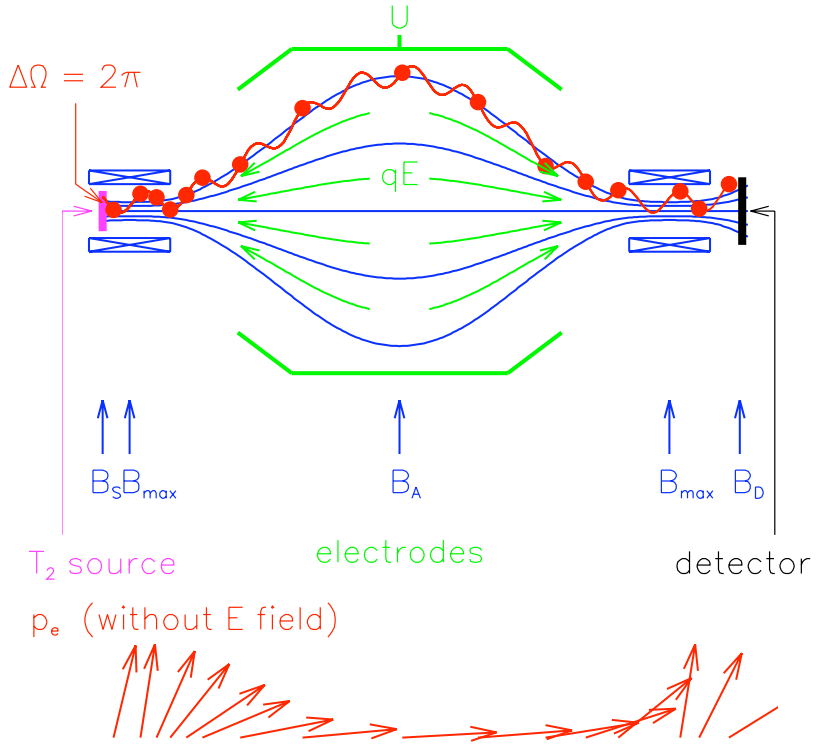

Figure 2.2: MAC-E filter design and illustration of the momentum transformation of the beta-decay electrons[24].

An electron in a MAC-E spectrometer moves from a region of high magnetic field (B_{max}) at the entrance of the spectrometer to a region of low magnetic field (B_{min}) at the analyzing plane. The magnetic moment of the electron remains constant, while the direction of the

electron's momentum, illustrated in figure 2.2, adiabatically rotates to point along the z-axis. At the analyzing plane of the spectrometer, the electron's momentum is nearly parallel to the magnetic field lines and orthogonal to a retarding electrostatic potential. This type of spectrometer acts as a high-pass filter allowing only electrons with energy higher than the set point of the retarding potential to proceed past the analyzing plane.

The precision ($\frac{\Delta E}{E}$) of a MAC-E filter is proportional to the ratio of the maximum magnetic field (B_{max}) to the minimal field (B_{min}) at the analyzing plane[25].

$$\frac{\Delta E}{E} = \frac{B_{min}}{B_{max}} \tag{2.1}$$

The pre-spectrometer has an energy resolution of 100 eV, while the main spectrometer, with a 10 times larger analyzing plane, has an expected energy resolution of 0.93 eV.

Table 2.1: Pre and main Spectrometer specification summary[24].

Specification	Pre-spectrometer	Main Spectrometer
Vacuum	10^{-11} mbar	10^{-11} mbar
B_S	3.6 T	3.6 T
B_{max}	4.5 T	6 T
B_{min}	$2 * 10^{-2}$ T	$3 * 10^{-4}$ T
ΔE	100 eV	0.93eV
E-qU	300 eV	0 to 30 eV

The magnetic configuration of the spectrometers has an added layer of filtration. The spectrometer, utilizing the magnetic mirror effect, rejects electrons emitted in the source at a large angle from the magnetic field axis. These electrons, traveling a long path through the source, have an increased chance of interacting within the source causing an energy loss that distorts the measured spectrum. The source magnetic field (B_S) is less than the maximum magnetic field at the end of each spectrometer. The ratio of the maximum field to the field in the source determines the maximum accepted starting angle (θ_{max})[25]:

$$\sin\theta_{max} = \sqrt{\frac{B_S}{B_{max}}} \tag{2.2}$$

The probability of a β-decay electron of energy E being transmitted from a spectrometer set at potential U is analytically calculated. The analytically calculated transmission function ($T(E, qU)$)[24] using equation 2.1 and 2.2 is

$$T(E,qU) = \left\{ \begin{array}{cc} 0 & E - qU < 0 \\ \frac{1-\sqrt{1-\frac{E-qU}{E} * \frac{B_S}{B_{max}}}}{1-\sqrt{1-\frac{\Delta E}{E} * \frac{B_S}{B_{max}}}} & 0 \leqslant E - qU \leqslant \Delta E \\ 1 & E - qU > \Delta E \end{array} \right\} \tag{2.3}$$

2.4 Detector System

The KATRIN detector system is the primary responsibility of the U.S. collaboration institutions. After the spectrometers, the flux of accepted beta-decay electrons is reduced by a factor of 2x10^{-13} from the total flux, leaving a final rate of $\sim$ 10 mHz at the detector system. This low rate means that the chosen focal plane detector needs to have a high electron detection efficiency and reasonable energy resolution for 18.6 keV electrons. The focal plane detector chosen for this application is a silicon monolithic PIN diode array and discussed in more detail in chapter 3.

2.4.1 Vacuum System

The KATRIN detector system is divided into an extreme high vacuum (XHV) and high vacuum (HV) chamber. The XHV chamber houses the focal plane detector and connects to the main spectrometer. It must be compatible with the the main spectrometer vacuum of 10^{-11} mbar, meeting a design vacuum of 10^{-9} mbar. The XHV is separated from the HV by a copper post-acceleration electrode and the detector feed-through flange. The HV chamber has a lower vacuum requirement of 10^{-6} mbar because it contains the focal plane detector front-end electronics and out-gassing from these components is too high to meet the XHV chamber requirements. Table 2.2 lists the achieved vacuums for both chambers.

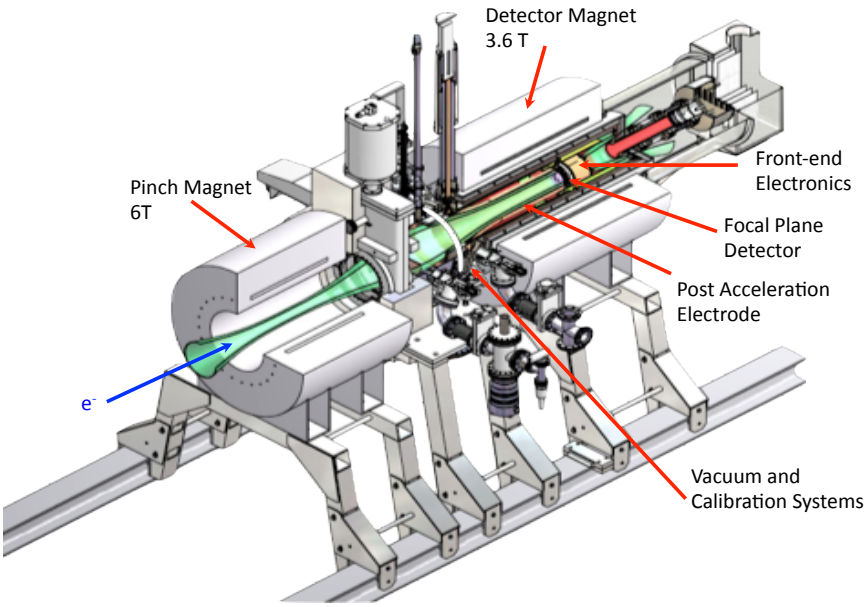

Figure 2.3: Primary components of KATRIN detector system.

2.4.2 Post-Acceleration Electrode

The post-acceleration electrode (PAE) is a spun copper electrode. Post acceleration raises the potential of the focal plane detector and boosts the energy of electrons. This moves the filtered β-decay electrons into a higher energy region with lower backgrounds, increasing the signal to background ratio (Figure 2.4). Increasing the electron energy also decreases the backscattering off the focal plane detector and reduces the effects of the focal plane detector's dead layer. This results in better detector resolution for electrons.

2.4.3 Magnets

The detector system magnetic design consists of two solenoid super conducting magnets. The pinch magnet, stationed between the main spectrometer and the detector system, sets the maximum magnetic field for the main spectrometer. Down stream from the spectrom-

Table 2.2: Detector system vacuum chamber designed and achieved base pressures.

Chamber	Design Pressure	Measured Pressure
XHV	1×10^{-9} mbar	0.7×10^{-9} mbar
HV	1×10^{-6} mbar	0.3×10^{-6} mbar

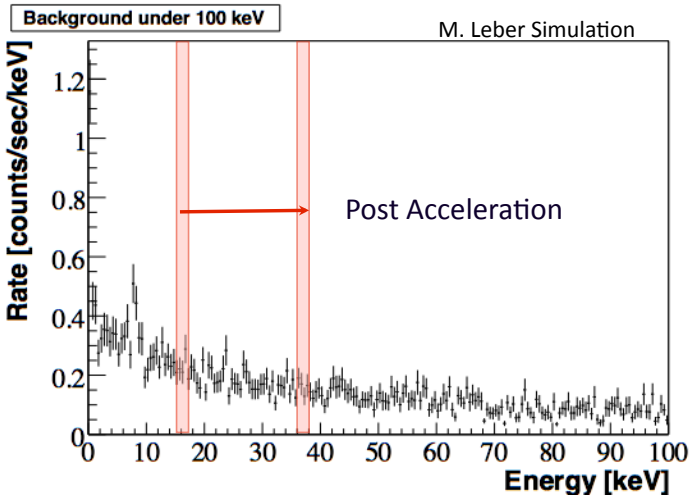

Figure 2.4: A simulated detector system background spectrum[26]. The lower shaded region of interest at the tritium endpoint (18.6 keV) can be moved to the higher energy region of interest with a lower background with 20 kV of post acceleration.

eter and pinch magnet is the detector magnet that images the source onto the focal plane detector.

Both magnets were manufactured by Cryomagnetics, Inc. Each magnet is capable of reaching a maximum field setting of 6T and has a magnetic center within 2mm of the center of their respective bores. The nominal field setting is 6T on the pinch magnet and 3.6T on the detector magnet. The magnetic field for each magnet drifts less than 200 ppb/hour.

2.4.4 Passive and Active Shielding

The detector system utilizes both active and passive shielding to screen the focal plane detector from the effects of environmental and cosmic radiation. The shields fit within the bore of the detector magnet and around the detector vacuum chamber. The passive shield is a 1 cm thick cylindrical copper layer nested inside a 3 cm thick cylinder of lead [27]. It primarily reduces the environmental backgrounds.

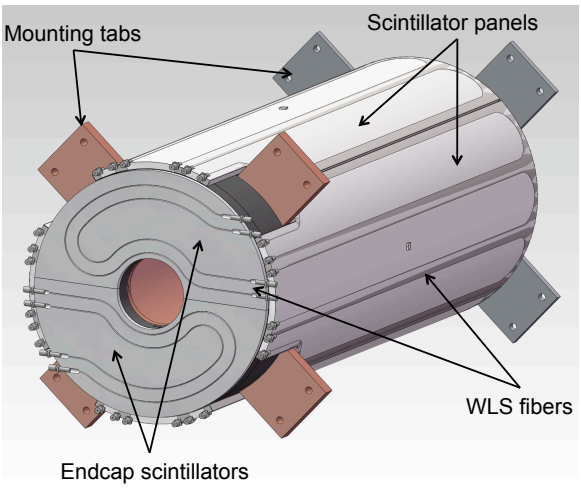

Figure 2.5: Scintillator veto panels embedded with wavelength-shifting fiber.

Surrounding the passive shield is the scintillator veto[27]. One centimeter thick Saint Gobain Bicron-408 plastic scintillator was shaped into 4 8-cm diameter and 106.3 cm long panels. Each panel is embedded with 3 wavelength-shifting fibers for a total of six fiber outputs. The end cap is divided into two half-moon panels with 4 wavelength-shifting fibers embedded in each. The wavelength-shifting fibers are mated with clear optical fibers that connect to multi-pixel photon counter units manufactured by Hamamatsu. The remaining details of the veto data acquisition and setup is described in section 4.2.1.

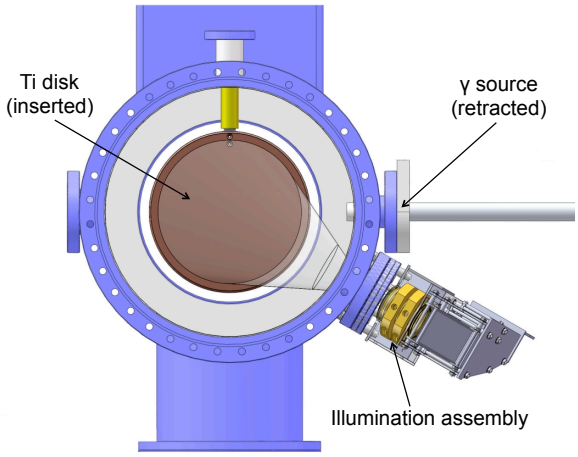

Figure 2.6: The retracted Americium-241 source holder and titanium photoelectron source as viewed from the focal plane detector.

2.4.5 Calibration Systems

2.4.5.1 Americium-241 Source

The focal plane detector energy calibration is provided by a sealed $500\mu Ci$ Americium-241 source. The source holder in figure 2.6 is attached to an air driven stepper motor system that moves the source in and out of the flux tube. The exterior of the source holder is at the extreme high vacuum pressure, while the interior and the source are at atmospheric pressure. This allows the source to be removed from the apparatus to reduce backgrounds during data taking.

^{241}Am alpha decays to ^{237}Np, emitting gammas. Two of the gamma emission lines occur at 26.3 keV and 59.5 keV and create two distinct peaks in the ^{241}Am spectrum in figure 2.7. The remaining peaks in the spectrum are created from ^{237}Np x-ray doublets. The doublets have well defined energies but are represented by only a single peak in the spectra due to the comparatively large detector resolution. This makes them poor calibration peak candidates. The two calibration peaks are fitted with a gaussian function and the centroid in ADC channel of each is extracted. A linear fit (ax+b) of the two points determines the energy calibration.

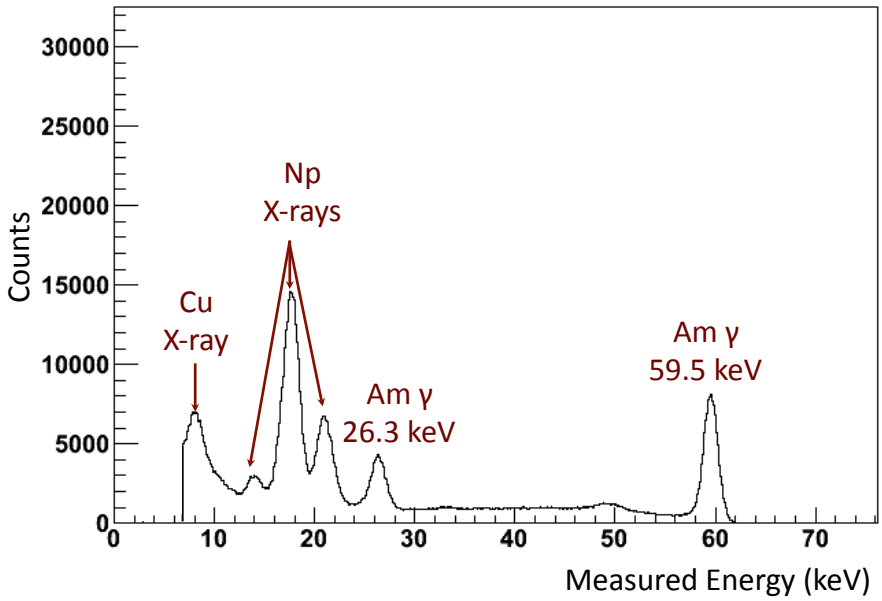

Figure 2.7: An example of an ^{241}Am spectrum measured by the focal plane detector and summed over 127 pixels. The 59.5 keV and 26.3 keV peaks are used for focal plane detector energy calibration.

Americium data taking needs to occur at two different source positions. In the presence of the magnetic field, the americium source generates Compton scattering electrons in the source holder. Those electrons are guided to pixels on the detector and mask the 59.5 keV peak.

2.4.5.2 Electron Source

A photoelectron gun serves as the electron calibration source. An ultraviolet diode illuminates a titanium disk causing photoelectric emission (Figure 2.6). A variable high-voltage supply applies a negative potential up to 25 kV on the disk accelerating the photoelectrons toward the focal plane detector. The accelerated electrons are guided to the detector by the magnetic fields generated by the pinch and detector magnets. At nominal settings, the magnets image the source disk onto the focal plane detector.

Chapter 3

FOCAL PLANE DETECTOR AND DATA ACQUISITION

3.1 Focal Plane Detector

Utilizing a well understood technology for the Focal Plain Detector (FPD), a monolithic silicon PIN-diode array was selected as the electron detector for the KATRIN system. PIN diodes meet the energy detection criteria for electrons of 5 to 50 keV. Furthermore, PIN diodes are easily manufactured into arrays on monolithic pieces of silicon and at sizes which cover the large flux tube area of 64 cm^2 at a 3 T detector magnet setting. An array on a single piece of silicon makes detector alignment easier since all of the pixels are guaranteed to lie in a single plane and be fixed in relation to each other. An array of pixels is resilient against single point failures reducing live time losses from dead channels. The KATRIN detector group selected CANBERRA as the manufacturer of the focal plane detectors.

A PIN diode is a three layer diode with a P-type and N-type layer sandwiching an intrinsic silicon layer. PIN diodes operate as a solid-state detector where ionizing radiation creates electron-hole pairs as it passes through the detector. The total number of electron-hole pairs created is proportional to the energy deposited in the active area of the detector. The small energy, 3.62 eV at 300 K, deposited per electron-hole pair reduces the statistical noise associated with the energy deposition. The statistical noise for radiation detectors is better than expected as the charge carrier creation is not a pure Poisson process. The statistical noise is often called the Fano noise and the reduction in noise is described by the Fano factor [28].

The entrance side of the wafer is uncoated and not pixelated offering 100 percent coverage of the magnetically imaged tritium source. The contact side of the PIN diode array mask, as seen in figure 3.1, has an inner quad-sected bullseye surrounded by 12 outer rings of 12 pixels each for a total of 148 pixels. Each pixel is fixed to an area of 44.1 mm^2 causing each pixel to have similar capacitances, hence similar noise characteristics. This dartboard design

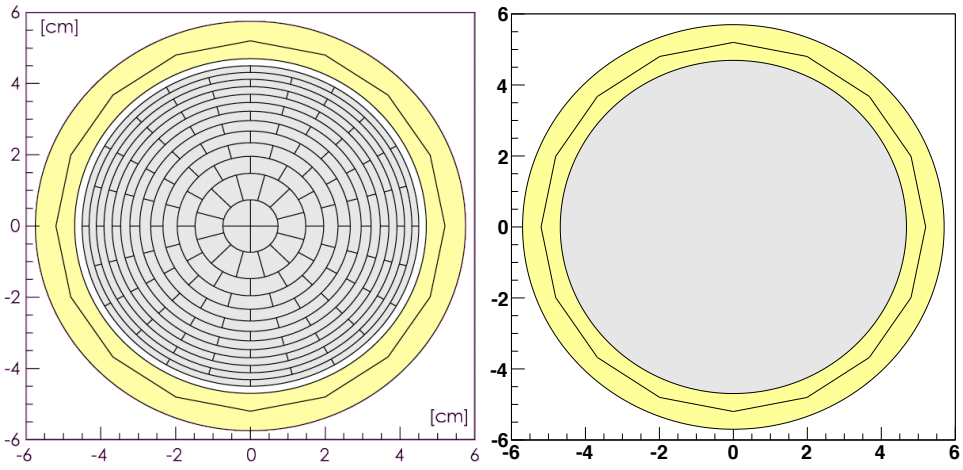

Figure 3.1: Focal plane detector layout. The left diagram shows the pixel segmentation on the junction or contact side of the detector while the right diagram is the ohmic or entrance side of the detector.

allows for imaging electrons from the spectrometer and hence one can apply corrections for any inhomogeneities in the magnetic and electric fields. The layout combined with the equal area of the pixels is a systematic check of the flux tube alignment since the count rate should be the same for each pixel in a ring. The 13th ring is the guard ring that can be biased at plus or minus 5 volts. The purpose of the ring is to minimize any field distortion on the outer ring of pixels. The reverse-bias voltage is applied to the set of contacts outside the guard ring. The reverse-bias contacts have a conductive path from the contact side to the entrance side. The typically used silver contacts can produce x-ray fluorescence at energies near the tritium endpoint increasing the background rates in our region of interest. So, the contacts are plated with titanium nitride chosen for its low background and non-oxidation properties.

Using a Optical Gaging Products, Inc. Smart Scope provided both a visual inspection of the purchased FPD's and a measurement of the pixel coordinates. All the coordinates were well within the design tolerance of .05 mm with an average measured tolerance of .0049 mm. Figure 3.3 displays the difference between the measured values and the specified values in radial coordinates. The pitch between contacts is 50 microns much less than the specified

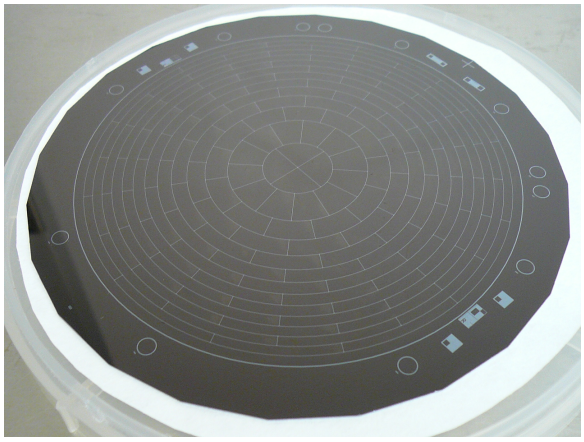

Figure 3.2: Photograph of the contact side of the focal plane detector.

300 microns. The detector thickness of 500 microns and pixel area of 44.1 mm^2 ensures a small pixel capacitance of approximately 9 pF.

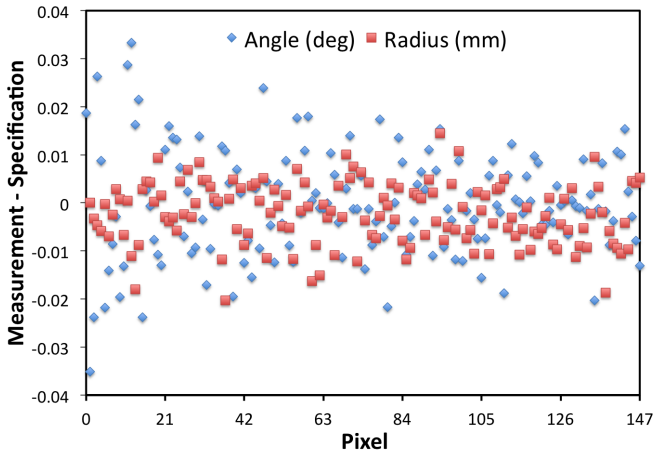

Figure 3.3: Pixel coordinate specifications subtracted from the measured values of focal plane detector 76041. The coordinates were measured with a precision optical microscope.

The room temperature leakage current for each FPD was measured by CANBERRA. An example of those results are shown in figure 3.4 for FPD 76041 and is reflective of the other purchased wafers. The KATRIN specification for the leakage current is less than .1 nA per pixel at 173 kelvin. Unfortunately, the KATRIN electronics does not have instrumentation

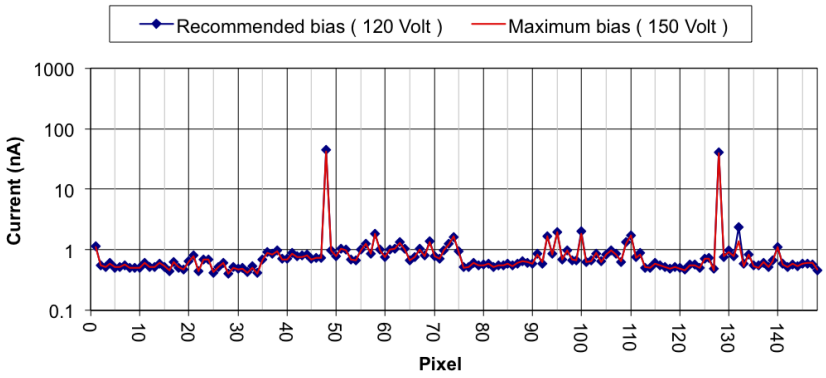

Figure 3.4: CANBERRA leakage current measurement for FPD 76041 measured at 20° C.

sensitive enough to measure this low level of a current. However, the detector leakage current is typically dominated by thermal excitation and obeys the probability function

$$p(T) = C * T^{3/2} e^{-\frac{E_g}{2kT}}$$

where T is the absolute temperature, E_g is the band gap energy, k is the Boltzmann constant, C is a material dependent proportionality constant[28]. The CANBERRA measurements were taken at 293 kelvin therefore a 120 kelvin temperature reduction should approximately reduce the leakage current by a factor of 10^7. As can be seen in figure 3.4 all the room temperature leakage currents are below 100 nA per pixel making them more than sufficient to meet the specification at 173 kelvin.

Such a large monolithic detector required a novel approach to connect the pixel pads in the extreme high vacuum to the preamplifiers located in the high vacuum region. A vacuum flange with 184 glass-insulated pin feed-throughs create the electrical connection from one vacuum chamber to the other. Mounted on each feed-through is a pogo-pin that makes the electrical connection to the pixel pad. A pogo-pin has an internal spring to ensure adequate pressure is being applied to the detector pad. Fifty newtons of total force is applied to the FPD from the pogo-pins. This mechanical stress deflects the center of the FPD .34 mm. Concerns arose about the mechanical stress degrading the detector performance, but

a study found that was no decline in performance under these strains [29].

3.2 Electronics and Data Acqusition

The Institut fur Prozessdatenverarbeitung und Elektronik at the Karlsruhe Institut fur Technolgy designed and built the focal plane detector electronics. The electronics needed to meet a large array of design concerns. Figure 3.5 details the FPD electronics setup. There are two paths: a signal path and a control path. The signal path begins with radiation deposition and charge collection in the FPD; then charge propagation and amplification from the preamps to the optical sender board; signal digitization in the KATRIN DAQ crate; and finally data readout by the ORCA real-time data acquisition program.

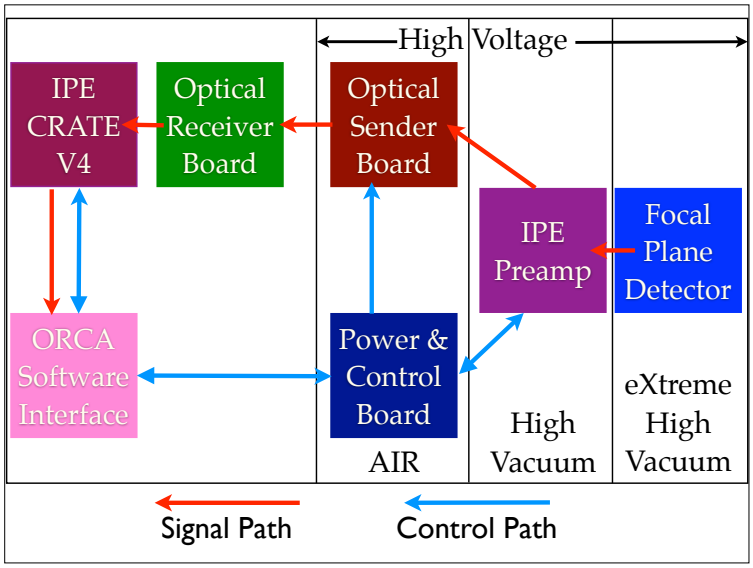

Figure 3.5: Focal plane detector electronics block diagram.

The front-end electronics are mounted close to the detector within the vacuum system in a preamp carousel consisting of 24 modules instrumenting the 148 pixels. Four modules that contact the 4 interior pixels have seven channels, while the remaining modules have six channels. Each preamplifier used a IF1320 FET during commissioning data taking at the University of Washington. The modules allow board temperature monitoring while

supplying both the FPD reverse bias and guard ring voltages. Each preamp has leakage current monitoring, single channel electronic pulse injection and charge amplification of FPD signals. Typical signals from the preamplifiers have a rise-time of 250 ns and fall time of 1 ms.

The Power and Control (PAC) board provides the control and monitoring interface to the front-end electronics and optical sender boards. It also provides the power regulation for those components. The PAC board's programmable Peripheral Interface Controller communicates with the ORCA and the ADEI slow control systems via RS232 serial communication. It provides monitoring of leakage currents, vacuum temperatures and the reverse bias voltage. It relays the variable gain settings to the Optical Sender board. An optical pulse input for electronic pulse injection used for calibration is routed to the front-end of the preamplifier by multiplexers controlled by the PAC board.

The signals from the 148 preamp channels are connected to four optical sender boards paired with optical receiver boards interfaced to the KATRIN DAQ crate. The FPD, PAC board and optical sender board can all be elevated to high voltage with the post-acceleration electrode. The optical sender and receiver boards isolate the KATRIN DAQ crate from the high voltage region. Another of the design requirements for the KATRIN electronics was the ability to study the alpha backgrounds, which occur at much higher energies than the electrons from tritium beta decay. In order to examine both the kiloelectronvolt electrons and the megaelectronvolt alphas the optical sender board has a programmable gain stage.

The KATRIN IPE crate performs the analog to digital signal conversion. Each channel's signal is processed through a series of band pass filters and a programable amplifier leading to serial 20-Mhz 12-bit ADCs. An FPGA implements three measurement modes: energy, trace, and histogram. Energy mode is the primary operation mode for KATRIN. The analog signal is passed through a programmable trapezoidal filter providing an energy value, with an associated time stamp and event ID. Trace mode is a diagnostic mode that digitizes the full charge signal into a digitized waveform as well as providing the same information as energy mode. Histogram mode creates histograms of energy data in set time intervals. This mode loses the ability to analyze event by event data but gains the ability to run dead time free with rates as high as 1MHz during calibrations.

A series of two trapezoidal filters determines an event's energy and time. The output O_i at a time bin i of a trapezoidal filter is the difference between two rolling windows. Each window is a sum of length L time bins of ADC values v_i sampled in 50-ns time bins. The two windows are separated by a gap length of G time bins.

$$O_i = \sum_{j=0}^{L} v_{i-j} - \sum_{k=L+G}^{2L+G} v_{i-k} \tag{3.1}$$

The length L determines the amount of filtering while a gap length larger than the signal rise time prevents variations in the output [26]. A signal, after passing through the first filter, is passed through the second filter of length L/2. The second filter provides the derivative of the first filter where the zero crossing corresponds to the maximum of the previous filter. The maximum occurs 3L/2 bins before the zero crossing. A triggered event occurs if the maximum of the first filter is above a set programable threshold.

3.3 Focal Plane Detector and Electronics Characterization

The initial electronics and focal plane detector characterization was performed at the University of Washington using a test vacuum chamber designed by Greg Harper. The test vacuum chamber's simple assembly as compared to the full detector vacuum section allowed for easy access to the vacuum electronics while characterizing their performance and behavior. The chamber is equipped with a pulse tube cooler that provides a constant cold source for cooling the in-vacuum electronics. A set of two heating resistors and a PT-1000 platinum Resistive Temperature Detector (RTD) connected to the preamplifier mounting plate maintain a set point temperature via a PID control loop implemented in the ORCA software system. The americium calibration source as described in section 2.4.5.1 is attached to a rotating arm that moves the source in and out from under a stainless steel shield. At this stage the operation temperature, reverse bias voltage, and shaping parameters were optimized.

After completing these initial measurements, the electronics and FPD detector were assembled into the KATRIN detector system. The system as described previously has several calibration sources including the same americium source used in vacuum chamber

testing, a photo-electron source, an electronic pulser, and a LED pulser. These devices were used to determine the detector's linearity and energy resolution. They were also used in conjunction with measurements of the KATRIN detector backgrounds, to evaluate the figure of demerit, and measure the focal plane detector dead layer as detailed in subsequent chapters.

3.3.1 Optimal Operating Temperature

As stated in section 3.1 the leakage current in the FPD decreases with decreasing temperature. The decreased leakage current improves the detector resolution and a similar effect should improve the performance of the FET in the preamplifier. The charge carriers in the FET do have a freeze out point where the FET will stop working at too low of temperatures. Also, the performance of the preamplifier does not necessarily improve with decreasing temperature. The FPD detector temperature is coupled to the preamp temperature via the FPD feedthrough vacuum flange and a single source cools both elements. This forces one to find a balance between the FPD and preamplifier temperatures.

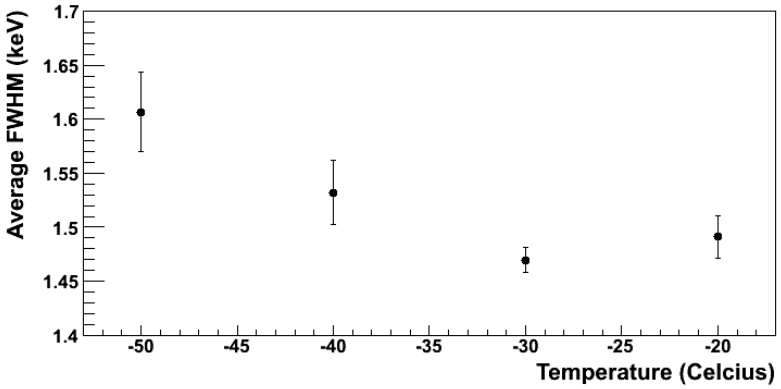

Figure 3.6: Measurement of the focal plane detector's resolution temperature dependence.

The ^{241}Am source was used to illuminate the FPD at four different temperature settings $-20°, -30°, -40°$, and $-50°$ celsius. The resolution of the detector is measured from the width of a Gaussian fit of the 59.4 keV peak. Figure 3.6 displays the average FWHM

across the FPD versus temperature set point. There is a clear minimum at the $-30°$ C of 1.47 ± 0.01 keV.

3.3.2 Reverse Bias Voltage

A completely reversed biased or fully depleted focal plane detector is necessary to maximize detector resolution and efficiency. Charges in an unbiased semiconductor detectors suffer from recombination causing incomplete charge collection. This reduces the gain as well as the energy resolution of the detector. The depletion region is the active region of the detector where charge collection occurs. The depletion region is small in unbiased detectors causing a loss in efficiency and an increase in the detector's capacitance. The large capacitance further degrades the noise properties of the detector.

For this measurement the FPD was illuminated by an ^{241}Am source at different reverse bias settings for equal amounts of time. The resolution of the detector is again measured using the width of a Gaussian fit of the 59.4 keV peak. This peak remains distinguishable above the changing noise floor as the voltage settings are changed. Figure 3.7 displays the average FWHM across the FPD versus reverse bias. The plot sharply falls from 0 to 40 volts and then asymptotes out.

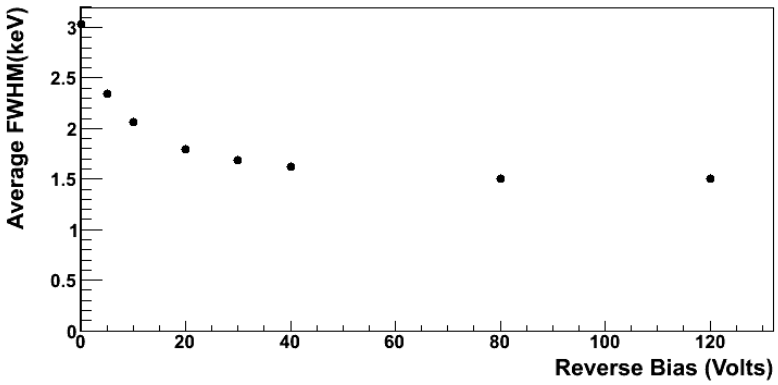

Figure 3.7: Focal plane detector resolution reverse bias dependence at a temperature setting of $-20°$ C and shaping time of 6.4 μs.

A measure of the detector efficiency as a function of voltage can be inferred from the rate

in the 59.4 keV peak. As the bias voltage increases the active detection region increases, this increases then the number of detected 59.4 keV gammas from the americium source. The rate is calculated from the area in the peak divided by the run time. In figure 3.8 the rate for each voltage setting is plotted versus the pixel number. At 80 volts the rate reaches a maximum.

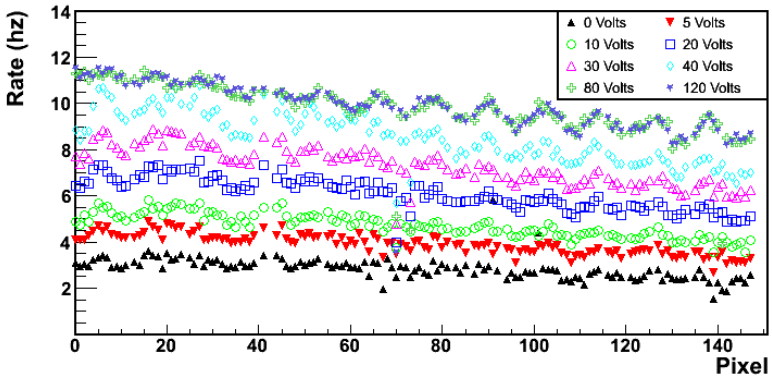

Figure 3.8: Focal plane detector rate in 59.4 keV peak of an ^{241}Am for different reverse-bias voltages. The rate was calculated from the counts in the peak weighted by the run time.

A feature of note in the plot that does not affect the result is the downward linear decrease superimposed with an oscillation in rate as pixel number increases. The trend is caused by the source being positioned near but not exactly at the center of the FPD. The pixel numbering scheme starts in the center and spirals outward. Both the resolution and efficiency maximize at 120 volts verifying CANBERRA's voltage set point. The voltage set-point was not taken past 120 volts as a precaution against damage to the detector.

3.3.3 Optimal Shaping Time and Gap Length

The trapezoidal filter implemented in the KARTIN IPE digitizing crate has two adjustable parameters, a filter length and a gap length(Section 3.2). The optimal filter length in respect to energy resolution averages out the effects of high frequency noise without introducing the effects of low frequency noise. Optimizations of both parameters were based on the resolution of the 59.4 keV peak width of the ^{241}Am.

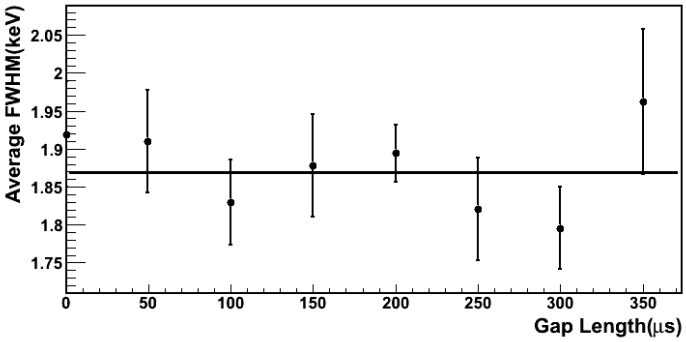

Figure 3.9: Focal plane detector resolution dependence for different gap length settings at a shaping length of 3.2 μs.

The gap length settings span from 0 to 350 nanoseconds in 50 nanosecond increments for a total of 8 set points. The filter gap was investigated at a filter length setting of 3.2 μs. The gap length setting does not have a clear optimal value. Data plotted in figure 3.9 is consistent with a constant polynomial at 1.87 ± 0.02 keV with a χ^2/d.o.f. of 5.13/7. In general, the gap length in most data runs was set to 200 ns.

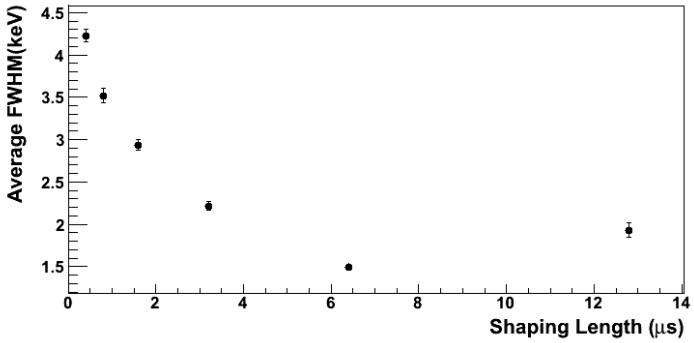

Figure 3.10: Focal plane detector resolution for different shaping lengths at gap length of 200 ns.

There are 8 possible set points for the filter length, but only 6 were tested since the 100 ns and 200 ns filter lengths are not viable settings. A clear minimum occurs in figure 3.10 at the 6.4 μs setting of 1.49 ± 0.02 keV. The optimal shaping length is larger than what is expected from Spice simulations (Figure 3.11). The simulations both for a 1 nA and 100 pA

input leakage current have an optimal shaping time of 3.2 μs. The resolution values of 1.2 and .8 keV respectively are much better as well, implying there are additional noise sources not included in the simulation.

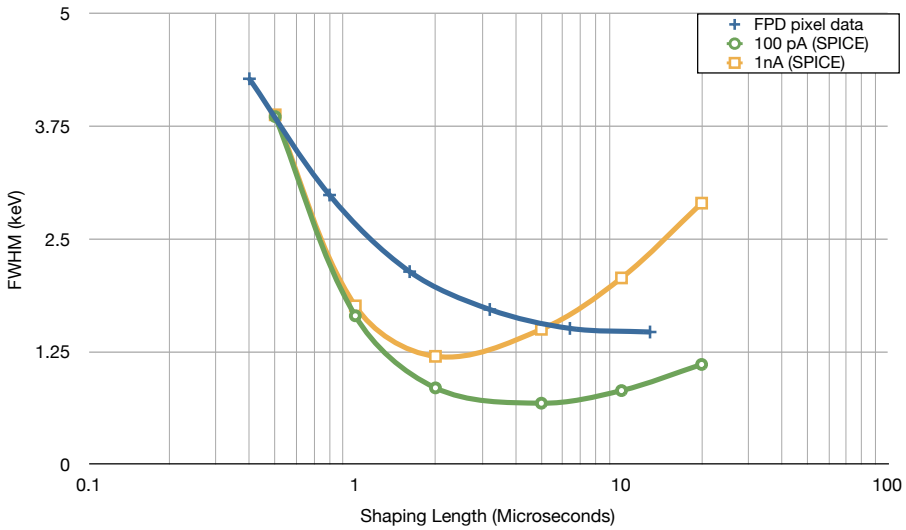

Figure 3.11: Resolution estimates from SPICE simulations of KATRIN preamplifiers with 100 pA (green) and 1nA (yellow) input leakage current at different shaping lengths. (Blue) A representative measurement of resolution at different shaping lengths from a single channel of the focal plane detector.

The larger shaping time effects the pile up probability

$$1 - exp[R * T] \tag{3.2}$$

where R is the true event rate and T is the minimum time separation for the DAQ to resolve separate events. The resolving time for the KATRIN's DAQ is 3/2 the shaping length L. Table 3.1 shows the percentage pile-up for different event rates. The pile-up rate approaches 1 percent as the true rate reaches 1 kHz.

Table 3.1: Percentage percentage of pile-up for shaping lengths of 3.2 μs and 6.4 μs.

Rate (kHz)	Percent Pile-Up	
	3.2 μs	6.4 μs
0.1	0.05	0.096
1	0.48	0.96
10	4.7	9.1
100	38	62

3.3.4 System Linearity

Optical pulse injection into the FPD and electronic pulse injection in the preamplifier front-end were used to measure the system's integral linearity. The integral linearity is measured by injecting pulses of different known amplitudes (intensity in the optical case) and measuring the ADC channel number. A best-fit line is found on a plot of ADC channel versus pulse amplitude. The largest precent deviation from the best fit line and ADC channel value is the non linearity.[28] The RMS integral linearity over all pixels is .34 percent for optical pulsing.

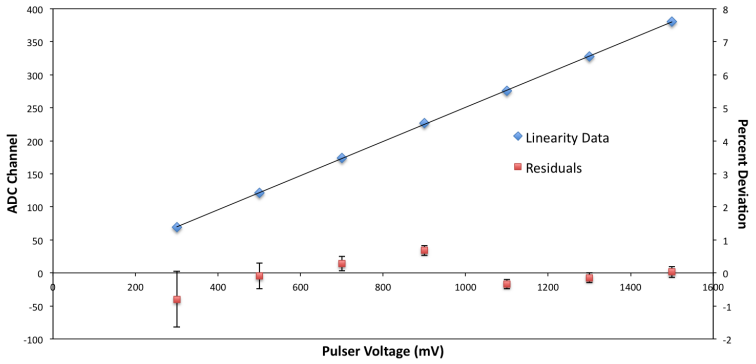

Figure 3.12: Measurement of FPD electronics linearity from optical pulse injection for representative pixel 31. The blue squares are the mean ADC channel (left vertical axis) plotted against the pulser input voltage and fitted with a line. The red diamonds are the residuals (right vertical axis) between the blue square data and the best-fit line.

Figure 3.12 shows the linearity and fractional difference for pixel 31. There is a clear step in the fractional difference as the voltage transitions from .9V to 1.1V. Typically, this plot is expected to be quadratic in behavior, where the greatest differences are expected to be at

the end points. The Agilent pulser has an internal attenuation network that switches from one setting to another as it spans voltage ranges to maintain its linearity. This caused the step behavior and was verified with an external attenuator that shifted the step the location in the ADC channel while maintaining the same place in voltage amplitude. Electronic pulse

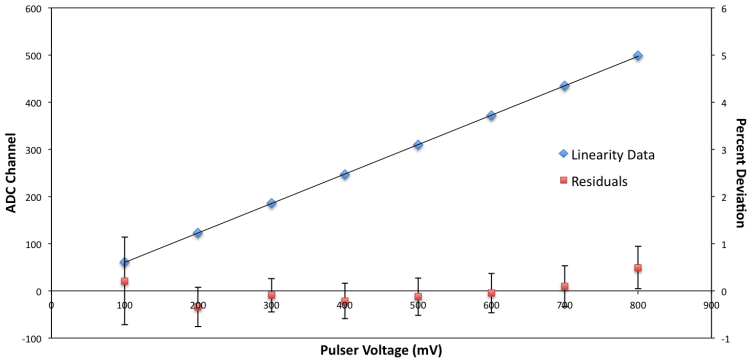

Figure 3.13: Measurement of FPD electronics linearity with electronic pulse injection for representative pixel 31. The blue squares are the mean ADC channel (left vertical axis) plotted against the pulser input voltage and fitted with a line. The red diamonds are the residuals (right vertical axis) between the blue square data and the best-fit line.

injection measured a lower RMS integral linearity of .28 percent over all pixels. The lower RMS is due to independence from the step non-linearity caused by the Agilent pulser. For electronic pulser injection the Agilent pulser is used over a different range that avoided the internal switching. This is illustrated in the characteristic quadratic shape of the fractional deviation plot in figure 3.13

3.3.5 Energy Resolution

Three different calibration sources were used to measure the detector resolution. Electronic pulse injection also gives a measure of the resolution independent of the physics from radiation deposition in the detector. The width of the 59.4 keV americium peak measures the gamma resolution while an electron source provides resolution measures at a variety of electron energies.

Figure 3.14 is both the electronic and americium resolution measurement for each work-

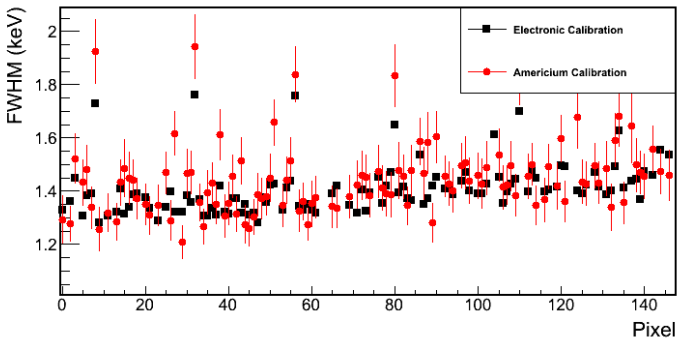

Figure 3.14: Electronic and Americium measurement of FPD resolution.

ing pixel. The average resolution across the focal plane detector for the electronics calibration is 1.38 ± 01 keV (FWHM), while the average americium resolution is 1.41 ± 01 keV (FWHM). As expected the electronic resolution is slightly lower than the americium resolution since it is independent of physics effects such as the Fano factor (sec. 3.1).

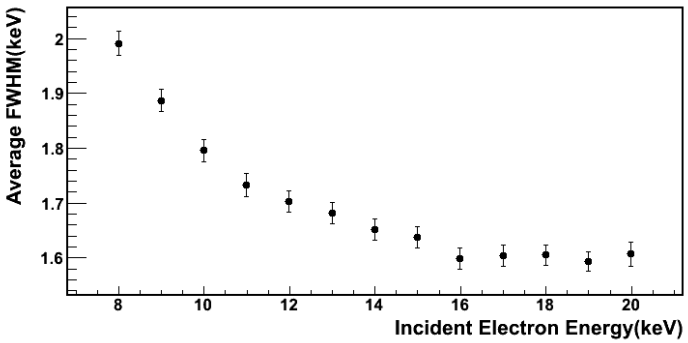

Figure 3.15: Electron source measurement of focal plane detector energy resolution averaged over the entire array.

The resolution is 1.60 ± 02 keV (FWHM) for 18.6 keV electrons without a magnetic field. This FWHM is larger than that for the americium because of backscatter and dead layer effects. The gammas deposit energy via point interactions uniformly throughout out the bulk of the detector, while the electrons deposit energy continually starting at the surface of the detector. For electrons, energy straggling through the dead layer and back scattering

broaden the peak. A scan of electron energies in 1 keV increments from 8 to 20 keV in figure 3.15 shows that the resolution degrades with decreasing electron voltage. The amount of backscatter and energy loss in the detector increases with decreasing energy.

Chapter 4

DETECTOR SYSTEM BACKGROUNDS

Detector system related backgrounds contribute to the overall uncertainty of the KATRIN measurement. Intrinsic radioactive decay in the detector assembly materials and cosmic rays are the major contributors to detector backgrounds. A background rate of less than 1 mHz is the design goal for the detector system. In order to achieve this goal KATRIN employs a set of background reduction methods: a muon veto and a pixel to pixel anticoincidence method.

4.1 Measurement

A background measurement was done during commissioning in Seattle mimicking the final KATRIN setup best as possible. The major discrepancies from the final KATRIN setup at KIT are the physical location of the detector system and a lack of a main spectrometer. The local background sources of the University of Washington physics basement are different than from the surface location at KIT. Also, the main-spectrometer does not exist at the University of Washington and is replaced by a stainless blank-off flange. The americium source was removed from the apparatus and the electron gun was in its stored position at the top of the chamber. The magnetic fields were set to their nominal values of 3.6 T on the detector magnet and 6 T on the pinch magnet. Focal plane detector data were acquired over a period of 8 hours in order to obtain sufficient statistics for the analysis. Figure 4.1 shows the background energy spectrum of the focal plane detector system.

Table 4.1: Detector system background rates summed over 127 operating pixels and scaled to 148.

ROI (keV)	Average Background Rate (mHz/keV)
10-30	3.21 ± 0.08
120-300	1.96 ± 0.02

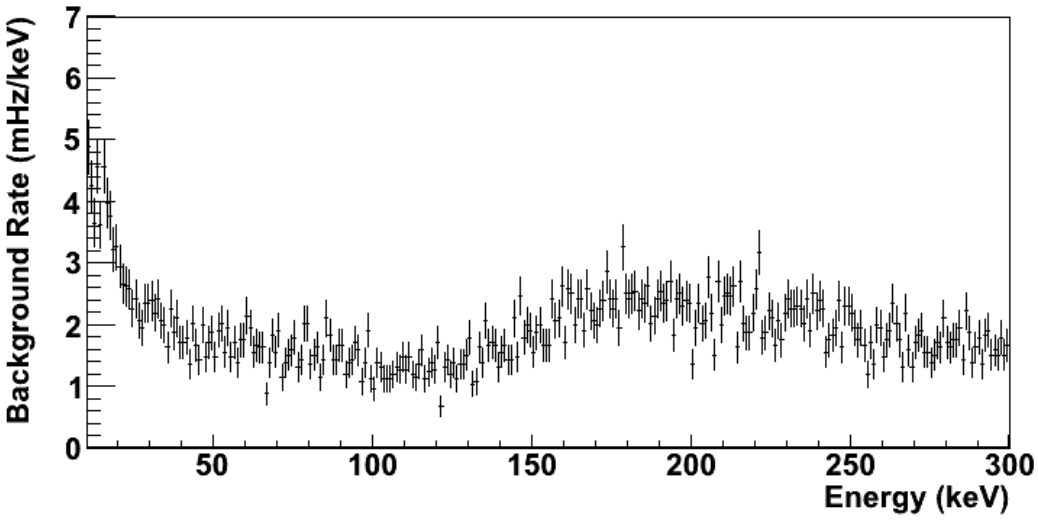

Figure 4.1: Raw background energy spectrum measured by the focal plane detector summed over 127 operating pixels and scaled to 148 at nominal magnetic field settings.

Background rates were evaluated in two regions of interest, a low energy region from 10 to 30 keV and a high energy region from 120 keV to 300 keV. The low energy region of interest corresponds to an area around the tritium end-point, while the high energy region corresponds to the minimum ionizing peak that can be seen in the energy spectrum in Figure 4.1. The two regions of interest let us evaluate the effectiveness of background cuts discussed in the next sections.

4.2 Background Cuts

4.2.1 Active Veto Cut

The veto system employs a set of scintillating veto panels: four barrel and two crescent moon panels (Figure 4.2). Wave length shifting (WLS) fibers loop through each panel. Clear optical fiber couples each end of the WLS fiber to an individual multi-pixel photon counter (MPPC). The MPPCs are temperature controlled to -10C to reduce the dark current.

MPPCs have a large dark rate of ∼20kHz at -10C and the scintillating fibers have a low photon output. In order to quantify the cosmic ray sensitivity the DAQ threshold would

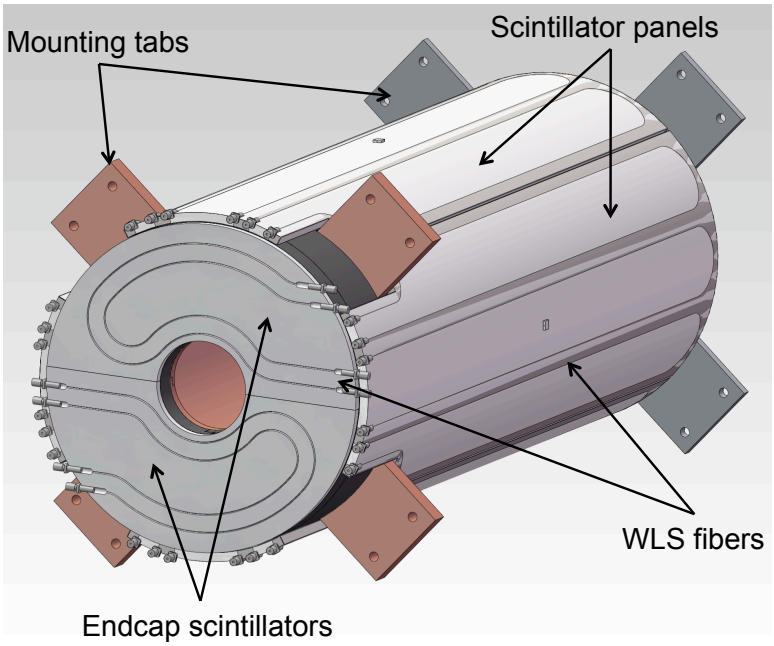

Figure 4.2: Layout of the detector veto panels.

have to be set to the single photon level. At this threshold the dark rate causes dead time in the KATRIN DAQ crate. Also the accidental rate with focal plane detector data causes a non negligible loss of good data. In order to avoid these problems and attain a high veto efficiency, the IPE firmware is being designed with a coincidence trigger for events on a single panel. Unfortunately, at the time of local commissioning this firmware was not available.

Instead, for the Seattle based commissioning, each MPPC channel is connected to the KATRIN DAQ crate front-end via an analog summing board. The summing boards provide an output to the DAQ crate for each MPPC pulse for individual readout, an analog sum signal of all MPPC channels for each scintillator panel and a trigger signal for that sum. Summing the MPPC outputs allows the sum threshold to be raised above the single photon level. The time separation of photons generated in a panel is small compared to the pulse width of the MPPCs allowing good overlap of MPPC pulses from multiple fibers. However, since this is not a true coincidence, single multi-photon dark events from a MPPC channel can cause a trigger. This rate however is reduced greatly from the single photon dark rate

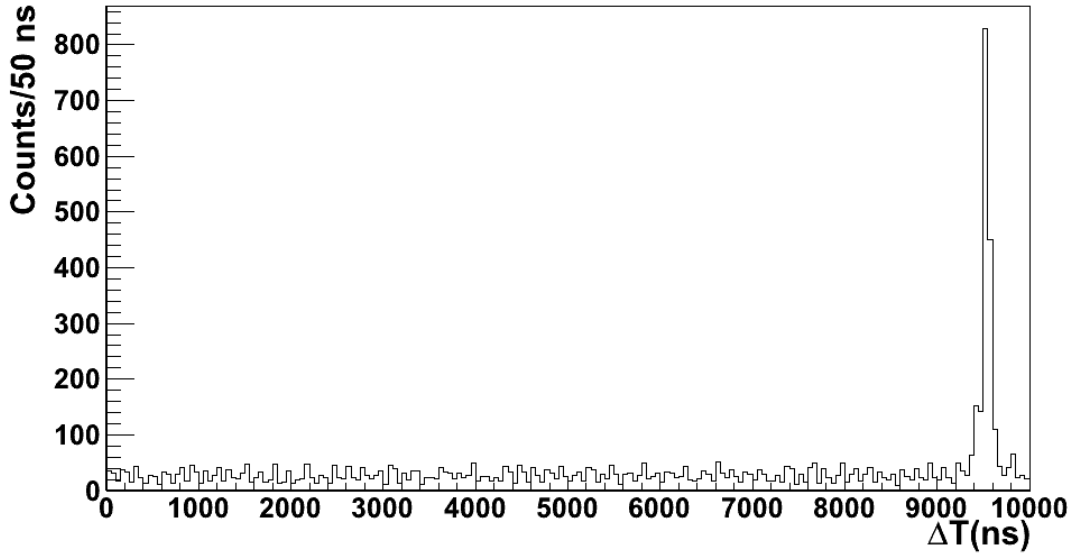

Figure 4.3: Timing correlation plot between focal plane detector events and veto events. The x-axis represents the time difference between a focal plane detector event and the last fired veto event.

of 6 MPPCs in a sum.

The MPPCs for each panel were grouped together in each sum creating a total of six veto trigger signals. A set of dip switches on the summing board set the threshold of the voltage level trigger for each sum signal. If the sum signal is fired a NIM logic pulse is generated and a veto event is recorded. For data storage reasons only the sum trigger is recorded into the data stream. This is sufficient to provide an event stamp for a coincidence analysis with the focal plane detector, but individual channels information and the energy of the sum is lost.

The veto cut is applied as an offline data cut that removes focal plane detector events from the final analysis when they are within a specified time window of a veto event. The window width and delay relative to the veto signal is determined by measuring the time correlation between focal plane detector events and veto events. Figure 4.3 is a plot of FPD rate versus time since a veto event occurred. At approximately 9.5 microseconds there is a clear coincidence peak between the veto events and focal plane detector events. A 1 μs

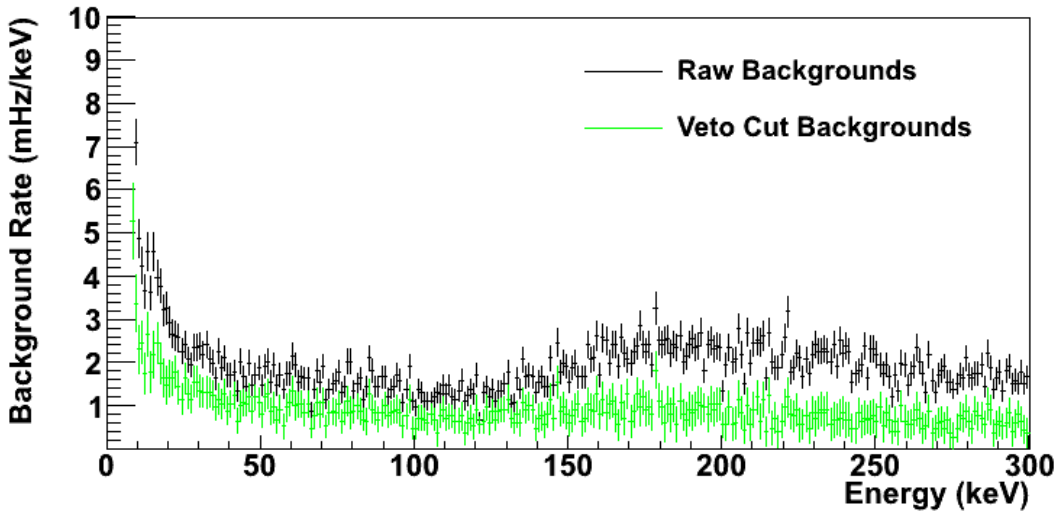

Figure 4.4: Raw background energy spectrum(black) and veto-cut background energy spectrum (green). Both spectra are summed over 127 operating pixels and scaled to 148 pixels.

window centered around this peak was chosen as the coincidence window width.

The location of this peak is a result of the two different shaping times used by the veto and focal plane detector system. A trapezoidal filter is used to determine the energy and trigger times of both event types in the KATRIN DAQ crate. The trigger time occurs 3/2 shaping times after the beginning of an event pulse for a zero gap length[26]. The gap length adds an additional time of half its length. The veto has a shaping time of .200 μs and a gap length of .050 μs while the focal plane detector shaping time is 6.4 μs with a gap length of .400 μs. For a veto and focal plane detector event occurring at the same time with these settings there will be a 9.475 μs time difference in their recorded trigger times.

Table 4.2: Veto cut background rates summed over 127 pixels and scaled to 148.

ROI (keV)	Background Rate (mHz/keV)	Veto Coincidence Rate (mHz/keV)	Post Veto Cut Rate (mHz/keV)	Cut Efficiency
10-30	3.21 ± 0.08	1.42 ± 0.05	1.79 ± 0.06	44%
120-300	1.96 ± 0.02	1.18 ± 0.01	0.78 ± 0.01	60.2%

The veto cut reduces the low energy backgrounds by 44 % to 1.79 ± 0.06 in the low

energy region of interest. It is more efficient in the high energy region removing 60.2% of the backgrounds. The efficiency difference occurs because the veto panels are very efficient at detecting cosmic ray muons but not cosmic ray photons. According to Monte Carlo studies done by Michelle Leber, cosmic ray photons have a low probability of being detected in both the veto and the focal plane detector[26]. They can produce lower energy secondary photons that are detected in the focal plane detector.

4.2.2 Multi-Pixel Cut

Independent of the veto system another method to reduce backgrounds is the multi-pixel cut. This cut removes time correlated events in pixels from the analysis. The logic behind the cut is that focal plane detector events from the tritium source are uncorrelated. As stated earlier, a tritium decay produces an electron, a neutrino and the recoil nucleus. Only the electron is detectable in KATRIN. On the other hand, some background events do occur in a correlated manner. An example of such events are cosmic rays creating a showers of secondary particles. The segmentation of the focal plane detector enables a correlation analysis to be done between events in different pixels.

The appropriate time window is determined by examining the histogrammed time differences in figure 4.5. The histogram shows a very prompt event peak for Δt less than 200 ns that falls off quickly to 3 μs. A 1 μs coincidence window was selected for the cut.

Using the same ROI energy windows defined in the veto cut section 4.2.1, backgrounds in the low energy region are reduced by 62.9 percent. The high energy region backgrounds are reduced by 39.2 percent as listed in Table 4.3.

Table 4.3: Multi-pixel cut background rates summed over 127 operating pixels and scaled to 148 pixels.

ROI (keV)	Background Rate (mHz/keV)	Multi-Pixel Cut Coincidence Rate (mHz/keV)	Post Multi-Pixel Cut Rate (mHz/keV)	Cut Efficiency
10-30	3.21 ± 0.08	2.02 ± 0.05	1.19 ± 0.04	62.9%
120-300	1.96 ± 0.02	0.77 ± 0.01	1.17 ± 0.01	39.2%

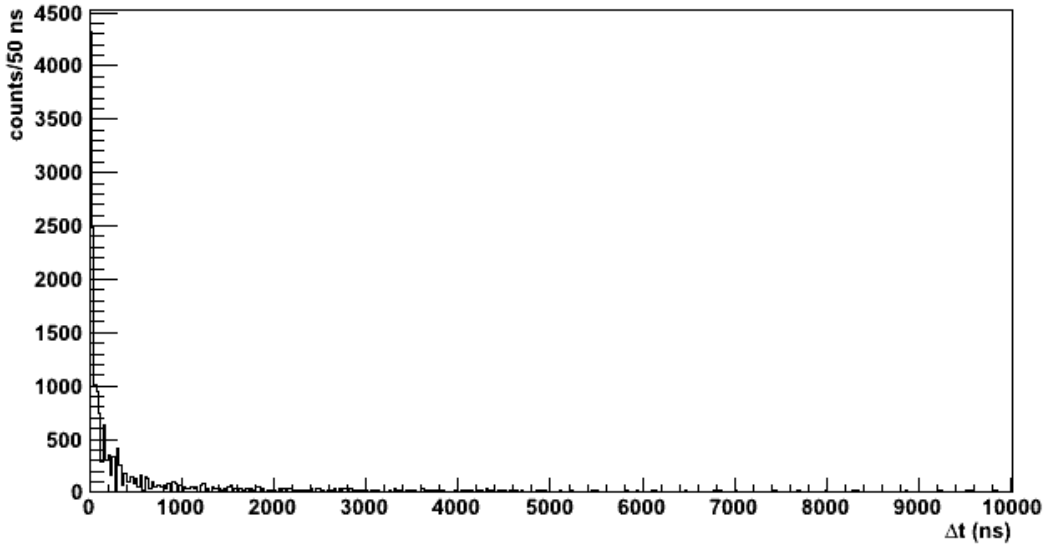

Figure 4.5: Timing correlation between pixels on the focal plane detector. The plot represents the time differences between events on different pixels.

Two concerns arise from the multi-pixel cut. First, for high data rates the accidental coincident rate becomes a concern. Secondly, charge splitting events are removed by this cut as well.

The derivation of the accidental coincidence rate for a 148 channel detector can be derived from the two channels coincidence rate $r_a = \tau r_1 r_2$, where τ is the coincidence window and the single rates r_1, r_2 for the two channels[28]. Each pixel is expected to have roughly the same singles rate for nominal field settings. The tritium source and backgrounds uniformly illuminate the detector and each pixel in the detector is the same area. Hence, the total accidental rate R_a is the number of pair combinations in the set of 148 pixels. In this setup a pixel can self coincidence, so repetitions are allowed leading to equation 4.1 .

$$R_a = \binom{148+2-1}{2}\tau r^2 = \frac{149!}{2!147!}\tau r^2 = 11026\tau r^2 \tag{4.1}$$

Evaluating equation 4.1 for a 1 microsecond window the accidental rate is 1.2 mHz for 1 Hz singles rate.

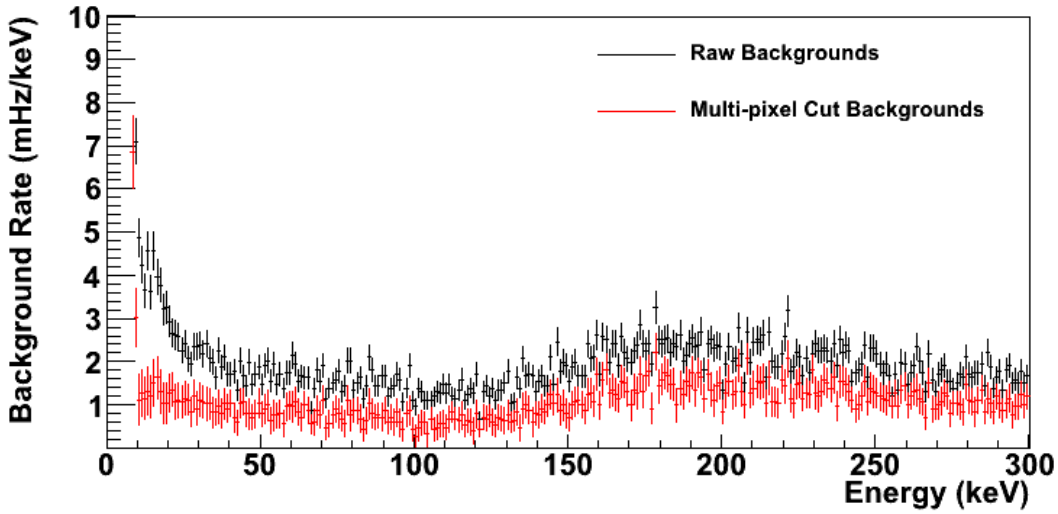

Figure 4.6: Raw background energy spectrum(black) and multi-pixel cut background energy spectrum (red). Both spectra are summed over 127 operating pixels and scaled to 148 pixels.

The other concern from this technique is losing events due to charge splitting at pixel boundaries. Charge splitting can occur when a particle interacts in the pixel boundary region. As discussed in section 3.1 the focal plane detector has a monolithic entry window and is pixelated on the opposite side. The pitch between pixels is 0.05 mm. The ratio of the total channel area to the total detection area gives an upper limit of 2.4 % for the charge splitting effect. The actual probability is smaller since electric field lines from detector bias is continuous across the detector entry surface and end on one of the pixelated surfaces on the rear. Near the boundary region the charge generated by a particle can follow separate field lines to separate pixels. An analysis of electron and americium data by Sanshiro Enomoto shows the charge splitting probability is less than 1%[30].

4.2.3 Summary of Background Cuts

Combining both the veto cut and multi-pixel reduces the low energy backgrounds to 0.89 ± 0.04 mHz/keV in the low energy region (Table 4.4). As expected, the two cuts have a significant amount of overlap leading to higher rates than one would expect if the two cuts were independent. The overlap in the two cuts gives a robustness against inefficiencies in

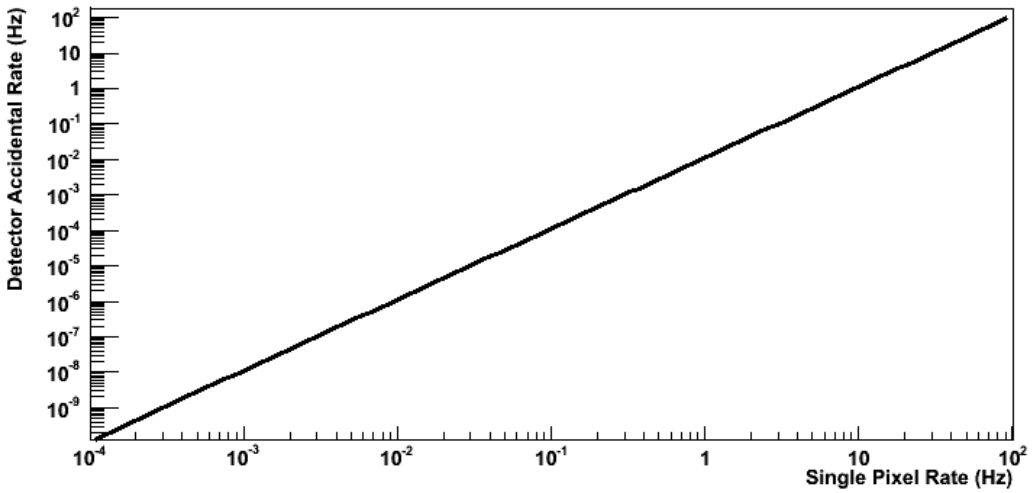

Figure 4.7: Multi-pixel cut accidental rate for τ=1 μs window.

the veto system.

Table 4.4: Combined veto and mulit-pixel cut background rates summed over 127 operating pixels and scaled to 148 pixels.

ROI (keV)	Background Rate (mHz/keV)	Post Cut Rate (mHz/keV)	Total Cut Efficiency
10-30	3.21 ± 0.08	0.89± 0.04	72.0%
120-300	1.96 ± 0.02	0.53 ± 0.01	72.9%

4.3 Post Acceleration

An alternative approach to reducing backgrounds is to shift the signal to a lower background region. Examining the zoomed uncut background spectrum in figure 4.9 the background rate decreases as the energy increases. This was the impetus for the addition of a post-accelaration electrode to the detector design. The electrode can be set to a positive potential that boosts the source electrons higher energy than their initial 18.6 keV .

The electrode was tested at three different potential settings of 7.75, 10, and 12 kV. The electrode is designed to carry up to 20 kV but instabilities at higher voltages led to

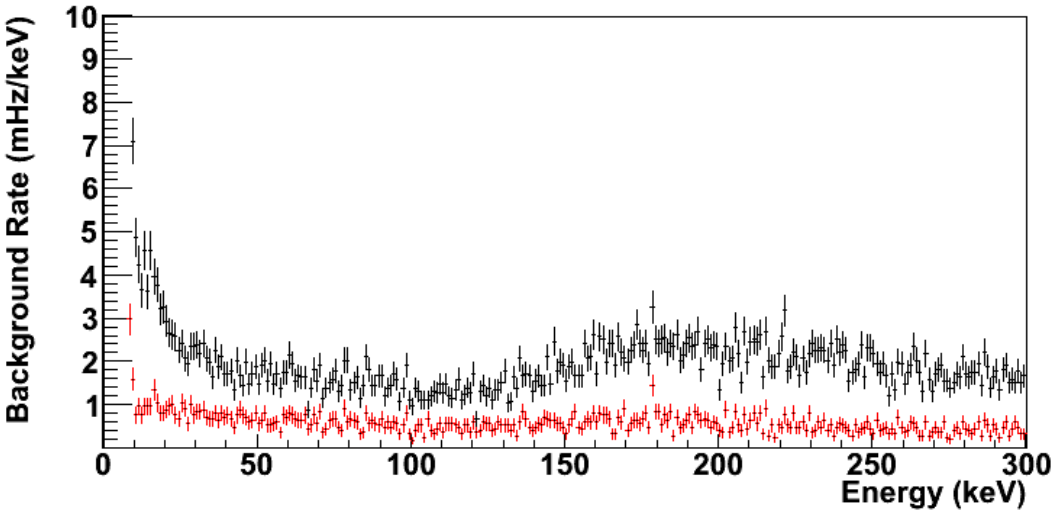

Figure 4.8: Raw background energy spectrum(black), and combined veto and mulit-pixel cut background spectra (red). Both spectra are the summed rates of 127 operating pixels and scaled to 148 pixels.

discharges. In order to protect the commissioning electronics from high voltage discharge the voltage settings were limited to 12 kV. Measured rates for post-acceleration backgrounds are given in Table 4.5.

Table 4.5: Post-acceleration electrode background rates for a region of interest from 10 to 30 kV. The rates are summed over 127 operating pixels and scaled to 148 pixels.

Post Acceleration Voltage (kV)	Background Rate (mHz/keV)	Cut Background Rate (mHz/keV)
0	3.21 ± 0.08	0.89± 0.04
7.75	4.16 ± 0.1	1.91± 0.07
10	5.59 ± 0.1	3.36± 0.08
12	8.7 ± 0.1	5.7± 0.1

An initial review of the results in table 4.5 indicates that a potential applied to the post-acceleration electrode has a detrimental effect on the detector background rate. As the potential is increased from 0 to 12 kV the background rate increases 271%. Examination of the background spectra in figure 4.10 show that peaks appear in the spectrum when a

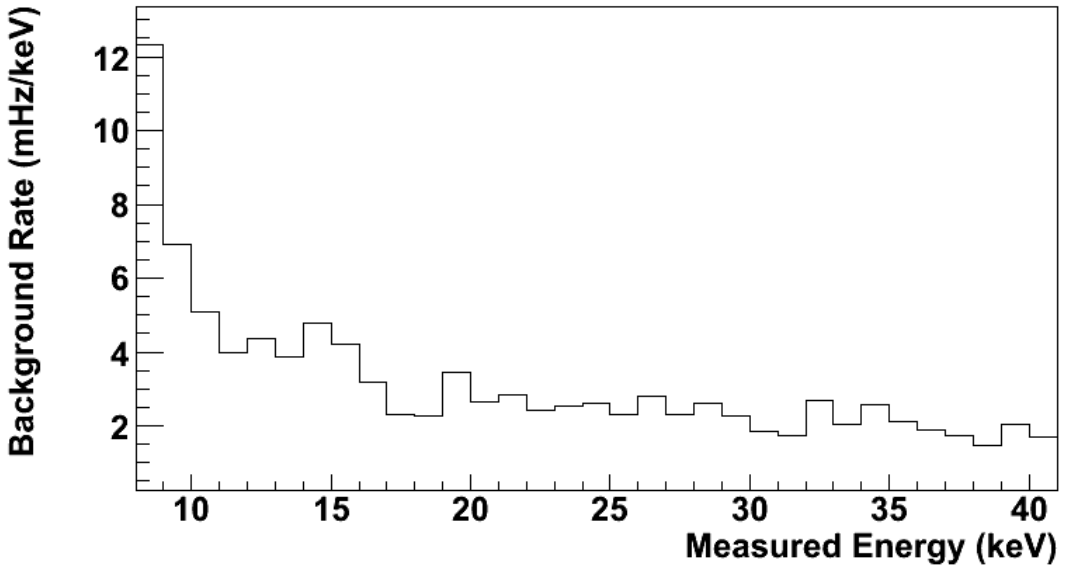

Figure 4.9: Raw background spectrum with 0 kV on the post-acceleration electrode. The spectrum is summed over 127 operating pixels and scaled to 148 pixels.

voltage is applied. For instance a large peak is observed in the 12 kV spectrum centered just below 12 keV. This occurs both in the 7.75 and 10 keV spectra, though the 7.75 peak is hard to discern as its closer to the detector threshold. Also there are secondary and tertiary peaks at multiples of the set potential voltage.

The cause of the increased backgrounds must be the result of negatively charged particles being accelerated by the potential of the post-acceleration electrode. Also, the particles must initially have very low energies since the primary peaks are just below the set point of the electrode. The most likely source of these particles is extremely low energy electrons generated from the main-spectrometer blank-off flange. Possible physics mechanisms for the generation of these electrons is shake-off electrons from surface alpha decays on the flange and ionization caused by cosmic rays passing through the flange. These background electrons should not be generated in the final KATRIN setup, as the flange will be replaced by the main-spectrometer volume.

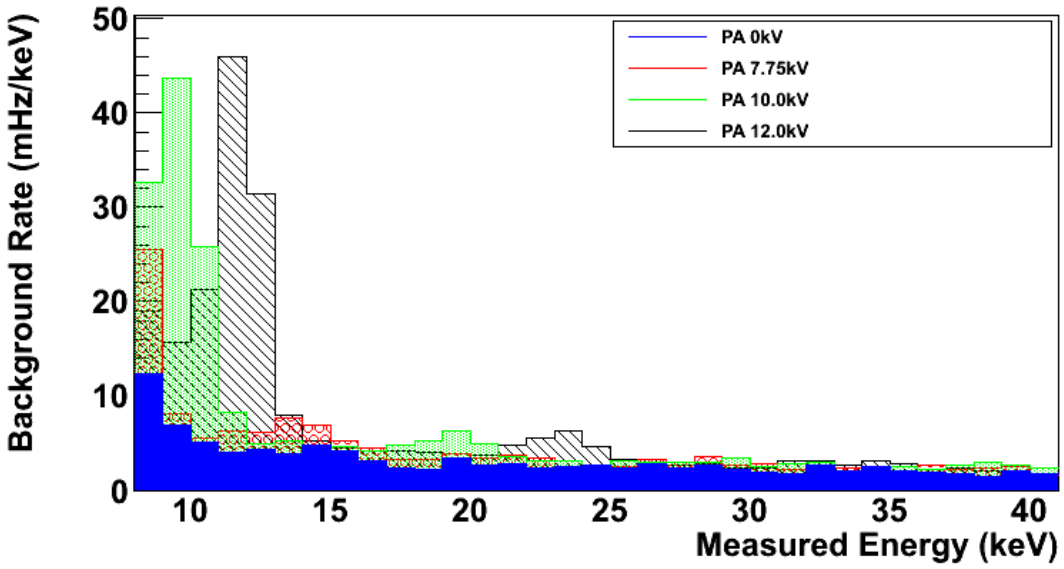

Figure 4.10: Background spectra for post-acceleration electrode voltage settings: 0 kV (blue), 7.75 kV (red), 10.0 kV (green), 12.0 kV (black). The measured spectra are summed over 127 operating pixels and scaled to 148 pixels.

4.4 Simulation and Measured Background Comparisons

Michelle Leber made a series of Geant 4 simulations of detector backgrounds to help guide detector material selection and design[26]. A series of Germanium detector measurements was done to tune and validate her simulation. There are slight differences between this simulation and the FPD measurement. The simulation used a magnetic field of 3.0 T at the detector while the nominal field setting used in the measurement is 3.3T at the detector. Also the simulation assumed a resolution of 600 eV instead of the measured value of 1.60 ± 0.02 keV (FWHM).

For the background cuts the simulation assumed a 90 percent efficiency for the veto system and used a 100 ns timing window for the multi-pixel cut. The true veto system efficiency is unknown but certainly not the 90 percent as indicated by the high energy ROI results.

The simulation and measured spectra in figure 4.11 track each other very well, similarly for the cut spectra in particular given the set-up differences in the cuts. Instead of the

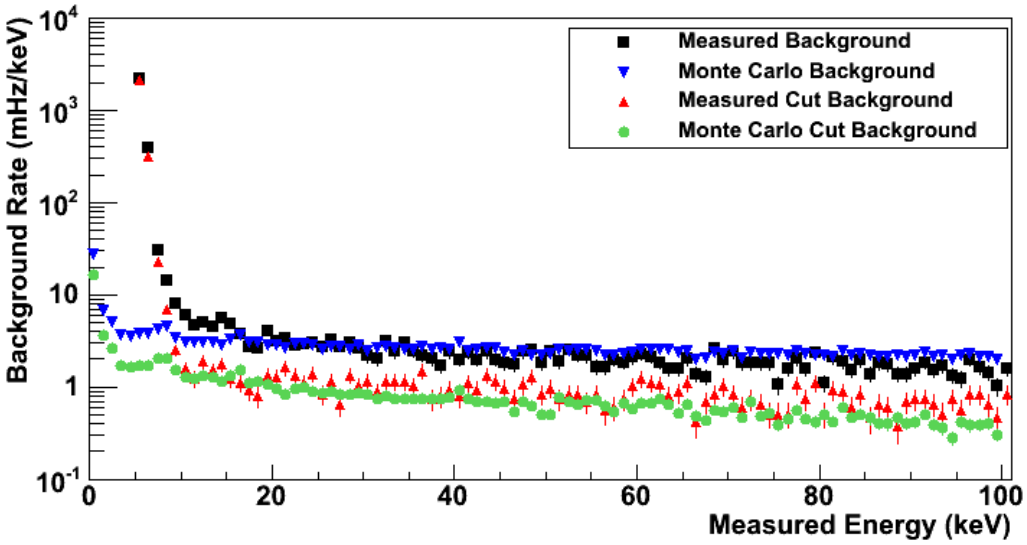

Figure 4.11: Raw simulation (blue) and measured (black) background spectra. Combined cut simulation (green) and measured (red) background spectra. The measured spectra are summed over 127 operating pixels and scaled to 148 pixels.

Table 4.6: Measured and simulation background rate comparison. The measured rates are summed over 127 operating pixels and scaled to 148 pixels.

Background Type	Window (keV)	Measured Rate (mHz/keV)	Simulation Rate (mHz/keV)
Raw	16.1-20.1	2.87 ± 0.17	3.14 ± 0.06
Cut	14.6-20.3	0.95 ± 0.08	1.21 ± 0.04

larger ROI energy window discussed in the previous sections, an optimized ROI was used to determine the rates in table 4.6. The details of the selection of the optimized window are found in section 5.2. The simulation over estimates the background rate by 9% and the cut backgrounds by 27%.

Chapter 5

FIGURE OF DEMERIT

The primary sensitivity of the KATRIN experiment is determined by the source strength and the main spectrometer resolution. A confluence of detector parameters contribute to the uncertainty in the neutrino mass including the detector backgrounds and FPD electron response function. The detector system group developed a figure of demerit, F, to quantify these effects. F, essentially a signal to noise ratio, weights the response function against the total background based upon their influence of the m_ν^2 uncertainty.

5.1 Statistical Uncertainty of the Neutrino Mass

The differential tritium beta decay energy spectrum for non-zero qausi-degenerate neutrino mass (m_ν) near the end-point energy (E_0) is

$$\frac{dN}{dE_e} = 3rt(E_0 - E_e)[(E_0 - E_e)^2 - m_\nu^2]^{1/2} \tag{5.1}$$

where r is the signal rate per eV^3, t is the measurement time, and E_e is the beta energy. Katrin's integrating spectrometer selects an analyzing region between the end-point energy $E_0 - m_\nu$ and the spectrometer retarding potential qU. The total number of signal events in this region is

$$N_s = rt(E_0 - qU)^3[1 - \frac{3}{2}\frac{m_\nu^2}{(E_0 - qU)^2}]. \tag{5.2}$$

Including the background rate b the total number of counts is

$$N = N_s + N_b = rt(E_0 - qU)^3[1 - \frac{3}{2}\frac{m_\nu^2}{(E_0 - qU)^2}] + bt. \tag{5.3}$$

The statistical uncertainty for the neutrino mass (m_ν) is found from differentiating

equation 5.3 with respect to m_ν^2.

$$\sigma_N^2 = N_s + N_b = (\frac{\partial N}{\partial m_\nu^2})^2 \sigma_{m_\nu^2}^2 \tag{5.4}$$

$$\frac{\partial N}{\partial m_\nu^2} = -\frac{3rt}{2}(E_0 - qU) \tag{5.5}$$

$$\sigma_{m_\nu^2} = \frac{2}{3rt(E_0 - qU)}\sqrt{N_s + N_b} \tag{5.6}$$

Neglecting the neutrino mass in N, since the analysis window is much larger than the neutrino mass, yields

$$\sigma_{m_\nu^2} = \frac{2}{3rt}\sqrt{rt(E_0 - qU) + \frac{bt}{(E_0 - qU)^2}}. \tag{5.7}$$

The optimal window size $E_0 - qU$ is found by minimizing equation 5.7 with respect to $E_0 - qU$.

$$\frac{\partial \sigma_{m_\nu^2}}{\partial E_0 - qU} = \frac{\partial}{\partial E_0 - qU}\frac{2}{3rt}\sqrt{rt(E_0 - qU) + \frac{bt}{(E_0 - qU)^2}} = 0. \tag{5.8}$$

The solution is

$$(E_0 - qU) = (\frac{2b}{r})^{1/3} \tag{5.9}$$

After substituting the optimum window into equation 5.7, the optimum neutrino mass uncertainty is

$$\sigma_{m_\nu^2} = k\frac{b^{1/6}}{r^{2/3}t^{1/2}} \tag{5.10}$$

where k is a constant $= \left(\frac{16}{27}\right)^{1/6}$[24]. This formula represents the best case scenario because the background and the endpoint energy are assumed to be independently and infinitely accurately determined[31][32].

5.2 Figure of Demerit

There are two contributing factors from the detector system that affect the uncertainty in equation 5.10; the detector background rate b_{det} and the detector response d. The detector response d in figure 5.1 is the normalized distribution function for tritium end-point energy

electrons incident on the focal plane detector. The main spectrometer potentials qU are set very near the tritium end point energy. These eV to sub-eV window sizes $(E_0 - qU)$ are much smaller than the keV level detector resolution in the response function d. Therefore any main-spectrometer signals and backgrounds can effectively be considered as a delta function that are distributed across a large energy range when folded with the detector response d.

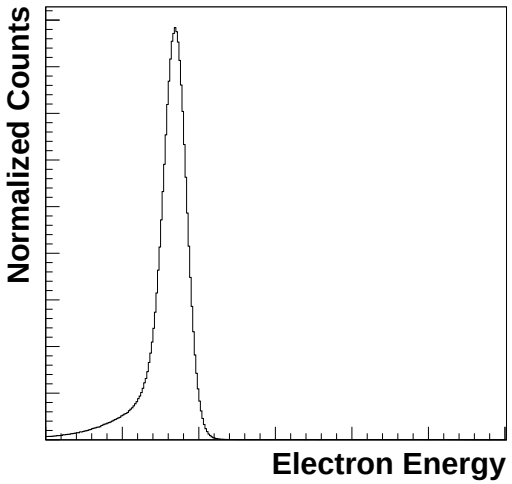

Figure 5.1: An example of a normalized detector response function d.

The total background rate b has two constituent parts: main spectrometer background b_{ms} and detector background b_{det} rates. Main spectrometer backgrounds are fixed by the analysis window $E_0 - qU$, are independent of the detector system, and assumed here to be constant. Based upon previous experience with the Mainz Experiment the KATRIN design goal for the spectrometer related background rate is $\leq$10mHz[24]. Inserting the two background components into 5.10 results in

$$\sigma(m_\nu^2) = k\frac{(b_{ms} + b_{det})^{1/6}}{r^{2/3}t^{1/2}} \tag{5.11}$$

Since the entire energy regime cannot be analyzed due to experimental limitations, an

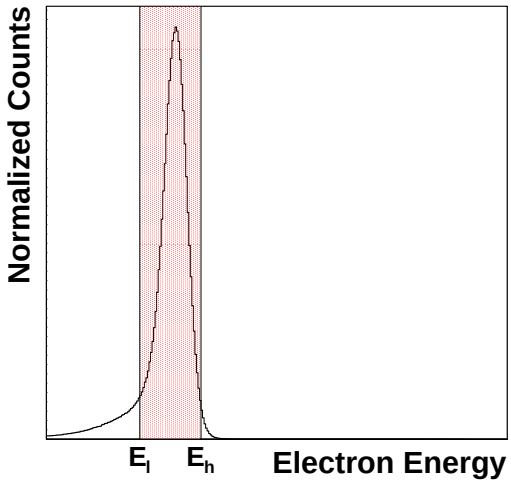

Figure 5.2: An example of a normalized detector response function d with a shaded region of interest from E_l to E_h. Integration of the response function in the shaded region results in the scaling factor $f(E_l, E_h)$.

analysis region of interest is selected. The region of interest spans from E_l to E_h and has a width ΔE. The total number of events (both signal r and background b_{ms}) is reduced because of this selection. This is taken into account in equation 5.11 by introducing a scaling factor f, which is the integrated detector response over the region of interest.

$$f(E_l, E_h) = \int_{E_l}^{E_h} d \, \mathrm{d}E \tag{5.12}$$

The scaling factor $f(E_l, E_h)$ is equivalent to the area under the curve in the shaded region of figure 5.2. Similarly the detector background rate b_{det} is now the integrated detector background spectrum in the region of interest as in figure 5.3. Scaling r and b_{ms} in equation 5.11 leads to a m_ν^2 uncertainty of

$$\sigma(m_\nu^2) = k \frac{(f(E_l, E_h) * b_{ms} + b_{det})^{1/6}}{(f(E_l, E_h) * r)^{2/3} t^{1/2}}. \tag{5.13}$$

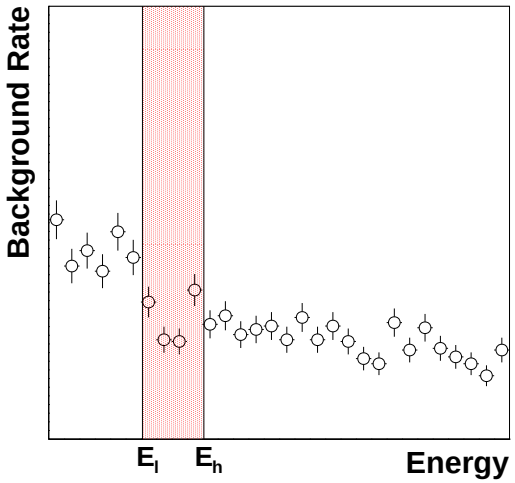

Figure 5.3: An example of a detector background spectrum with a shaded region of interest from E_l to E_h. Integration of the spectrum in the shaded region results in the detector background rate b_{det}.

Separation of the detector contributions from equation 5.13 results in

$$\sigma(m_\nu^2) = k\frac{b_{ms}^{1/6}}{r^{2/3}t^{1/2}}\frac{(f(E_l,E_h)+\frac{b_{det}(E_l,E_h)}{b_{ms}})^{1/6}}{f(E_l,E_h)^{2/3}}. \tag{5.14}$$

The figure of demerit, F, is defined as

$$F = \frac{(f(E_l,E_h)+\frac{b_{det}(E_l,E_h)}{b_{ms}})^{1/6}}{f(E_l,E_h)^{2/3}}. \tag{5.15}$$

F is a figure of demerit since the lower the value the smaller the effect that the detector system contributes to the final neutrino mass uncertainty. For any given electron response function and background spectrum there is an optimal region of interest that minimizes F. There is a balancing act created by F between the accepted signal rate and the accepted background rate. Figure 5.4 illustrates as the region of interest width, ΔE, increases so do the contributing backgrounds. Decreasing the width ΔE limits the number of accepted electrons in the response function. The detector system commissioning goal is $F < 1.2$, and

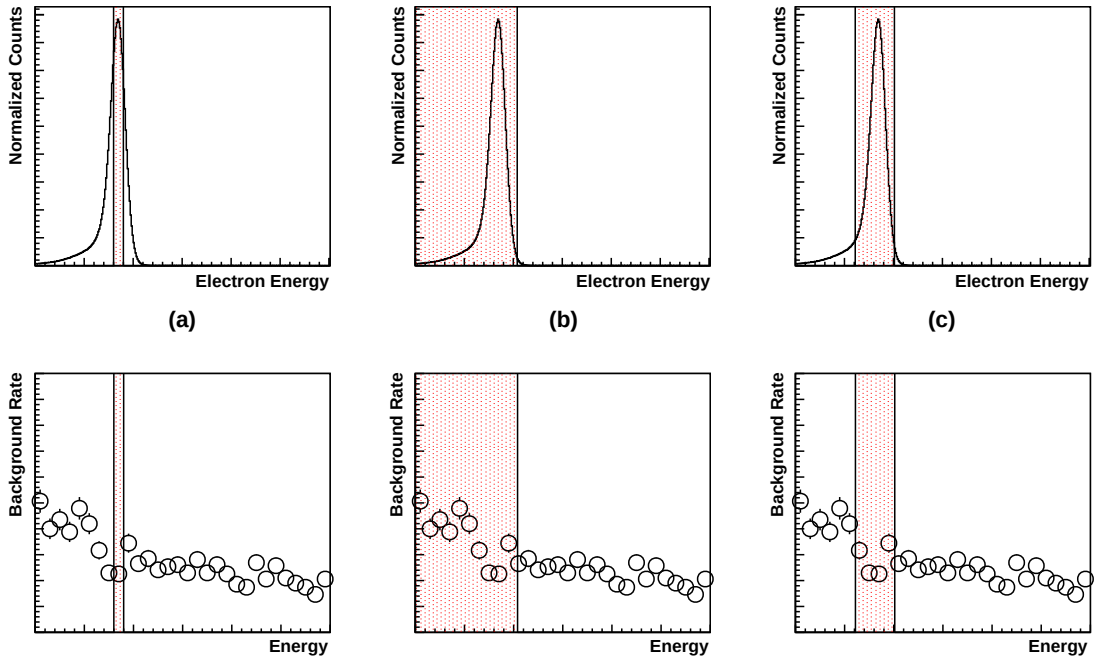

Figure 5.4: The upper plots are normalized electron response functions d while the lower plots are detector background spectra, where the shaded regions represent different possible region of interest widths ΔE. (a) For a small region of interest width ΔE the number of allowed electrons is small resulting in a large F. (b) A large region of interest width ΔE accepts a large background rate resulting in a large F. (c) An optimized region of interest width ΔE balances the accepted electrons against the backgrounds resulting in a minimized figure of demerit F.

is set by the needs of main spectrometer commissioning. The penultimate goal is $F < 1.1$ for tritium data taking[33].

5.3 Measurement and Results

Two approaches were considered to evaluate the figure of demerit: a pixel by pixel approach and a holistic approach. The pixel by pixel approach treats each pixel as an individual detector and a figure of demerit would have to be derived for each. This method gives an accurate evaluation of each pixel but requires much more data taking time to obtain accurate background spectra for each pixel. Since expediency was of great concern during

detector commissioning the holistic approach was opted for. In the holistic approach the data from all the pixels in the focal plane detector are summed together and then evaluated.

The measurements for the figure of demerit should be taken with the same settings as expected for tritium running. Thus all data were taken at the nominal magnetic field settings of 3.6T on the detector magnet and 6T on the pinch magnet. These are the expected field settings for the experiment, but some future optimization may occur depending upon final system configuration.

Only 127 pixels of the 148 detector pixels were used for this analysis, since valid energy calibration data from Americium 241 source runs were required for each pixel. Of the 21 removed pixels 15 had missing calibrations due to broken or poorly functioning electronic channels. The remaining six channels had poor calibration fits due to Compton scattering electrons contaminating the Americium spectrum as discussed in section 2.4.5.1.

The electron response function was extracted from electron source calibration data(section 2.4.5.2). Data for the 127 active pixels were normalized and then averaged together to provide the global response function. The electron-source energy was set to the tritium endpoint energy of 18.6 keV. Even though the main spectrometer produces a spread due to the difference in the potential setting U and the end-point energy E_0; the difference $E_0 - qU$ is much smaller than the detector system energy resolution. Hence the detector response is extracted from a single electron gun setting because as seen in figure 3.15 the energy resolution changes very little between 18 and 19 keV.

Detector background spectra were averaged over 8 hours of run time and figure of demerits were calculated for both raw and cut background spectra. The cut background spectra result from implementing both the veto cut and multi-pixel cut. These cuts are explained in section 4.2.

The minimum figure of demerit at nominal magnet field settings is 1.224 ± 0.007 for the raw background spectrum and 1.119 ± 0.006 for the cut background spectrum (Figure 5.5). The result from the cut background spectrum also has a larger region of interest ΔE due to the lower backgrounds. This result meets our commissioning goal of $F < 1.2$. In fact, the cut background spectrum nearly meets the tritium data taking goal of $F < 1.1$.

As discussed in section 2.4.2, the KATRIN detector system is equipped with a post-

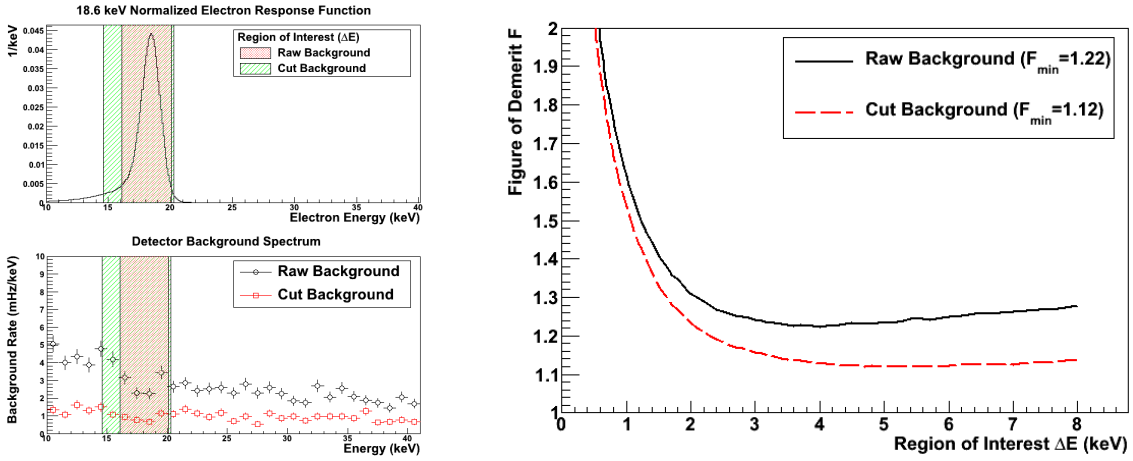

(a) (b)

Figure 5.5: (a)Above is the normalized electron response function taken with an electron gun setting of 18.6 keV. Below are the raw and cut detector background spectra. The shaded areas represent the two optimized regions of interest for each background. (b)Figure of demerit minimization curves.

Table 5.1: Figure of demerit results for raw and cut background data at nominal magnetic field settings.

Background	ROI (keV)	ΔE (keV)	F_{min}	Background Rate (mHz/keV)
Raw	16.1-20.1	4	1.224 ± 0.007	2.87 ± 0.17
Cut	14.6-20.3	5.7	1.119 ± 0.006	0.95 ± 0.08

acceleration electrode (PAE) that can boost electrons into a lower background region. PAE settings of 7.7, 10, 12 kilovolts were used to examine three background regions. However, low energy electrons emitted from the main-spectrometer blank-off flange contaminated the background spectra as discussed in section 4.3. These background electrons should not be generated in the final KATRIN setup, as the flange will be replaced by the main-spectrometer volume.

The resulting figure of demerits from these setups are higher than the 0 kV setting because of the higher than expected electron backgrounds contamination. Using the 0kV background with the post-accelerated detector response gives an indication of the expected

Table 5.2: Figure of demerit results with post acceleration using the cut background at nominal magnetic field settings.

PAE (kV)	ROI (keV)	ROI width (keV)	F_{min}	Background Rate (mHz/keV)
12	28-32.2	4.2	1.137 ± 0.006	1.27 ± 0.11
10	25.6-31.3	4.7	1.156 ± 0.006	1.63 ± 0.11
7.7	23.7-28	4.3	1.141 ± 0.007	1.30 ± 0.12

Table 5.3: Figure of demerit results using post-accelerated response functions and non post-accelerated cut background to calculate F to better represent the expected final KATRIN setup.

PAE (kV)	ROI (keV)	ROI width (keV)	F_{min}	Background Rate (mHz/keV)
12	28-32.2	4.2	1.111 ± 0.006	0.86 ± 0.08
10	25.3-30.3	5.0	1.113 ± 0.006	0.89 ± 0.08
7.7	23.5-28	4.5	1.112 ± 0.006	0.85 ± 0.09

background from the main-spectrometer. Table 5.3 shows that independent of the PAE value the figure of demerit reaches a minimum of $F_{min} = 1.11$.

Chapter 6

IN-SITU DETECTOR DEAD-LAYER MEASUREMENT

6.1 PIN-Diode Dead Layer

KATRIN's neutrino mass sensitivity is primarily dependent upon the precision of main spectrometer and the strength of the source, but modeling and understanding the detector response is required, since it also influences KATRIN's sensitivity. A critical parameter that effects the detector response is the focal plane detector's dead layer. The dead layer is a surface layer of the semiconductor detector where uncollected energy deposition occurs influencing the detector response function.

As discussed in chapter 3, ionizing radiation interacting in the detector creates electron-hole pairs proportional to the energy deposition of the radiation. Charged particles, unlike gammas, do this in a continuous way as they move through the detector. The doping layer of the detector forms a junction with the intrinsic layer that is outside the depletion region. Partial or zero charge collection occurs in this region because the generated electron-hole pairs can recombine rather than drift to a contact due to the low or zero electric field.

For a monoenergetic particle of energy E interacting in the detector, an ideal detector without a dead layer has a response function shown in figure 6.1 with an idealized delta-function at an energy E and a separated, broad, small-amplitude backscatter distribution from electrons escaping the detector. Adding a 1500 Å dead layer causes an initial energy loss (Figure 6.2) of the incident electrons that creates an asymmetric energy spectrum that fills the space between between the peak energy value and backscatter tail. The counts in the peak are reduced by a factor of 100. In order for KATRIN to reach its sensitivity goals, it is desirable to be able to measure the thickness of the dead layer to 10 nm accuracy. Its influence on the focal plane detector energy response is necessary for generating accurate simulations of the KATRIN experiment. Furthermore, the amount of energy loss in the dead layer is both angle and energy dependent and hence modifies the spectrum of electrons from

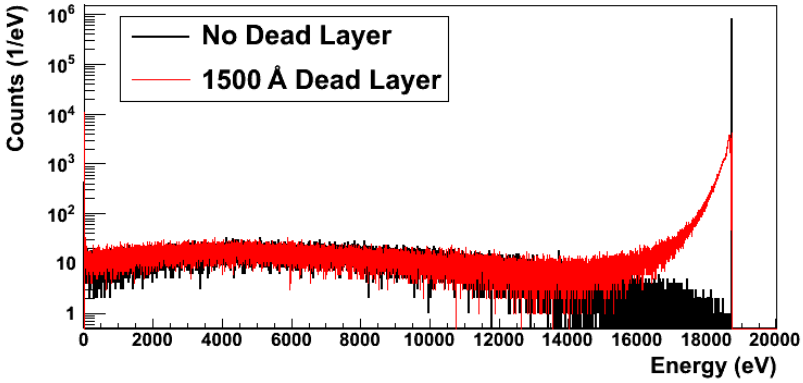

Figure 6.1: Simulated energy deposition spectra in a silicon detector for 18.6 keV normal incident electrons with no dead layer (black) and a 1500 Å monolithic dead layer (red). Spectra simulated with KESS software package[34].

tritium in complex ways.

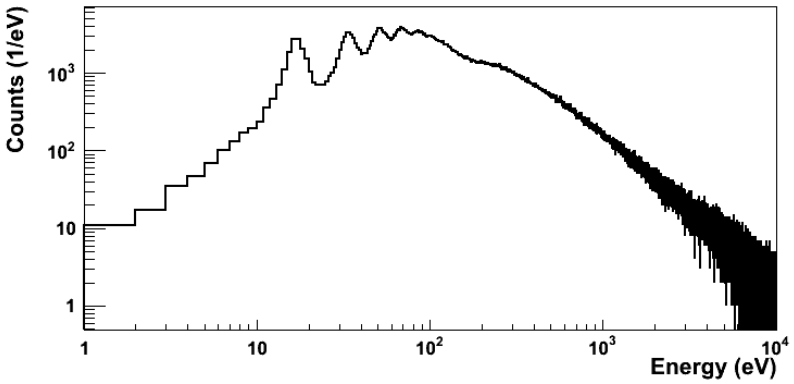

Figure 6.2: Simulated electron energy deposition in a 1500 Å silicon dead layer for 18.6 keV electrons. Spectrum simulated with KESS software package[34].

The typical measurement method to determine PIN-diode dead layers is to measure alpha particle energy deposition for different incident angles [28]. Increasing the angle increases the path length of the alpha through the dead layer resulting in greater energy

loss. The energy deposited in the detector is then determined from the equation

$$E_{deposited} = E_0 - (\frac{1}{\cos\theta} - 1)\frac{dE}{dx}T \tag{6.1}$$

where E_0 is the intercept value, $\frac{dE}{dx}$ is the average energy loss usually determined by the Bethe-Bloch function, and T is the thickness of the dead-layer. This method requires an alpha source with the ability to vary its angle or the angle of the detector under test. Neither of these options are workable in the KATRIN detector system. Nor, as we shall report, does this technique necessarily lead to an accurate description of the dead layer. A method can be constructed using a variable energy electron source but still relying on a continuous approximation for electron energy deposition. Such a model does not properly approximate electron energy loss because the energy loss does not obey a distribution where the average energy loss is the same as the most probable loss, but rather the one seen in figure 6.2 [34]. An accurate method requires the entirety of the electron energy spectrum to be compared with a detailed monte Carlo simulation to determine the focal plane detector dead-layer thickness.

6.2 Dead-Layer Measurement Methodology

The general method to determine a dead-layer thickness is to use the entire shape of the electron spectrum generated by a mono-energetic electron source and compare it with simulated spectra using different dead-layer thickness. The simulated spectra for an assumed dead-layer value are fit to the electron source energy spectra calculated using a χ^2 minimization technique. A series of calculations are performed as the dead layer is varied. Then a quadratic fit to the values of dead-layer thickness versus χ^2 is made and a minimum χ^2_m is found. At the minimum χ^2_m of the curve is the best-fit value for the dead-layer thickness. The error on the thickness is the difference between the best-fit thickness and the thickness found at $\chi^2_m + 1$; marginalizing over other fit parameters.

A multitude of electron energy settings can be used to increase the data set and constrain the fit. Since the dead-layer thickness is independent of electron energy, the χ^2 can be summed from fits at multiple energy settings for a single dead-layer value. The fit region

for the minimization at each incident energy is found by finding the first energy bin around the peak value bin that has a minimum of 10 counts. This maximizes the size of the fit window for each spectrum and avoids χ^2 minimization's problem due to low statistics.

The relative amplitude of the simulated spectrum and the electron source spectrum are scaled. The scaling of the two histograms together can either be done by letting the normalization float as a parameter of the χ^2 fit or can be set by the ratio of the integrated counts in the electron source to the simulation spectrum. The former method has the problem of underestimating the normalization but does produce smaller χ^2 values. The latter method is used, since it is just as reasonable as the former, and neither method affects the final dead-layer result in a measurable way.

6.2.1 Electron Monte Carlo Generation

The Katrin Electron Simulation Software (KESS) package, constructed by Pascal Renschler, Hans Bischel and Zine-El-Abidine Chaoui simulates detailed interactions of electrons incident on a silicon wafer[34]. The simulation described here used a simple setup of monoenergetic electrons incident normally on a silicon wafer. In the 500 micron wafer an active detector region and dead-layer region were specified. The dead layer to active region transition assumes that the dead layer is monolithic and the regions sharply transition from one to the other. The same Monte Carlo simulation was used for all pixels in the focal plane detector. Simulated spectra were generated for dead layers of thicknesses from 100 Å to 5000 Å in 100 Å increments for monoenergetic electrons at energies corresponding to the electron source voltage data set.

The focal plane detector sits in a magnetic field at the nominal setting of 3.6 T on the detector magnet and 6 T on the pinch magnet. The major effect of the magnetic field is that electrons are confined to the magnetic field lines. Backscattered electrons following the magnetic field lines have their momentum reversed by the electrostatic potential and return to the focal plane detector. The transit time of backscattered electrons is very fast compared to the charge collection time of the detector. Instead of simulating the magnetic and electric field configuration of the detector system the backscattered electrons' momenta

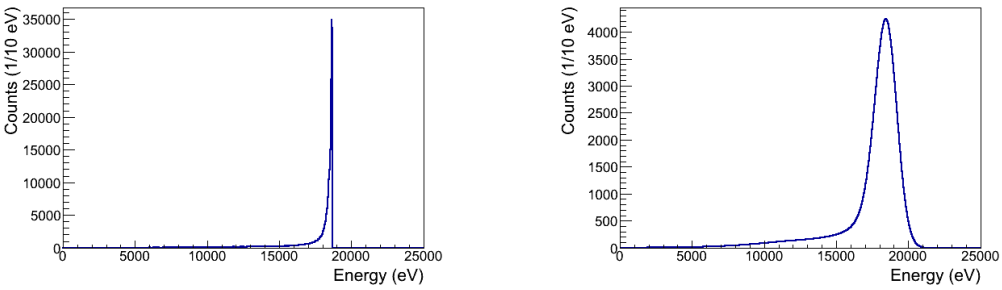

(a) (b)

Figure 6.3: (a) Simulated 18.6 keV electron energy spectrum with a magnetic field on in a PIN diode with 1500 Å dead layer. (b) The simulated spectrum convolved with a Gaussian to include the electronic noise and a Fano noise Gaussian.

are negated and returned immediately.

The simulated focal plane detector spectrum in figure 6.3a has perfect electronic resolution. Both the electronic resolution and statistical Fano noise need to be folded into the spectrum. Each pixel has a different level of electronic noise, so the simulated spectrum is convolved with each pixel's Gaussian noise function. The width of the noise function is extracted from the width of pulser peaks determined from the electronic pulser calibrations performed for each pixel. The uncertainty (σ_E) in the energy caused by the Fano noise is

$$\sigma_E = \sqrt{E * F * \epsilon} \tag{6.2}$$

where E is the energy deposition, F=.143 is the Fano factor, and $\epsilon = 3.62$ is the ionization energy[28]. After the two convolutions the figure 6.3a is transformed into figure 6.3b.

6.2.2 Electron Source Data Generation

Electron source data were generated at 11 different voltage settings from 9.6 to 19.6 kV in 1 kV increments. The data for 9.6, 10.6 and 11.6 kV were not used in the fits because the low energy ends of their spectra were cut off by the electronics hardware threshold setting. Energy scans were done both at the nominal magnetic field setting of 3.6 T on the detector

magnet and 6 T on the pinch magnet as well as for zero field.

An Americium 241 source provides the energy calibration spectrum for focal plane detector data. It has two relatively isolated gamma calibration peaks at 26.3448 keV and 59.5412 keV. Each peak is fitted with a Gaussian and the mean ADC value is extracted. The energy calibration is determined from a linear fit (ax+b) of the mean values versus the energy values, where the slope (a) is in units of energy per ADC channel x and the offset b is in the units of energy. The error on the resultant slope is less than 0.1 percent. The error in the offset is on the same order as the generated offset itself, typically around 150 eV.

The electrons generated from the electron source at zero magnetic field are not well imaged on the focal plane detector. There is no magnetic field to constrain the trajectories of the electrons and the electric field lines from the source disc are not solely restricted to the focal plane detector but illuminate the entirety of the vacuum chamber. A study of the electric fields and electron trajectories by T.J. Corona, found that only a 2 cm diameter circle of the source disc is imaged onto the focal plane detector. This greatly reduces the rate seen on the focal plane detector as compared to data taken with the magnetic field on. Furthermore, the electrons generated from the remainder of the disc scatter inside the vacuum chamber. This creates a hard-to-quantify background and a preference for the better constrained magnetic-field-on data.

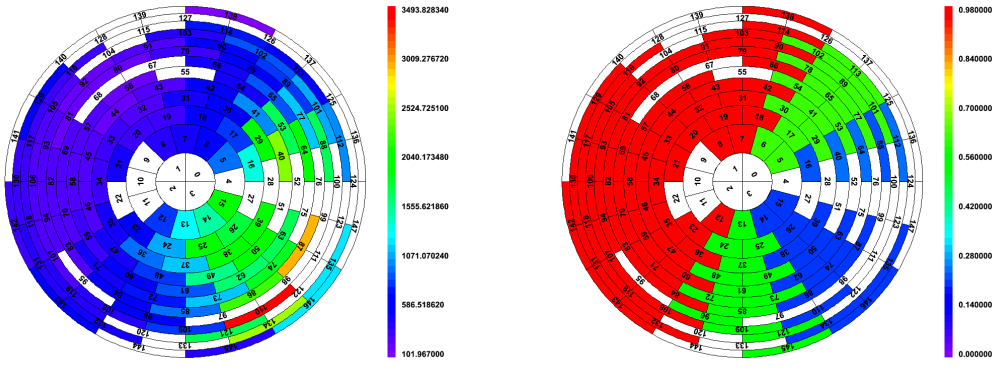

(a) (b)

Figure 6.4: Focal plane detector (a) scaler rates and (b)proportional live time. The proportional live time is the ratio of the scaler rate to the recorded data rate.

At the nominal magnetic field setting, the election gun source disk images onto the focal plane detector. However, the illumination system shines on the source disk at a rather large oblique angle causing a significant UV-light intensity variation across the disk. Hence, the rate varies a full order of magnitude from one side of the detector to the other (Figure 6.4a) and several outer pixels are not illuminated. Large rates create two problems, the first being a live-time issue and the second being a baseline shift.

Half of the focal plane detector was operating at less than 100 percent live time created by large rates. There are 4 separate slices of pixels each suffering a different proportion of dead time, each associated with a different FLT card. Since the dead time proportion is the same for each slice this is a form of non-paralyzable dead time.

The other problem large rates create is a negative baseline shift of the signal pulses. This is caused by the ac coupling in the system and the trapezoidal filter parameters used by the FLT firmware for extracting the energy of the waveform [35]. During high-rate data taking the typical interval between events causes an event pulse to start on the tail of the previous pulse. As a consequence the early-time averaging window (the window that reaches the peak of the event pulse first) in the trapezoidal filter sums too little charge, while the late-time window (the window at the start of the event) averages too much charge. The difference of the two sums creates the negative offset. Figure 6.5 represents peak position of 18.6 keV electron data taken at different event rates on a single pixel. It shows that the base line shift manifests itself as a negative energy offset, reducing the observed peak position. This offset is not significant and can be ignored for the americium energy calibration as the rates for this calibration are on an order of a few hertz per channel. Typically this problem is solved in the electronics chain with a form of baseline restoration or using a bi-polar shaping filter[28]. Neither of these were implemented at the time of data taking but baseline restoration is being implemented now.

The negative offset created by the base-line shift does create a problem for this analysis since the energy calibration is modified from ax+b to ax+b+c(r) where c(r) is a rate dependent offset parameter. The electron source data is calibrated with only the americium calibration, without a correction for the rate dependent offset. A problem arises from the fact that simulation data also does not account for the issue and there will be an energy

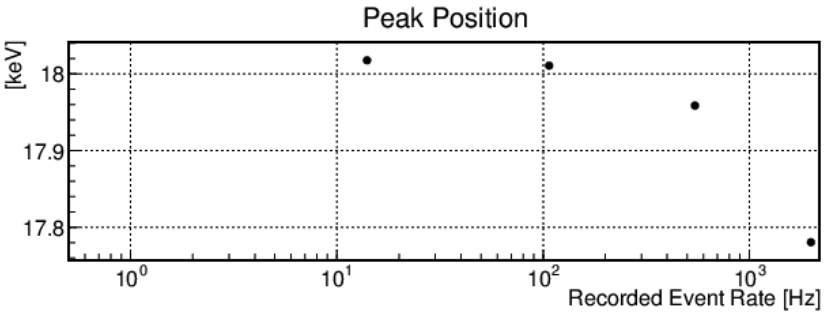

Figure 6.5: Measurement of 18.6 keV electron peak position for a single focal plane detector pixel as a function of rate[35].

offset between the two spectra.

The dead-layer analysis accounts for this systematic by adding an additional floating offset to the fit of the two spectra. The offset adds or subtracts a constant energy from each bin in the simulated data. Figure 6.6 shows the expected strong negative correlation ($\rho = -.88$) between the offset parameter and pixel scaler rate. Results of a linear fit show that the offset declines at $-232.5 \pm .4$ eV per kHz. This scaling factor is similar to the -210 eV per kHz estimated from figure 6.5.

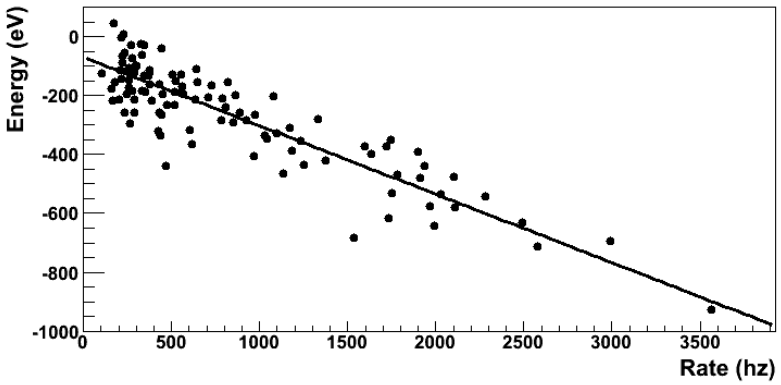

Figure 6.6: Correlation plot between floating offset parameter and scaler rate for each focal plane detector pixel. The two parameters have a strong negative correlation of $\rho = -.88$ and linear fit of the data has a slope of $-232.5 \pm .4$ eV per kHz and intercept of $-69.8 \pm .4$ eV.

Several pixels have been eliminated from the analysis. Table 6.1 details the reason for each pixel that has been excluded. Pixels were eliminated for low rates, poor preamplifier performance, energy calibration problems as discussed previously or just being a dead channel. Background cuts were not applied to the data since the signal rate is so high. On average 103 pixels were used in the analysis. A cut based on using only 100 percent live time channels would leave only 53 pixels.

Table 6.1: Pixels removed from the analysis.

Reason Removed	Pixels
Cross Talk Preamplifier	4, 28, 52, 76, 100, 124
Low Rate	120,125,126,128,133,136,137,139,140,141,144
Dead Electronics Channel	27,51,55,67,68,75,95,97,98,99,111,115,122,123,125,127,147
Bad energy calibration	0,1,2,3,9,10,11,22

6.3 Dead-Layer Measurement and Results

6.3.1 Dead-Layer Diffusion

The initial attempt of evaluating the dead-layer thickness for nominal magnetic field electron data led to confusing results with poor fits. Figure 6.7 shows a broad spread in dead-layer values for the pixels in the focal plane detector. This is inconsistent with the expectation that the focal plane detector's surface doping is a uniform process over the area of the detector. The mean dead-layer thickness for the array was found to be 1239 ± 20 Å ($\chi^2/n.d.f. = 1.48$) with a spread of 216 ± 14 Å. The large spread in thickness across the pixels is much greater than the typical single pixel error of a few angstroms.

Examining the fits and residuals for the best fit thickness indicated lack of agreement between the simulations and data. The simulated spectra do not correctly fit the electron source spectra at the low-energy end of the spectrum. For instance, in the 12.6-keV spectrum in figure 6.8 the simulation undershoots the data from 11 to 8 keV then overshoots the data as it goes to lower energy. This feature shows up in the residual as the steep linear drift in residual values from 7 to 11 keV. The magnitude of this discrepancy decreases with

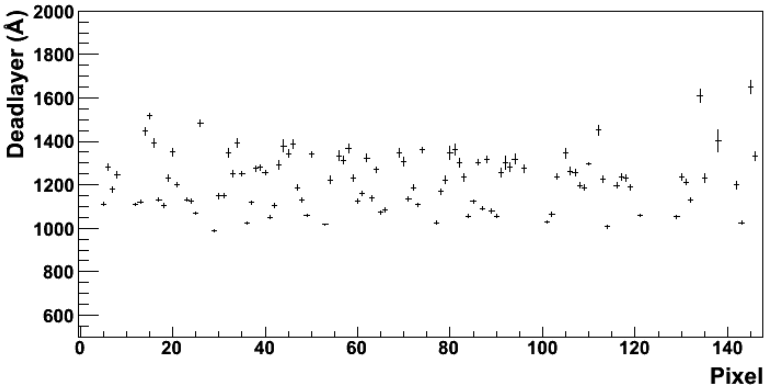

Figure 6.7: Dead-layer thickness results plotted as a function of pixel number for 0 percent diffusion from a monolithic dead layer.

increasing electron source energies seen both in the fits and the residuals.

The simulated spectra appear to have too many counts in the low energy tail. If some of the counts in the tail were moved to higher energies it would increase the data near the under shoot and decrease the data at the overshoot. The solution also needs to account for the increased effect with decreasing electron source energies. Electron backscattering and energy deposition in the dead layer both increase with decreased electron energy. The magnetic field forces backscattered electrons to make multiple transits across the dead layer causing even more energy loss at lower electron energies. In the simulation, the dead layer is assumed to be completely dead but if some electron-hole pairs can diffuse from the region or some part of the region before recombination and be collected on the electrodes it can account for the discrepancy.

A similar mechanism has been found in germanium detectors. A partially dead layer creates slow rising pulses similar to those in a silicon detector that has not been fully depleted. Alexis Schubert modeled this region by having a completely dead-region and a transition region that increases charge collection as function of depth from the completely dead region[36]. The reason for a partially live dead layer in a PIN diode versus a Germanium detector may be quite different as the germanium dead layers are on order of a millimeter as compared to the hundreds of nanometers for a silicon detector. Also Germa-

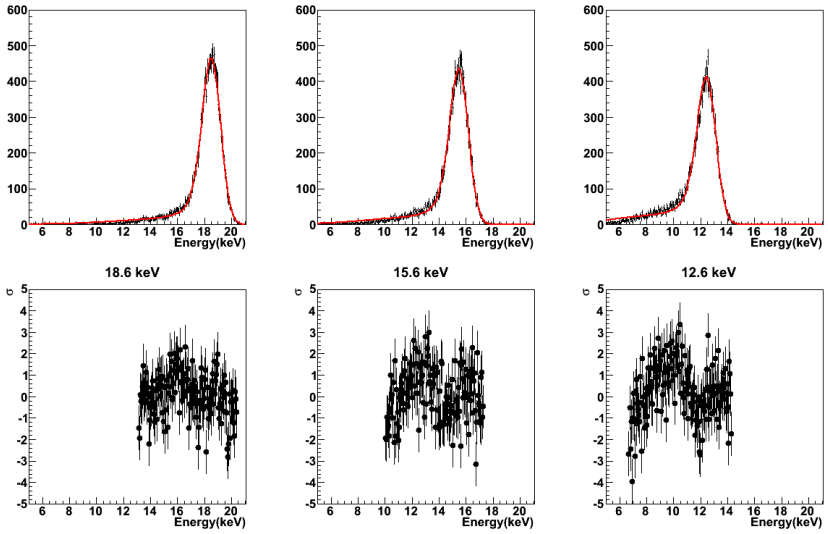

Figure 6.8: (Top row)Pixel 33 electron source data in black fitted with the simulation in red for 18.6 ($\chi^2/n.d.f. = 1.04$), 15.6($\chi^2/n.d.f. = 1.48$) and 12.6($\chi^2/n.d.f. = 2.16$) keV electron source energies. The lower three plots are residuals normalized to the error σ of the electron source data. The residuals only display the points within the fit window.

nium outer contacts are created by lithium drift rather than the ion deposition used for PIN diodes.

Instead of creating a model of depth dependent energy collection in the dead layer, we used a diffusion factor d to describe the amount of energy collected from the dead layer. This is a physically reasonable model because the dead layer is a heavily doped region with no significant field, from which carriers can only escape by diffusion. For every pass an electron makes through the dead layer depositing energy E_{dead} in the dead layer, an amount $d \times E_{dead}$ was added back to the energy collected in the active region. The factor d was allowed to have values between 0 and 1, and varied during the fitting process. Qualitatively, one expects $d \approx .5$ because half the carriers will diffuse to the active region and half will be lost to the contact.

The inclusion of the diffusion factor was found to improve the fit of the simulated spectra to the electron source spectra. The linear trend in the residuals for pixel 33 in figure 6.9 has vanished at low energies with the removal of the over and undershoot in the electron

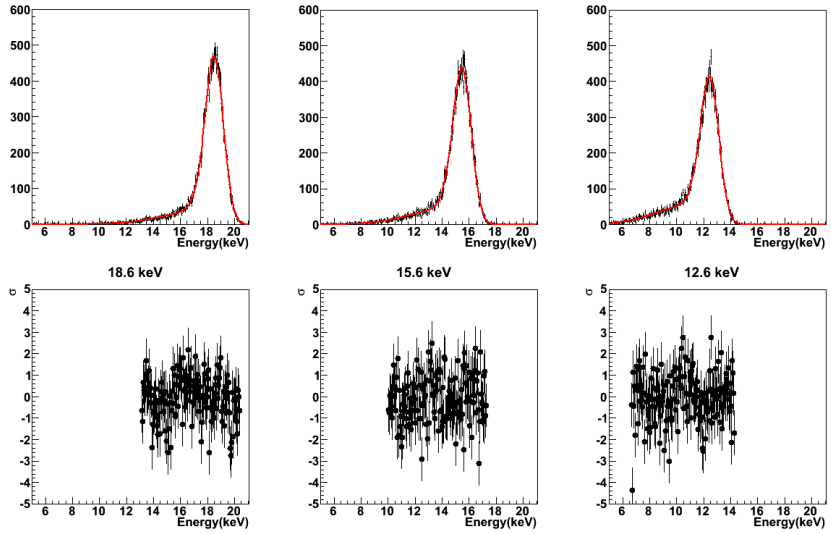

Figure 6.9: (Top row)Pixel 33 electron source data in black fitted with the simulation data including a diffusion factor of .45 in red for 18.6($\chi^2/n.d.f. = .99$), 15.6($\chi^2/n.d.f. = 1.19$) and 12.6 keV($\chi^2/n.d.f. = 1.25$) electron source energies. The lower three plots are residuals normalized to the error σ of the electron source data. The residuals only display the points within the fit window.

source spectra. Inclusion of the diffusion factor in the simulation increases the dead layer as evidenced in figure 6.10 and improves the $\chi^2/n.d.f.$ most dramatically for the lowest energy from 2.16 to 1.25. The mean dead layer increases with increasing diffusion factor seen in both the pixel and histogram plots, while the spread in dead-layer values histogrammed across all pixels reaches a minimum at 40 percent diffusion (Dead layer = 1489 ± 7 Å, sigma = 65 ± 5 Å).

The minimal spread in dead-layer values does not correspond to the minimal χ^2 fit value. Using only the 100 percent live-time pixels to avoid any systematic problems caused by pixels suffering from large dead-times the χ^2 minimum occurs at $45.9 \pm .1$ percent ($\chi^2/n.d.f. = 1.15$). The results for a diffusion factor of 46 percent are displayed in figure 6.11 with a mean dead layer of 1598 ± 7 Å and a width of 160 ± 10 Å. The dispersion of the pixel values is much larger than the typical pixel statistical error of 12 Å.

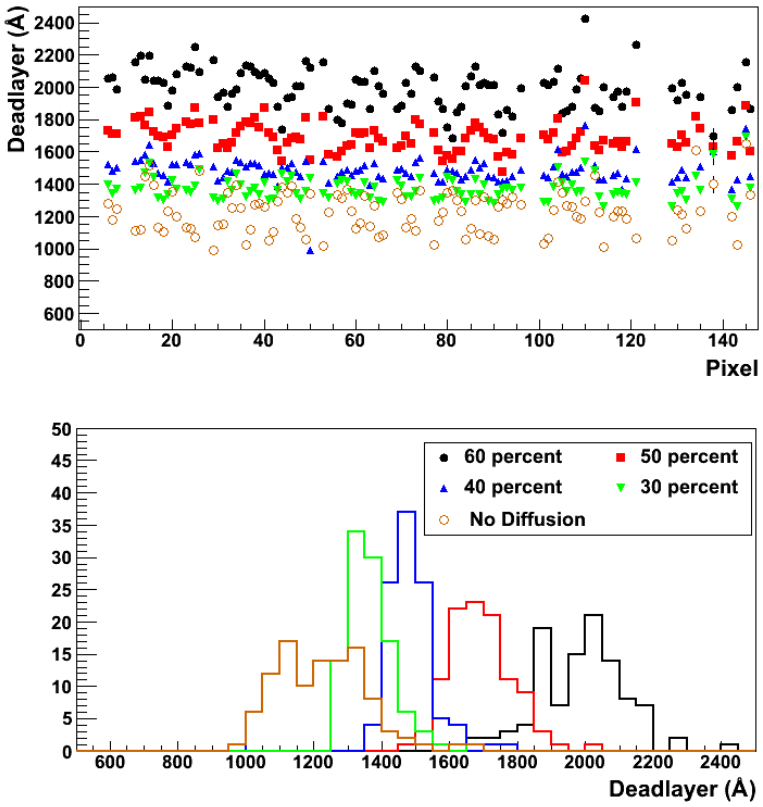

Figure 6.10: Dead-layer thickness results for multiple diffusion percentages.

6.3.2 Geometric and Rate Dependent Effects

The periodic structure seen in figure 6.11 arises from the geometric correlation of pixel number and its polar coordinate. The pixel numbering starts at the center of the detector and spirals outward in rings. There is both an angular (Figure 6.12d) and radial (Figure 6.12f) component to the variation in the dead-layer thickness. The angular modulation in thickness (Figure 6.11) is related to the angular correlation observed in the rates (Figure 6.12c), while the origin of the radial component (Figure 6.12e) is less clear.

The mean variation of the dead-layer thickness at each radius certainly could be correlated with the rate, but similarly it could be associated with the process used to construct the detector. In figure 6.13 the mean dead-layer thickness decreases with the radius. If the surface doping process scans a beam of constant energy at varying angles the implantation

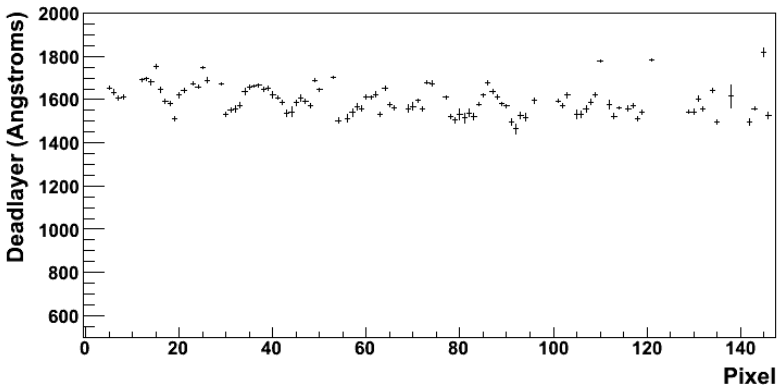

Figure 6.11: dead-layer thickness results plotted against pixel number for 46 percent diffusion.

depth would change radially across the detector.

As stated in section 6.2.2 high-rate data causes a base-line shift that creates an energy offset. Besides an offset the higher rates also degrade the energy resolution (Figure 6.14)[35]. The base-line shift is not constant in time because the electron source is random causing poisson fluctuations of the rate. These fluctuations degrade the energy resolution as the base-line moves up and down around a mean.

The dead-layer determination compares the shape of the electron spectrum and a simulated spectrum at a specific dead layer. The simulated spectrum derives its resolution from a noise measurement made with a pulser. The pulser measurement certainly could have a base-line shift in the data, but it does not fluctuate since the pulser is periodic in time and not random. The width of the pulser peak then is a good measure of the electronics noise at low electron source rates even with a shift in the base-line. But, at higher electron-gun rates, the pulser peak width will underestimate the total noise in the electron source spectrum.

Two new sets of simulated spectra were created to determine how underestimating and overestimating the electronic noise could effect the dead-layer measurement. One set of simulated spectra were created with 10 percent more electronic noise and the other with 10 percent less electronic noise. The results of this study were that if electron source spectra contain more noise than measured with the electronic calibration, the extracted dead-layer

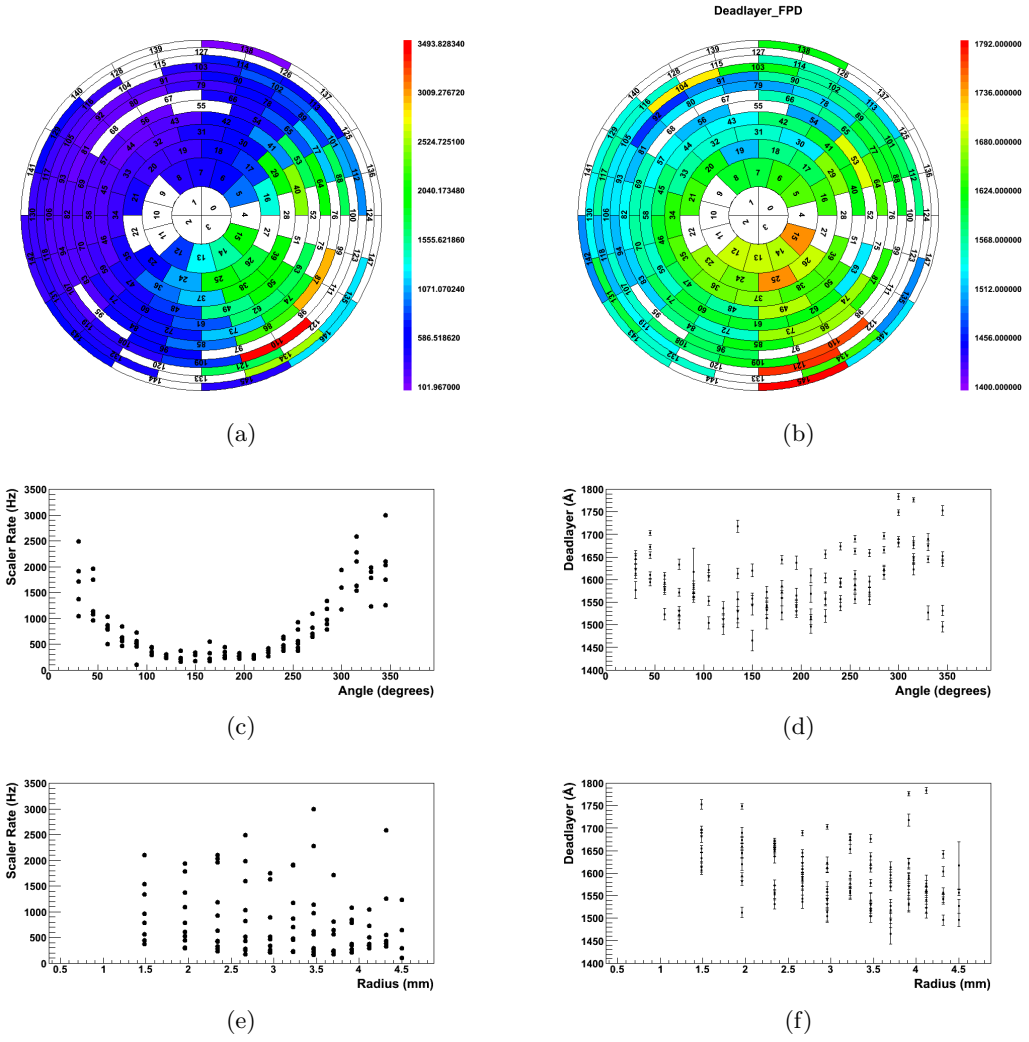

Figure 6.12: Detector scaler rates (hz) plotted (a) on the focal plane detector pixel display, (c) against angular and (e) radial coordinates. Detector dead-layer thickness (Å) with a 46% diffusion factor plotted (b) on the focal plane detector pixel display, (d) against angular and (f) radial coordinates.

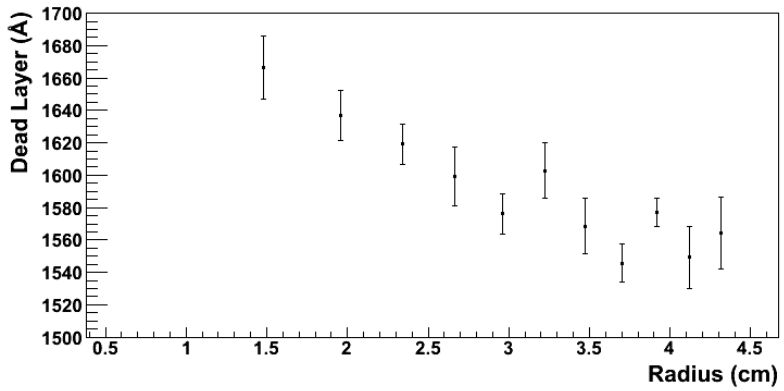

Figure 6.13: Average dead-layer thickness plotted against radius. Each data point is the average of dead-layer values found at the same radius.

value is larger, while if the electron source spectra have less noise, the measured dead-layer values are smaller. This correlation between spectrum width and extracted dead-layer thickness occurs because a thicker dead layer correlates with a broader peak. Since the rate dependence of the width is unaccounted for in the simulated spectra the resulting dead-layer fits have larger thicknesses compensating for the underestimation in electronic noise.

Unable to confidently break the radial dependence of the dead-layer thickness, it will be assumed that the entirety of the thickness variation is rate dependent. The correlation coefficient between the scaler rate and dead-layer thickness is $\rho = .64$. After correcting for

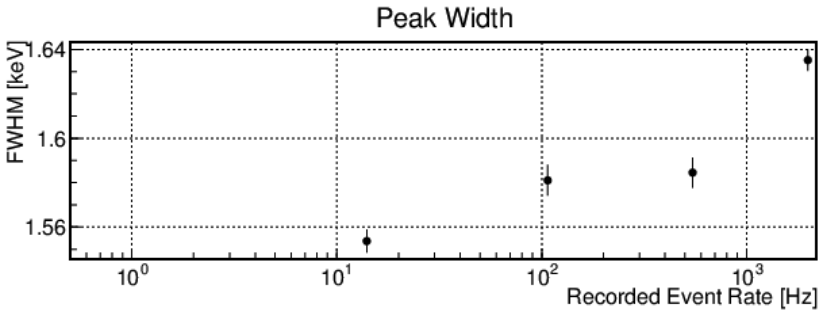

Figure 6.14: Measurement of 18.6 keV electron resolution (FWHM) for a single focal plane detector pixel as a function of rate[35].

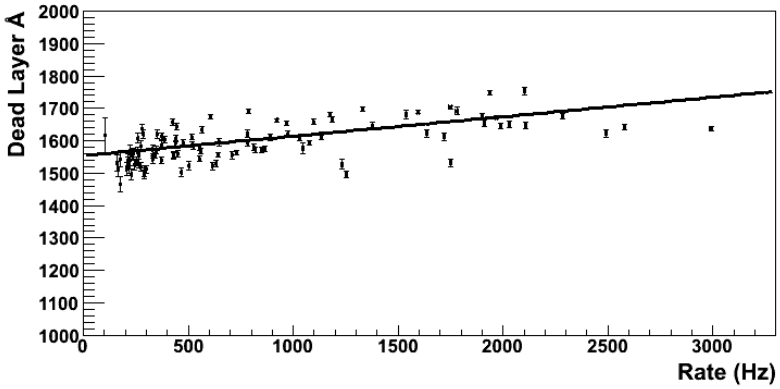

Figure 6.15: Dead-layer thickness rate dependence for a diffusion factor of 46 percent. The correlation factor is $\rho = .64$ a linear fit of the data has slope of $.060 \pm .001 \mathring{A}/hz$ and an intercept of 1554 ± 2 Å.

the rate-based component of the dead layer, the average dead-layer thicknesses is 1554 ± 7 Å. Figure 6.16 is the measured and rate-calculated thicknesses plotted against pixel number.

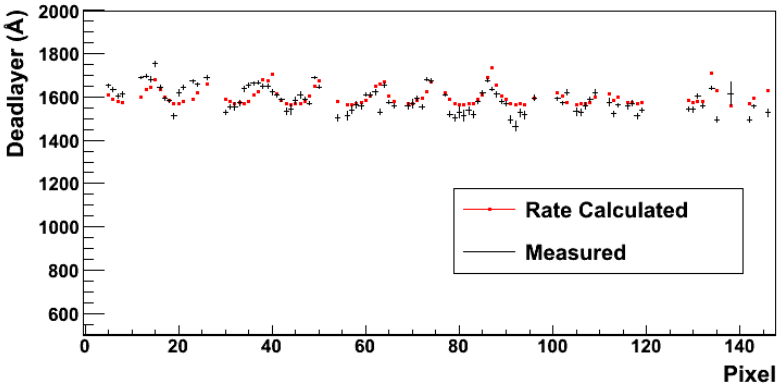

Figure 6.16: Measured dead-layer thickness(black) and calculated dead-layer thickness(red) from the fit in figure 6.15 plotted against pixel number.

In figure 6.15, the spread in data points about the linear fit is much greater than the per point statistical error. The mean statistical error for the array is 12 Å or 0.75 percent for an average dead layer of 1598 Å. On average 20 thousand electron-source events contribute to each pixel's dead-layer fit per energy setting. This results in an expected statistical error

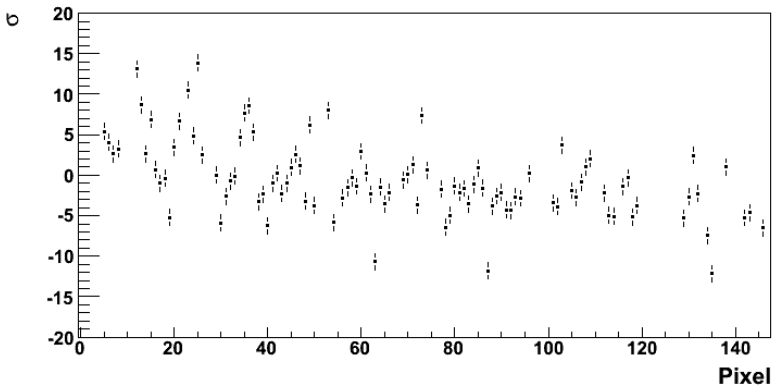

Figure 6.17: Residual between the measured dead-layer thickness and calculated dead-layer thickness from the fit in figure 6.15. Each point has been weighted by the measured error value.

of 0.7 percent per energy fit. The error reduces by a factor of $\sqrt{8}$ to 0.25 percent when including all 8 energy settings. The average statistical error is only a factor of 3 larger than the estimated value; hence, the statistical error per pixel is reasonable.

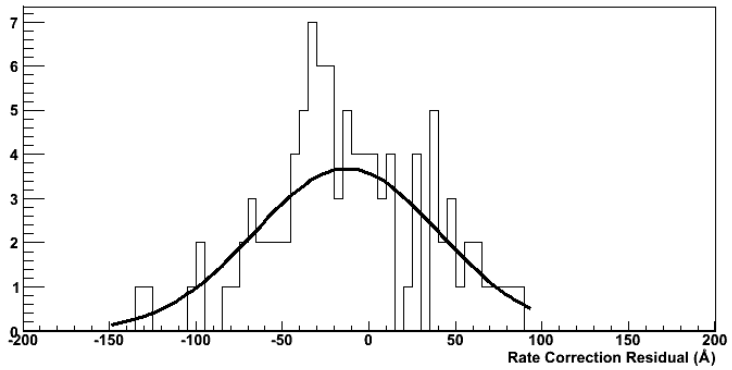

Figure 6.18: The residual of the rate dependence fit in figure 6.15. The dead layer calculated from the rate dependent fit is subtracted from the measured dead layer. The Gaussian fit of the data has a centroid of -12.86 ± 6.99 and sigma of 53.46 ± 8.81 ($\chi^2/n.d.f. = 15.95/34$).

Figure 6.18 is a histogram of the difference between each pixel's dead layer and the best-fit line value in figure 6.15. A Gaussian fit to the histogram results in a centroid of -12.86 ± 6.99 Å and sigma of 53.46 ± 8.81Å ($\chi^2/n.d.f. = 15.95/34$). The sigma of this

distribution is the sample variance about the best-fit line. It represents the error associated with the dead-layer value generated by the best-fit line. The non-zero centroid indicates a slight asymmetry in the sample variance about the best-fit line.

Table 6.2: Rate corrected focal plane detector dead-layer thickness averaged over the focal plane detector pixels. The rate correction is determined from the fit in figure 6.15. The errors listed are the statistical uncertainty of the average, the average systematic error from the rate correction and the remaining systematic errors. The energy calibration, noise, and diffusion errors are added in quadrature to determine the remaining systematic error (Table 6.6). All data in angstroms.

Dead Layer	Statistical Uncertainty	Rate Correction Systematic	Remaining Systematic
1554	7	1	$^{+18.7}_{-12.2}$

6.3.3 Multi-Parameter Fit

Rather than treating a pixel's rate (s_i), radial (r_i) and (θ_i) azimuthal dependence of the dead layer independently, a simultaneous fit also can be performed to determine their effect on the focal plane detector's dead layer. Assuming a dead-layer thickness D_0 and that the previous stated dependencies are first and second order corrections, then a pixel's dead layer, D_i, can be described as:

$$D_i \quad = \quad D_0 + Ar_i^2 + Es_i + B\cos(\theta_i) + C\sin(\theta_i). \tag{6.3}$$

The radial dependent term "A" is only quadratic because the derivative must be zero at the origin. The two angular dependent terms are required to produce an amplitude and phase. Finally, there is the linearly rate dependent term illustrated in figure 6.15.

Table 6.3 shows the results of the linear least-square fit of equation 6.3 to the pixel dead layers. In each row a parameter was added to the fit to demonstrate the improvement each parameter made to χ^2. The rate and radial dependencies gave the greatest improvements to the χ^2 value. Overall this multi-parameter model improves χ^2 by a factor of 1.9 as compared

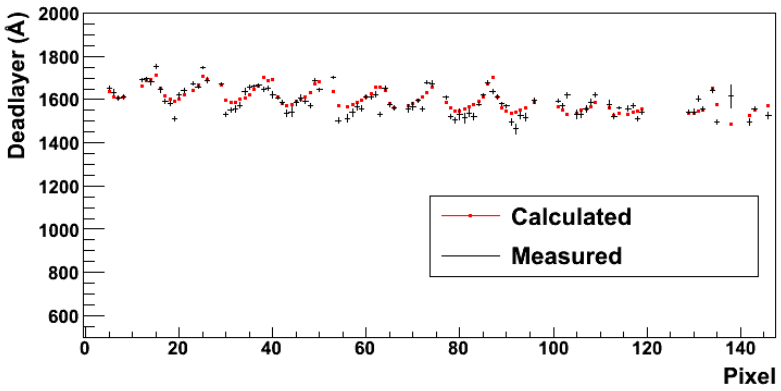

Figure 6.19: Measured dead-layer thickness(black) and calculated dead-layer thickness(red) from the fit of equation 6.3 plotted against pixel number.

Table 6.3: Linear least-square fit parameters from equation 6.3 to the focal plane detector dead-layer pixel data. In each row a fit parameter is added to the minimization.

χ^2	n.d.f.	D_0 (Å)	E (Hz/Å)	A (Å/cm^2)	B (Å)	C (Å)
3913.05	102	1615 ± 1	0 ± 0	0 ± 0	0 ± 0	0 ± 0
2281.63	101	1554 ± 2	0.060 ± 0.001	0 ± 0	0 ± 0	0 ± 0
1535.19	99	1659 ± 2	0 ± 0	$-5.87 \pm .19$	43.78 ± 1.66	-28.94 ± 1.27
1423.35	100	1611 ± 3	0.052 ± 0.002	-5.62 ± 0.19	0 ± 0	0 ± 0
1193.05	98	1609 ± 3	0.052 ± 0.003	-5.60 ± 0.19	-4.30 ± 3.08	-18.28 ± 1.39

to the pure rate-dependent model. The correlation matrix in table 6.4 shows that the radial dependence is independent of the rate and azimuthal fit parameters. As expected the azimuthal and rate dependent components are correlated because of the strong azimuthal dependence of the rate.

Making a rate-dependent dead-layer correction to each pixel's measured dead layer and including the geometric components results in a mean dead layer for the array of 1554 ± 5 Å and sigma of 46 ± 3 Å. The mean dead layer is the average of the measured dead-layer values for each pixel corrected for the count rate. The systematic error associated with the rate correction is ± 2 Å. Unlike the single parameter fit, D_0 no longer represents the corrected dead-layer value. It is reasonable to leave the geometric components because they are potentially artifacts of the deposition process used in the manufacturing of the focal

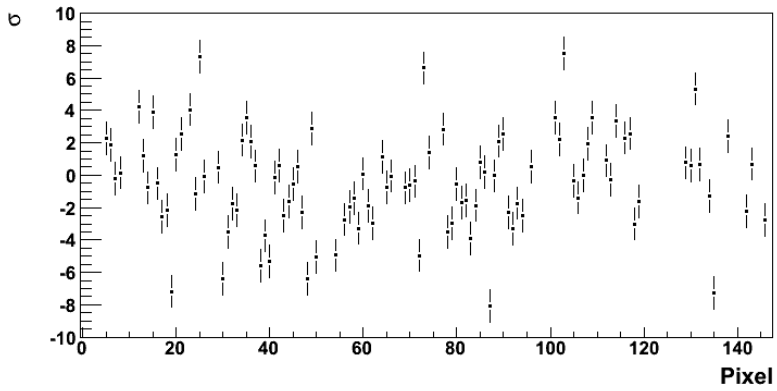

Figure 6.20: Residual between the measured dead-layer thickness and calculated dead-layer thickness from the fit of equation 6.3. Each point has been weighted by each pixel's measured dead-layer error value.

Table 6.4: Correlation matrix for the linear least-square fit parameters from equation 6.3 to the focal plane detector pixels' dead-layer values.

	D_0	A	B	C	E
D_0	1.00	-0.56	0.61	-0.28	-0.81
A	-0.56	1.00	0.03	-0.02	0.08
B	0.61	0.03	1.00	-0.42	-0.84
C	-0.28	-0.02	-0.42	1.00	0.41
E	-0.81	0.08	-0.84	0.41	1.00

plane detector.

Figure 6.21 is the histogram of the multi-variable fit residuals. As discussed at the end of the previous section, this gives the sample variance about the multi-parameter fit. A Gaussian fit to the residual histogram has a centroid of -8.7 ± 5.1 Å and sigma of 38.9 ± 5.4 Å. The variance is still slightly asymmetric about the fit, but the width is smaller as the fit has improved with the change to the multi-paramter model. The width is 3 times larger than the typical pixel's dead-layer thickness error.

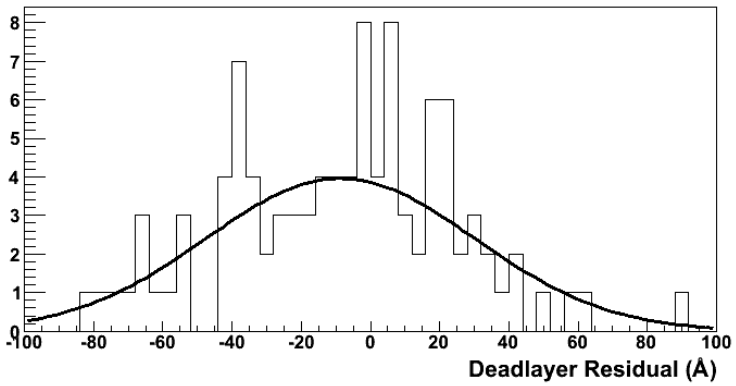

Figure 6.21: The residual of the multi-parameter fit in equation 6.3. The dead layer calculated from the multi-parameter fit is subtracted from the measured dead layer. The Gaussian fit of the data has a centroid of -8.7 ± 5.1 and sigma of 38.8 ± 5.4 ($\chi^2/n.d.f. = 17.19/31$).

Table 6.5: Average focal plane detector dead-layer thickness applying a rate-dependence correction from the multi-parameter fit. The errors listed re the statistical uncertainty of the average, the average systematic error from the rate correction and the remaining systematic errors(Table 6.6). All data in angstroms.

Rate Corrected Dead Layer	Statistical Uncertainty	Rate Correction Systematic	Remaining Systematic
1554	5	2.4	$^{+18.7}_{-12.2}$

6.3.4 Other Systematic Errors

The focal plane detector energy calibration, the electronic noise measurement, and the choice for the diffusion factor are all sources of possible systematic error. The largest source of systematic error is the energy calibration. The floating offset accounts for some of the error in the intercept parameter but not the slope. Increasing the slope by one sigma in the energy calibration increases the dead layer on average by 12.4 Å, while decreasing the slope by one sigma decreases the dead layer on average by 9.5 Å.

The effect of the error in the electronic noise is measured by increasing and decreasing the noise parameter by its error and generating two new sets of simulation spectra. Though

the error on the noise width is Gaussian its effect on the dead layer may not be. Decreasing the width of the noise Gaussian increases the dead layer on average by 7.3 Å and increasing the noise decreases the dead layer by 5.6 Å.

Table 6.6: Focal plane detector dead-layer systematic errors. The energy calibration, noise, and diffusion errors are added in quadrature to determine the remaining systematic total error. All values in angstroms.

Remaining Systematic Error Total	Energy Calibration	Noise	Diffusion
$^{+18.7}_{-12.2}$	$^{+12.4}_{-9.5}$	$^{+7.3}_{-5.6}$	$^{+11.8}_{-5.2}$

In order to estimate the systematic error from the diffusion factor it was varied by one percent about the optimal value. This is ten times the error in the diffusion factor so the difference found between the dead layers at 46 percent and plus or minus 1 percent were scaled accordingly. The resultant error from increasing and decreasing the diffusion factor by 1 sigma is 11.8 Å and -5.2 Å respectively.

6.4 Summary

The method of fitting the electron source spectrum to a simulated spectrum to determine the dead-layer thickness of a PIN diode meets the KATRIN goal of 100 angstrom precision. Before applying a correction, the rate and geometric dependent effects produce a sigma of 65 ± 5 Å in the dead-layer values. Using the multi-parameter fit for the rate dependence and geometric effects, yields the final average detector dead-layer thickness of 1554 ± 5 (Stat.) $^{+18.8}_{-12.4}$ (Syst.) Å.

In the future, the observed rate dependent systematic could be potentially removed from the analysis via several other methods. Both the rate dependence of the base line shift and the broadening it causes could be measured for each pixel in the focal plane detector. It is necessary to use a calibration source random in time as the broadening effect occurs from the poisson variation in the rate. Once the rate based function for the change in resolution

is determined it can be convoluted into the simulated spectra. This was not done for this analysis as the problem revealed itself after the detector system had been disassembled and shipped to Karlsruhe, Germany. Further the solution would also be very computer intensive.

Another method would be to take all of the electron data at low rates where the peak broadening effect is minimal. It does require taking great care in the data taking process. The electron source disc would need to be illuminated at various intensities over multiple runs lengthening data taking time and the single rate data assembled together in a post-data taking analysis process. Limits would also have to be determined on how consistent the rate needs to be from pixel to pixel as well as how low they need to be requiring a study similar to the one proposed in the previous paragraph.

The final method would be adding a rate dependent width as an initial fit parameter to the electron source spectrum. This is not easily implemented to this analysis as in its current state new convoluted spectra would need to be generated for different possible values of the parameter. This is extremely time consuming and computing intensive. A more practical approach may be moving from a binned chi-squared minimization to an un-binned maximum likelihood.

Chapter 7

SUMMARY

Commissioning of the KATRIN detector system at the University of Washington showed that the detector section is near meeting specifications for tritium dating taking. As described in chapter 5, figure of demerit of 1.12 determined from the analysis of cut-background data exceeds the performance requirement for main spectrometer commissioning. Some improvements to the detector system are needed to reach the tritium data taking goal of 1.1.

The figure of demerit in equation 5.15 weights the integrated detector background spectrum against the integrated detector response. Decreasing the width of the detector response increases the signal in the optimal integration window, while decreasing the background allows you to increase the size of the window. The latter is exemplified in the window size differences between the raw and cut background cases.

Since the measurements described here, several upgrades to the system have been implemented to improve the detector response. The FET on the preamplifiers has been upgraded to a unit with better noise properties. The cooling system has been upgraded, increasing the cooling efficiency to the focal plane detector and front-end electronics. Increased cooling improves the noise properties of the front-end electronics and decreases the leakage current of the focal plane detector. Current measurements in Karlsruhe, show a 10 percent decrease in the width of the 60 keV ^{241}Am peak. Measurements are still being completed to determine the current figure of demerit value.

Improvement to the detector related background is reliant on the operation of the post-acceleration electrode. Post-acceleration also improves the detector response. Besides moving the electron peak to a lower background region, it also improves the detector response. Increasing the electron energy decreases the amount of backscattering, thereby decreasing the width of the electron response function.

Backgrounds increased with the use of post-acceleration during detector commissioning at the University of Washington. Peaks appeared in the background spectrum in figure 4.10 are caused by electrons emitted from an upstream blank-off flange. During normal operation the focal plane detector will view the main-spectrometer vacuum instead of the blank-off flange. Background measurements during main spectrometer commissioning are planned to ensure that the electron peaks vanish with the removal of the flange. However, the estimated figure of demerit of 1.11 using the background spectrum without post acceleration and the 12 kV post accelerated response function nearly meets the tritium data taking goal.

Besides detector and electronic related noise, the electron response function is also dependent upon the thickness and stability of the focal plane dead layer. In figure 6.1 the addition of a 1500 Å dead layer changes the mono-energetic electron peak to a broader asymmetric one. The absolute thickness of the dead layer is less relevant than its stability during tritium data taking. An extremely thin dead layer is ideal, but its implementation is limited by detector manufacturing techniques. If the thickness changes during tritium data taking then the optimized region of interest determined by the figure of demerit calculation is invalid and the measured rate will either be too large or small. This creates a difficult systematic to account for in the final analysis of the measured tritium spectrum.

In developing an in-situ method for measuring and monitoring the focal plane detector dead layer, we found that the standard monolithic model used by alpha measurements is not correct. Adding an energy diffusion factor of 46 percent, which adds a proportion of energy deposited in the dead layer back into the active region, significantly improves the fit between simulation and electron data from a $\chi^2/n.d.f.$ of 1.67 to 1.15. The greatest improvement occurs at the lowest electron gun settings because electron backscattering increases at low energies and the presence of the magnetic field returns them to the focal plane detector enhancing the effect.

After including the diffusion factor, a systematic variation still remained in the dead-layer thicknesses. The variance is most likely caused by rate dependent resolution degradation. Correcting for this effect found a focal plane dead layer of 1554 ± 5 (Stat.) $^{+18.8}_{-12.4}$ (Syst.) Å. Though, the dead layer correlates with rate with a Pearson's linear correlation factor of .64, the linear fit used to remove the rate dependence fits the data poorly. Using a multi-

parameter model that also allowed for geometric variation improved the fit quality by a factor of 2.

Returning to the diffusion correction, it does not rely on a particular model for how the energy leaves the dead region. One possible model is that the probability of charge escaping the dead layer and being collected increases linearly from the surface to the end of the dead layer. The expectation for collecting energy from the dead layer is 50% of the energy deposited and close to the 46% found. To reconcile the small discrepancy, a thin completely dead region can be added before the partially dead region. Using the combination of a total and partial dead region, the dead layer would have a completely dead region of $\sim$ 124 Å and partially dead region of $\sim$ 1440 Å.

An alpha measurement of the same dead layer described by the preceding model would measure a value of $\sim$ 839 Å. Alpha measurements of dead layers measure the energy loss in the dead layer and convert it to a thickness using an analytic formula, such as Bethe-Bloch. A partially dead layer would appear thinner than reality due to the extra energy collection. Future measurements using both alphas and electrons are needed to investigate this model.

BIBLIOGRAPHY

[1] F. Rasetti, Physics **15**, 515 (1929). 1

[2] F. L. Wilson, American Journal of Physics **36** (1968). 1, 9

[3] J. Beringer et al., Phys. Rev. D **86** (2012). 4

[4] B. Aharmim et al. and S. N. O. Collaboration, Phys. Rev. C **72** (2005). 4

[5] E. Komatsu, K. M. Smith, J. Dunkley, C. L. Bennett, B. Gold, G. Hinshaw, N. Jarosik, D. Larson, M. R. Nolta, L. Page, et al., Astrophys.J.Suppl. **192** (2011). 5

[6] K. Ichiki, M. Takada, and T. Takahash, Phys. Rev. D **79** (2009). 5

[7] S. A. Thomas, F. B. Abdalla, and O. Lahav, Phys. Rev. Lett. **105**, 031301 (2010). 5

[8] J. Gomez-Cadenas, J. Martn-Albo, M. Mezzetto, F. Monrabal, and M. Sorel, Riv. Nuovo Cim. **35**, 29 (2012). 6

[9] O. Cremonesi, arXiv:1002.1437 [hep-ex] (2010). 7

[10] S. Pascoli, S. T. Petcov, and T. Schwetz, Nucl. Phys. B **734**, 24 (2006). 7

[11] S. Umehara, T. Kishimoto, I. Ogawa, R. Hazama, H. Miyawaki, S. Yoshida, K. Matsuoka, K. Kishimoto, A. Katsuki, H. Sakai, et al., Phys. Rev. C **78** (2008). 7

[12] H. Klapdor-Kleingrothaus, A. Dietz, L. Baudis, G. Heusser, I. Krivosheina, S. Kolb, B. Majorovits, H. Paes, H. Strecker, V. Alexeev, et al., Eur. Phys. J. A **12** (2001). 7

[13] A. Barabash, V. Brudanin, and N. Collaboration, Phys. Atom. Nucl. **74** (2011). 7

[14] E. Andreottia, C. Arnaboldi, F. T. A. III, M. Balata, I. Bandac, M. Barucci, J. W. Beeman, F. Bellini, C. Broerio, A. Bryant, et al., Astropart. Phys. **34** (2011). 7

[15] R. Bernabei, P. Belli, F. Cappella, R. Cerulli, F. Montecchia, A. Incicchitti, D. Prosperi, and C. Dai, Phys. Lett. B **546**, 23 (2002). 7

[16] R. Barate et al. (ALEPH Collaboration), Eur. Phys. J. C **2**, 395 (1998). 8

[17] K. Assamagan, C. Bronnimann, M. Daum, H. Forrer, R. Frosch, et al., Phys. Rev. D **53**, 6065 (1996). 8

[18] V. Aseev, A. Belesev, A. Berlev, E. Geraskin, A. Golubev, N. Likhovid, V. Lobashev, A. Nozik, V. Pantuev, V. Parfenov, et al., Phys. Rev. D **84** (2011). 8, 9

[19] S. C. Curran, J. Angus, and A. L. Cockroft, Physical Review **76**, 853 (1949). 8, 10

[20] C. Kraus, B. Bornschein, L. Bornschein, J. Bonn, B. Flatt, A. Kovalik, B. Ostrick, E. Otten, J. Schall, T. Thummler, et al., EPJ C **40**, 447 (2005). 9

[21] F. Gatti, Nucl. Phys. B - Proceedings Supplements (Neutrino 2000) **91**, 293 (2001). 9

[22] C. Arnaboldi, C. Brofferio, O. Cremonesi, E. Fiorini, C. L. Bianco, L. Martensson, A. Nucciotti, M. Pavan, G. Pessina, S. Pirro, et al., Phys. Rev. Lett. **91**, 161802 (2003). 9

[23] F. Gatti et. al., *Mare microcalorimeter arrays for a rhenium experiment* (2006), URL `http://crio.mib.infn.it/wig/silicini/proposal/proposal_MARE_v2.6.pdf`. 10

[24] J. Angrik, T. Armbrust, A. Beglarian, U. Besserer, J. Blumer, J. Bonn, R. Carr, B. Bornschein, L. Bornschein, T. Burritt, et al., *Katrin design report 2004* (2004). 11, 13, 14, 15, 51, 52

[25] G. Beamson, H. Q. Porter, and D. W. Turner, J. Phys. E: Sci. Instrum. **13**, 64 (1980). 13, 14

[26] M. L. Leber, *Monte carlo calculations of the intrinsic detector backgrounds monte carlo calculations of the intrinsic detector backgrounds for the karlsruhe tritium neutrino experiment* (2010). 17, 27, 41, 42, 48

[27] J. A. Formaggio, *The katrin active and passive veto system* (2007). 18

[28] G. F. Knoll, *Radiation Detection And Measurement* (John Wiley and Sons, 1989), 2nd ed. 21, 24, 33, 43, 60, 63, 65

[29] B. A. VanDevender, L. I. Bodine, A. W. Myers, J. F. Amsbaugh, M. A. Howe, M. L. Leber, R. G. H. Robertson, K. Tolich, T. D. Van Wechel, and B. L. Wall, Nuclear Inst. and Methods in Physics Research, A pp. 46–50 ((2012)). 25

[30] S. Enomoto, *Internal report: Charge splitting limits between fpd pixels* (2011), URL `https://crunch5.npl.washington.edu:8443/KATRIN+Analysis/32`. 44

[31] M. L. Leber, *Effect of background rate on minimum statistical error* (2006). 51

[32] P. Doe, J. Formaggio, M. Howe, M. Leber, and R. Robertson, *Optimization criterion for the signal and background in the katrin focal-plane detector* (2007). 51

[33] P. Doe, R. Robertson, J. Wilkerson, and J. A. Formaggio, *Project execution & management plan for u.s. participation in katrin* (2007). 55

[34] P. Renschler, *Kess - a new monte carlo simulation code for low-energy electron interactions in silicon detectors* (2011). 60, 61, 62

[35] S. Enomoto, *Internal report: Rate dependence of peak position* (2012), URL `https://crunch5.npl.washington.edu:8443/KATRIN+Analysis/35`. 65, 66, 72, 74

[36] A. G. Schubert, *Searching for neutrinoless double-beta decay of germanium-76 in the presence of backgrounds* (2012). 68

Appendix A

FOCAL PLANE DETECTOR DEAD-LAYER THICKNESSES AND ERRORS

A.1 Measured Dead-Layer Thicknesses

Table A.1: The list of focal plane detector dead layer thickness and statistical error for each pixel. The total systematic errors for each pixel are the calibration, noise and diffusion related errors added in quadrature (Table A.3. Reasons for an absent pixel are listed table 6.1

Pixel	Dead Layer (Å)	Statistical Error (Å)	Systematic Error (Å)	
			+	−
5	1654.6	7.8	17.0	15.9
6	1634.0	11.3	17.5	12.6
7	1606.5	9.8	18.0	10.0
8	1613.5	11.2	17.0	11.8
12	1690.6	6.8	19.4	10.9
13	1696.9	7.2	19.4	15.0
14	1681.9	13.3	50.6	14.1
15	1753.4	10.6	15.4	11.8
16	1645.3	12.4	25.1	17.3
17	1592.8	8.8	17.7	13.9
18	1582.4	8.8	17.3	11.0
19	1512.6	11.4	14.9	9.8
20	1620.2	14.1	12.9	10.2
21	1644.0	9.4	16.9	11.1
23	1674.3	7.9	18.4	11.9

Pixel	Dead Layer (Å)	Statistical Error (Å)	Systematic Error (Å)	
			+	−
24	1658.9	8.0	20.8	11.1
25	1748.5	5.6	20.3	11.5
26	1690.2	11.5	28.3	12.4
29	1672.5	5.3	19.4	12.0
30	1531.0	10.4	15.3	10.0
31	1553.5	10.2	17.0	12.2
32	1556.8	16.2	12.3	15.7
33	1573.2	12.3	23.6	8.0
34	1637.6	14.3	12.0	10.2
35	1656.4	9.9	16.3	14.5
36	1662.9	6.2	19.3	11.6
37	1666.0	7.6	19.2	10.8
38	1648.0	9.9	25.1	10.1
39	1652.3	10.0	32.6	16.9
40	1622.6	12.9	34.0	68.4
41	1608.8	7.5	17.4	9.4
42	1588.0	9.0	17.2	11.6
43	1536.4	14.8	11.6	7.3
44	1543.0	21.7	13.3	12.8
45	1584.8	14.2	13.1	8.1
46	1608.8	15.1	11.5	13.1
47	1592.3	9.8	15.4	8.4
48	1572.0	9.9	21.2	9.4
49	1689.4	6.4	27.0	11.0
50	1645.4	7.5	25.4	63.5
53	1703.7	5.6	24.9	11.8
54	1503.8	13.5	21.5	29.1

Pixel	Dead Layer (Å)	Statistical Error (Å)	Systematic Error (Å)	
			+	−
56	1513.2	19.2	12.2	15.8
57	1541.0	17.5	14.1	16.0
58	1565.1	15.4	14.6	34.8
59	1557.7	12.4	15.7	10.2
60	1611.3	8.8	18.8	9.7
61	1610.3	9.1	15.9	9.1
62	1623.3	12.4	15.4	8.3
63	1531.8	11.9	14.5	9.3
64	1654.1	10.3	31.3	16.9
65	1576.4	8.4	16.4	15.7
66	1560.3	9.9	24.9	13.1
69	1559.2	16.7	11.3	9.8
70	1569.0	18.5	54.2	40.8
71	1594.9	9.3	55.1	37.5
72	1555.6	11.1	17.1	12.8
73	1680.4	7.6	17.7	10.9
74	1675.2	10.8	14.9	8.3
77	1610.1	7.2	18.8	14.4
78	1521.6	10.9	24.5	10.9
79	1504.3	13.7	15.0	11.4
80	1530.5	25.5	15.6	10.4
81	1514.6	23.6	21.9	14.0
82	1539.1	17.6	55.9	20.0
83	1519.8	14.4	14.2	15.9
84	1578.5	8.4	17.6	9.7
85	1620.7	8.7	18.7	12.9
86	1677.0	8.8	28.9	7.0

Pixel	Dead Layer (Å)	Statistical Error (Å)	Systematic Error (Å)	
			+	−
87	1637.5	8.1	46.3	8.6
88	1613.5	11.5	25.3	12.7
89	1580.2	8.9	16.4	11.9
90	1569.9	8.6	16.6	10.2
91	1496.4	16.9	22.6	9.3
92	1465.1	22.9	13.8	17.4
93	1526.9	15.8	43.9	29.6
94	1518.1	17.5	23.3	11.7
96	1595.7	12.2	13.9	16.4
101	1594.1	7.3	18.8	9.7
102	1572.3	8.5	22.0	8.7
103	1621.0	12.2	18.8	10.8
105	1532.1	18.6	26.8	20.9
106	1530.6	14.4	8.6	16.4
107	1557.4	15.3	9.1	9.9
108	1588.7	11.4	12.2	8.0
109	1622.3	10.4	12.4	6.7
112	1576.9	18.4	8.1	25.6
113	1523.7	12.4	9.6	8.6
114	1562.3	7.1	6.4	10.7
116	1558.4	11.8	11.8	6.4
117	1571.9	11.9	9.8	7.6
118	1512.1	11.6	43.9	28.3
119	1540.5	9.7	17.0	6.2
129	1544.1	8.2	7.5	9.8
130	1542.7	12.0	46.9	6.9
131	1604.3	11.0	12.5	6.8

Pixel	Dead Layer (Å)	Statistical Error (Å)	Systematic Error (Å)	
			+	−
132	1557.4	10.0	10.0	7.0
134	1642.6	8.9	93.0	96.4
135	1495.9	11.0	63.9	35.1
138	1616.7	53.4	69.4	23.6
142	1496.4	14.3	45.4	50.2
143	1557.3	7.8	8.4	6.0
146	1527.1	15.5	14.0	9.5
Average	1591.8	12.0	18.7	12.2

A.2 Rate Corrected Dead-Layer Thicknesses

Table A.2: The list of rate corrected focal plane detector dead-layer thicknesses and statistical error for each pixel. The rate correction is determined from the multi-parameter fit in section 6.3.3. The total systematic errors for each pixel are the calibration, noise, diffusion and rate correction errors added in quadrature (Table A.3). Reasons for an absent pixel are listed table 6.1

Pixel	Corrected Dead Layer (Å)	Statistical Error (Å)	Systematic Error (Å)	
			+	−
5	1604.3	7.8	17.2	16.2
6	1604.5	11.3	17.5	12.6
7	1583.6	9.8	18.1	10.0
8	1594.1	11.2	17.0	11.8
12	1649.7	6.8	19.6	10.9
13	1627.6	7.2	19.8	15.0
14	1602.0	13.3	50.8	14.1
15	1644.2	10.6	16.6	11.8
16	1573.7	12.4	25.4	17.3
17	1552.1	8.8	17.9	13.9
18	1555.2	8.8	17.4	11.0
19	1497.1	11.4	14.9	9.8
20	1605.3	14.1	12.9	10.2
21	1620.9	9.4	17.0	11.1
23	1642.8	7.9	18.5	11.9
24	1601.9	8.0	21.1	11.1
25	1647.9	5.6	21.1	11.5
26	1597.5	11.5	28.8	12.4
29	1570.2	5.3	20.3	12.0
30	1498.1	10.4	15.4	10.0

Pixel	Corrected Dead Layer (Å)	Statistical Error (Å)	Systematic Error (Å)	
			+	−
31	1531.1	10.2	17.1	12.2
32	1544.8	16.2	12.3	15.7
33	1556.1	12.3	23.7	8.0
34	1623.1	14.3	12.1	10.2
35	1634.3	9.9	16.4	14.5
36	1614.9	6.2	19.5	11.6
37	1604.4	7.6	19.5	10.8
38	1538.4	9.9	25.9	10.1
39	1546.8	10.0	33.1	16.9
40	1493.1	12.9	34.9	68.4
41	1555.1	7.5	17.7	9.4
42	1561.0	9.0	17.3	11.6
43	1523.3	14.8	11.6	7.3
44	1533.9	21.7	13.4	12.8
45	1570.5	14.2	13.1	8.1
46	1595.2	15.1	11.5	13.1
47	1569.5	9.8	15.4	8.4
48	1529.4	9.9	21.4	9.4
49	1606.5	6.4	27.4	11.0
50	1541.9	7.5	26.1	63.5
53	1612.8	5.6	25.4	11.8
54	1479.5	13.5	21.6	29.1
56	1502.6	19.2	12.2	15.8
57	1529.9	17.5	14.1	16.0
58	1551.6	15.4	14.6	34.8
59	1540.3	12.4	15.7	10.2
60	1584.4	8.8	18.9	9.7

Pixel	Corrected Dead Layer (Å)	Statistical Error (Å)	Systematic Error (Å)	
			+	−
61	1564.0	9.1	16.1	9.1
62	1538.2	12.4	16.1	8.3
63	1440.8	11.9	15.4	9.3
64	1554.8	10.3	31.9	16.9
65	1531.5	8.4	16.6	15.7
66	1536.9	9.9	24.9	13.1
69	1546.9	16.7	11.3	9.8
70	1557.3	18.5	54.2	40.8
71	1570.2	9.3	55.2	37.5
72	1518.9	11.1	17.3	12.8
73	1619.4	7.6	18.0	10.9
74	1576.3	10.8	16.0	8.3
77	1551.0	7.2	19.1	14.4
78	1489.6	10.9	24.6	10.9
79	1489.3	13.7	15.0	11.4
80	1522.1	25.5	15.6	10.4
81	1505.9	23.6	21.9	14.0
82	1527.6	17.6	55.9	20.0
83	1505.7	14.4	14.2	15.9
84	1549.6	8.4	17.7	9.7
85	1570.0	8.7	18.9	12.9
86	1558.4	8.8	29.7	7.0
87	1481.9	8.1	47.2	8.6
88	1524.1	11.5	25.8	12.7
89	1538.0	8.9	16.6	11.9
90	1540.9	8.6	16.7	10.2
91	1484.5	16.9	22.6	9.3

Pixel	Corrected Dead Layer (Å)	Statistical Error (Å)	Systematic Error (Å)	
			+	−
92	1456.0	22.9	13.8	17.4
93	1514.2	15.8	43.9	29.6
94	1506.8	17.5	23.3	11.7
96	1562.1	12.2	14.1	16.4
101	1538.1	7.3	19.1	9.7
102	1528.2	8.5	22.2	8.7
103	1602.7	12.2	18.9	10.8
105	1521.1	18.6	26.8	20.9
106	1517.0	14.4	8.6	16.4
107	1543.7	15.3	9.1	9.9
108	1569.2	11.4	12.2	8.0
109	1581.7	10.4	12.7	6.7
112	1522.6	18.4	8.7	25.6
113	1497.6	12.4	9.7	8.6
114	1524.4	7.1	6.8	10.7
116	1540.6	11.8	11.9	6.4
117	1553.8	11.9	9.9	7.6
118	1496.8	11.6	43.9	28.3
119	1521.2	9.7	17.1	6.2
129	1515.4	8.2	7.7	9.8
130	1525.6	12.0	47.0	6.9
131	1584.1	11.0	12.5	6.8
132	1535.1	10.0	10.1	7.0
134	1508.5	8.9	93.3	96.4
135	1430.7	11.0	64.0	35.1
138	1611.4	53.4	69.4	23.6
142	1481.5	14.3	45.4	50.2

Pixel	Corrected Dead Layer (Å)	Statistical Error (Å)	Systematic Error (Å)	
			+	−
143	1523.8	7.8	8.6	6.0
146	1463.1	15.5	14.5	9.5
Average	1554.0	5.0	18.8	12.4

A.3 Systematic Errors

Table A.3: The list of focal plane detector dead layer systematic errors for each pixel. Reasons for an absent pixel are listed table 6.1

Pixel	Calibration (Å)		Noise (Å)		Diffusion (Å)		Rate Correction (Å)
	+	−	+	−	+	−	
5	1.9	13.1	3.8	3.8	16.4	8.2	2.9
6	10.5	9.8	4.3	4.5	13.3	6.5	1.7
7	8.9	5.2	4.4	4.3	15.0	7.4	1.3
8	8.6	8.3	4.9	4.9	13.8	6.8	1.1
12	7.3	5.6	4.0	3.9	17.6	8.5	2.4
13	9.1	12.4	1.5	1.5	17.1	8.2	4.0
14	5.3	11.2	5.9	6.0	49.9	6.2	4.6
15	6.4	6.2	5.8	8.1	12.7	5.9	6.3
16	19.9	14.1	5.5	3.0	14.3	9.6	4.1
17	7.6	11.3	4.0	3.0	15.5	7.6	2.4
18	6.4	6.8	4.5	4.1	15.4	7.6	1.6
19	8.3	7.3	4.7	4.6	11.4	4.6	0.9
20	0.6	6.6	5.2	5.2	11.8	5.8	0.9
21	6.8	7.8	3.4	3.5	15.1	7.0	1.3
23	6.4	7.7	3.6	3.6	16.8	8.3	1.8
24	7.8	5.5	8.4	4.0	17.4	8.8	3.3
25	6.7	5.6	3.5	3.8	18.9	9.4	5.8
26	25.2	10.6	3.4	3.1	12.4	5.6	5.3
29	4.9	6.2	0.0	3.3	18.8	9.8	5.9
30	6.3	6.3	4.5	4.4	13.2	6.4	1.9
31	8.8	9.3	4.4	4.4	13.9	6.6	1.3
32	5.1	13.9	6.1	5.7	9.4	4.5	0.7

Pixel	Calibration (Å)		Noise (Å)		Diffusion (Å)		Rate Correction (Å)
	+	−	+	−	+	−	
33	19.3	2.3	4.8	4.4	12.7	6.3	1.0
34	2.8	7.5	4.5	4.5	10.8	5.3	0.8
35	5.8	12.1	4.0	3.9	14.7	6.8	1.3
36	5.6	5.9	3.6	4.7	18.2	8.8	2.8
37	10.7	3.2	3.2	7.6	15.6	7.0	3.6
38	19.9	5.6	4.7	4.7	14.6	7.0	6.3
39	10.6	0.4	9.8	9.8	29.2	13.8	6.1
40	32.7	54.9	1.1	15.3	9.3	37.8	7.5
41	3.8	3.5	3.9	2.6	16.5	8.3	3.1
42	6.5	8.1	4.1	3.6	15.4	7.6	1.6
43	9.5	1.0	5.5	5.3	-3.7	4.9	0.8
44	9.6	10.0	7.5	7.5	5.5	2.7	0.5
45	4.8	3.0	5.0	5.2	11.1	5.5	0.8
46	0.2	11.2	5.3	4.5	10.2	5.0	0.8
47	3.8	2.2	4.2	4.0	14.3	7.1	1.3
48	14.4	4.0	4.0	4.1	15.0	7.4	2.5
49	4.9	4.3	19.3	4.9	18.2	8.9	4.8
50	13.3	7.6	13.2	63.1	17.1	0.0	6.0
53	17.6	6.1	0.8	3.7	17.6	9.4	5.2
54	5.7	24.8	8.4	8.4	19.0	12.7	1.4
56	6.3	13.9	7.0	6.4	7.8	3.8	0.0
57	12.5	14.4	6.2	5.8	1.8	3.8	0.6
58	9.1	34.0	5.1	5.2	10.2	4.9	0.8
59	9.1	7.4	3.9	3.8	12.2	5.8	1.0
60	10.1	4.8	4.0	3.5	15.4	7.6	1.6
61	4.3	3.6	4.2	4.2	14.7	7.2	2.7
62	4.0	2.2	5.3	5.3	13.9	6.0	4.9

Pixel	Calibration (Å)		Noise (Å)		Diffusion (Å)		Rate Correction (Å)
	+	−	+	−	+	−	
63	6.5	5.4	4.9	4.7	12.0	5.9	5.3
64	6.0	3.7	27.5	9.6	13.7	13.3	5.7
65	1.7	12.9	4.7	4.2	15.6	7.8	2.6
66	19.2	9.8	4.4	4.2	15.3	7.5	1.3
69	4.5	7.5	4.6	4.6	9.2	4.2	0.7
70	12.4	9.1	47.3	35.5	23.4	18.1	0.7
71	52.9	36.6	4.4	2.9	15.0	7.5	1.4
72	9.6	10.0	4.4	4.6	13.5	6.5	2.1
73	3.6	5.8	3.4	3.8	17.0	8.4	3.5
74	2.1	2.7	4.5	3.6	14.0	7.0	5.7
77	7.4	11.4	3.6	3.2	16.9	8.3	3.4
78	24.4	8.1	2.0	4.3	1.7	5.9	1.8
79	8.4	8.5	5.4	5.3	11.2	5.5	0.9
80	11.4	4.4	8.9	9.0	5.7	2.7	0.5
81	19.3	10.9	9.2	8.4	4.9	2.3	0.5
82	0.4	6.6	51.1	5.6	22.5	18.0	0.7
83	7.1	13.9	5.6	5.6	10.9	5.3	0.8
84	6.7	4.1	3.8	4.0	15.8	7.8	1.7
85	9.2	9.5	3.9	4.2	15.8	7.7	2.9
86	8.3	5.1	-1.7	1.7	27.6	4.5	6.8
87	41.7	2.7	4.9	1.7	19.5	8.0	9.0
88	5.5	7.3	21.4	8.3	12.2	6.3	5.2
89	2.7	8.1	3.9	3.9	15.7	7.8	2.4
90	1.9	5.0	4.3	4.1	16.0	7.9	1.7
91	19.0	2.8	7.1	7.4	10.1	4.9	0.7
92	8.0	15.3	8.7	7.4	7.0	3.4	0.5
93	42.3	28.7	6.6	5.6	9.5	4.6	0.7

Pixel	Calibration (Å)		Noise (Å)		Diffusion (Å)		Rate Correction (Å)
	+	−	+	−	+	−	
94	20.8	8.7	6.6	6.8	8.1	4.0	0.7
96	1.8	14.2	5.2	5.2	12.8	6.3	1.9
101	8.8	4.0	3.6	3.8	16.2	8.0	3.2
102	14.7	0.1	4.2	3.9	15.8	7.8	2.5
103	11.9	6.8	5.0	5.0	13.7	6.7	1.1
105	25.7	19.8	6.8	6.9	2.7	1.3	0.6
106	6.2	15.6	5.0	5.1	3.2	1.6	0.8
107	6.6	9.3	5.1	3.0	3.6	1.5	0.8
108	10.4	6.2	4.6	4.6	4.4	2.1	1.1
109	10.4	5.6	5.0	3.1	4.6	2.2	2.3
112	2.8	24.3	7.1	8.0	2.7	1.3	3.1
113	7.5	7.0	4.8	4.8	3.7	1.8	1.5
114	1.0	9.7	3.7	3.8	5.1	2.5	2.2
116	10.3	4.6	4.2	3.9	4.1	2.0	1.0
117	7.6	6.0	4.7	4.1	4.2	2.1	1.0
118	43.5	28.0	4.4	3.9	3.6	1.4	0.9
119	15.9	4.5	4.5	4.1	4.3	1.0	1.1
129	4.1	8.6	4.0	3.9	4.8	2.3	1.7
130	8.6	0.1	45.5	3.9	7.7	5.7	1.0
131	10.7	4.5	4.6	4.6	4.4	2.2	1.2
132	8.2	5.2	3.5	4.1	4.5	2.2	1.3
134	89.8	92.8	24.1	24.1	3.1	9.7	7.7
135	47.4	12.3	40.9	32.8	12.8	1.7	3.8
138	64.8	10.1	25.0	21.3	0.4	0.2	0.3
142	45.1	49.9	5.5	5.5	2.4	1.7	0.9
143	5.4	3.9	3.9	3.7	5.1	2.5	1.9
146	12.4	6.9	5.7	6.3	3.0	1.5	3.7

Pixel	Calibration (Å)		Noise (Å)		Diffusion (Å)		Rate Correction (Å)
	+	−	+	−	+	−	
Average	12.4	9.5	7.3	5.6	11.8	5.2	2.4